NASA Contractor Report 165599

RIME ICE ACCRETION AND ITS EFFECT ON AIRFOIL PERFORMANCE

Michael B. Bragg

The Ohio State University
Columbus, Ohio

March 1982

Prepared for

NATIONAL AERONAUTICS AND SPACE ADMINISTRATION
Lewis Research Center
Under Grant NAG 3-28

TABLE OF CONTENTS

NOMENCLATURE

SYMBOL	DESCRIPTION
A	Area
Ac	Accumulation parameter, Eq. (34)
B	Bassett unsteady memory force
c	Airfoil chord length
C_D	Droplet drag coefficient
Cd	Airfoil drag coefficient
C_ℓ	Airfoil lift coefficient
Cm	Airfoil moment coefficient
D	Viscous drag force
E	Total airfoil collection efficiency, Eq. (28)
Fr	Froude number, Eq. (6)
g	Gravitational acceleration constant
h	Airfoil projected height
K	Inertia parameter, Eq. (5)
$\bar{K}$	Trajectory similarity parameter, Eq. (24)
K_o	Modified inertia parameter, Eq. (14)
k	Roughness height
ℓ	Length of ice growth
M	Mass of ice accretion
m	Mass of water droplet
Ma	Apparent mass force

P	Pressure gradient force
R	Droplet Reynolds number, Eq. (7)
r	Airfoil surface radius of curvature, leading edge radius
R_U	Droplet free stream Reynolds number, Eq. (12)
r'	Effective radius of curvature, Eq. (38)
S	Airfoil surface arc length
T	Air temperature
t	Time
U	Free stream velocity
u	Local flowfield velocity
V	Cummulative volume percent
x,y	Horizontal and vertical coordinate
α	Airfoil angle of attack
α_i	Airfoil angle of attack when iced
α_{LO}	Zero lift angle of attack
β	Impingement efficiency, Eq. (25)
γ	Approximate drag law exponent
δ	Droplet diameter
ε	Angle between surface outer normal and vertical
η	Dimensionless droplet position
θ	Impingement angle
λ	Liquid water content of the cloud
λ/λ_s	Ratio of droplet trajectory to Stokes law trajectory, Eq. (15)

μ	Absolute air viscosity
ρ	Air density
σ	Droplet density
τ	Nondimensional time
ϕ	Angle between the droplet trajectory and outer surface normal at impact
ψ	Angle between the droplet trajectory and the vertical at impact

Subscripts

m	Model
t	Total conditions
o	Initial condition

Superscripts

$\cdot$	Derivative with respect to nondimensional time
$\bar{}$	Vector notation

I. INTRODUCTION

The scientific study of aircraft icing began in the 1920's when aircraft were first relied upon for dependable transportation and national defense. Recently the increased utiliy of general aviation aircraft and helicopters has resulted in an increased potential for unfavorable encounters with ice. Advances in avionics has made instrument navigation very reliable and sufficiently inexpensive to enable this equipment to be within reach of most general aviation aircraft.

The aerodynamic penalties associated with flight into known icing conditions are well known; a sharp drag rise and a reduction of maximum lift coefficient. However avoiding icing by remaining on the ground when such conditions are predicted results in an economic penalty of loss of aircraft usefullness which is not easily accepted. The physical processes involved in aircraft icing, and therefore the solutions to the icing problem, are very complex.

Aircraft icing occurs when an aircraft penetrates in flight a cloud of small super cooled water droplets. A portion of these droplets impinge upon the leading edges

of various aircraft components resulting in the growth or accretion of ice. The accretion of ice and its effect on the aircraft is a very difficult problem requiring the expertise of many areas of science and engineering. However most of the problem falls into one of two categories; thermodynamics or aerodynamics.

The thermodynamics of aircraft icing deals with the process by which the droplets which impinge on the surface change from the liquid to the solid phase. Two types of ice accretions can be identified and these are depicted in figure 1. Rime ice forms a relatively streamline shape extending into the oncoming air, while glaze ice is characterized by the double horned shape. Table 1 summarizes the conditions under which each type of ice may be expected.

TABLE 1 ICE FORMATION

	Rime	Glaze
Liquid Water Content	Low	High
Air Temperature	Low	Near Freezing
Flight Velocity	Low	High
Freezing Fraction	One	Less Than One
Droplets Freeze	On Impact	Flow On Surface
Ice Color	White, Opaque	Clear
Ice Density	< 1 gm/cc	1 gm/cc

Rime ice occurs at low air temperatures and at low liquid water contents (the concentration of water droplets in the free stream) and low flight speeds. In rime icing the

droplets freeze on impact and a good approximation to this growth can be made by neglecting all thermodynamic effects [1] . Glaze ice occurs at temperatures slightly below freezing and at relatively high liquid water contents and high flight velocities. An analysis of glaze ice accretion must include the proper thermodynamic modelling.

Results of an aerodynamic wind tunnel test of a simulated ice shape [2] are shown in figure 2. Large increases in drag and a reduction in maximum lift coefficient are shown for both types of ice. Iced airfoils are difficult to analyze due to the severe surface roughness and large zones of separated flow which result from the irregular shapes of the ice accretions. Only empirical methods are currently available to predict this degradation in performance.

Two approaches to the aircraft icing problem are available. The first method is to prevent the ice from forming (ant-icing) or to remove it periodically (de-icing) from the aircraft component. This requires the design and installation of complex mechanical or thermal systems. These systems are usually designed as an add-on or retrofit to an existing component. The second approach is to design the component to eliminate or at least minimize the adverse effects of ice accretion. Such a component would not allow ice to accrete, or the ice

deposit would be of such a geometrical shape as not to adversly affect the aerodynamic performance. This method has several advantages over a de-icing or anti-icing approach:

1) No external power requirements
2) Minimize cost of construction
3) Less maintenance required
4) No chance of system failure

While components which are unaffected by ice may not be feasible, reducing this adverse effect by proper aerodynamic design certainly is feasible. Such a design would have the greatest impact on vehicles such as light aircraft, remotely piloted vehicles (RPV's), and missles where de-icing systems are often not desirable.

To design an airfoil or other aircraft component which minimizes the effect of ice accretion, a method for evaluating the iced airfoil performance must be established. An experimental approach to airfoil design is both too expensive and too time consuming. Some other means by which to design or analyze an iced airfoil must be found, reserving wind tunnel tests for final evaluation. One possible method would be an empirical approach based on the results of experimental tests of iced airfoils. However such a method has limited potential and requires a vast data base. Empirical

methods are difficult to formulate, including all the necessary independent variables, and can not be used accurately to extrapolate beyond the available data base. An analytical approach does not suffer these limitations. Properly formulated, this method will not only reproduce existing experimental data, but can be used to evaluate new airfoil designs. The theoretical model may also generate new insight into the icing problem.

To be most useful an analytical method must be as self contained as possible. That is, not rely on experimental results as input to the analysis. The analysis must contain in addition to the aerodynamic analysis, a model of the ice accretion process. The only inputs to the problem should be the atmospheric icing environment and flight conditions of the airfoil. The logical first step in such an analysis would be to initially study only rime ice accretion. Here the thermodynamics can be ignored and the droplet dynamics and aerodynamics can be emphasized. Rime ice is streamlined in shape and conventional methods of aerodynamic analysis for unseparated flows are applicable. Concentrating on rime ice initially would provide insight into the problem while allowing time for the further development of methods for dealing with icing thermodynamics and the analysis of separated flows.

While some aircraft icing areas such as thermodynamics have received recent attention, the analytical prediction of the aerodynamic performance of iced airfoils has not been studied. Little experimental work has been done since 1958 and no attempt has been made to predict the performance degradation experienced by iced airfoils since Gray's empirical method [3] of 1964. The analytical prediction of the aerodynamic effects of ice accretion on airfoils is then an important gap in our knowledge of the icing problem. In a joint NASA and FAA workshop on aircraft icing held at Lewis Research Center in 1978, the needs for new icing research were discussed. In his presentation Milton A. Beheim stated [4]

> ... a renewed effort on icing effects on airfoils is needed - not so much to refine ice protection systems as was done in the early 1950's but to determine the performance sensitivity to ice accretion effects so that airfoil selections can be made to avoid using a protection system whenever possible. Particularly for general aviation applications it may even be possible to evolve new airfoil geometries that minimize the possibilities of ice accretion and its deleterious effects on performance.

This paper focuses upon the analytical treatment of two dimensional airfoils exposed to a rime icing environment. New aircraft technology has generated requirements for an increased understanding of the icing phenomena. This re-examination of the icing problem, this

time with the aid of high speed computers and modern numerical methods, promises the improvements in icing technology necessary to increase the utilization of general aviation aircraft and helicopters in adverse weather.

II. REVIEW OF LITERATURE

The growth of ice on aircraft components results in a decrease in performance and a safety hazard which has been the subject of scientific research for over fifty years. Unfortunately most of this work was conducted in one ten year period which was concluded almost twenty-five years ago. Only now is there an attempt to organize and coordinate additional research. In an attempt to clarify the progress made by early researchers, and document the need to continue this work, this review of aircraft icing literature is presented in a historical perspective.

Early researchers disagreed on the physical phenomena responsible for ice accretion. This is quite evident in the review of early work by Bleeker [5] in 1932 and a later French report [6] in 1938. Much of this early work was performed in Germany and other Western European Countries. The U.S. made limited contributions to the study of aircraft icing before 1940; probably the most important being the development of mechanical de-icing systems. These inflatable de-icing boots were designed and built by the B. F. Goodrich Company and were installed on aircraft beginning in the 1930's. This same type of

system is still in use today.

A major step forward was made in 1940 with the first mathematical formulation of water droplet trajectories. G. I. Taylor [7] developed the differential equation governing droplet trajectories for the special cases of constant drag coefficient and Stokes law drag. Calculations were performed and the appropriate similarity parameters extracted for a few simple cases. Taylor suggested a scheme for the numerical solution of the equation for more complicated cases such as the flow about an airfoil. This work was continued by Glauret [8] who performed the numerical solution of Taylor's equations by hand calculation. Glauret furthered the work of Taylor by combining droplet trajectories to determine the local mass flux on the airfoil surface and the total collection efficiencies.

The publication of icing research in the open literature was discontinued during the war years of 1941 to 1945. However immediately after the war, perhaps due to the need for all weather military aircraft made clear by the war, icing research flourished until the mid 1950's.

After the Second World War the United States' National Advisory Committee for Aeronautics, NACA, began an ambitious program. The bulk of this work was conducted at the NACA's Lewis Research Center from 1945 to 1955. The

research was directed toward defining the natural icing environment, determining its effects on representative aircraft components, and designing techniques for ice protection [4]. Great progress was made in understanding the icing process and in protecting the aircraft from its hazards. The classic reference in the area of droplet trajectory calculations was published by Langmuir and Blodgett [9] in 1946. Here the droplet trajectory equation is presented for an arbitrary drag coefficient. The entire problem of trajectory calculations is presented in a form similar to that used today. Using a differential analyser the droplet trajectory about a cylinder, sphere, and ribbon were solved numerically and the collection efficiencies were presented for several cases. In addition, the modified inertia parameter was presented as a means to simplify the analysis by reducing the inertia parameter and the free stream Reynolds number into a single dimensionless parameter.

This method of numerically determing droplet impingement on aircraft components was used extensively by the NACA in the late 40's and early 50's. These researchers were greatly hampered by the lack of high speed digital computers and numerical solutions for the flow about an arbitrary body. As a result calculations were often made about bodies for which the flowfield could

be solved analytically. Droplet trajectories were calculated about cylinders [10,11], spheres [12], and Joukowski airfoils [13,14]. Arbitrary airfoil sections were first handled by Bergrun [15] using an empirical approach based on droplet trajectories about Joukowski airfoils. Brun, Gallagher, and Vogt [16] used a vortex substitution method to generate the flowfield about an arbitrary airfoil. This approach required a wind tunnel test to measure the surface velocities on the airfoil before the vortex strengths could be determined.

The method was used extensively by the NACA [17-19] to analyze the droplet impingement characteristics of airfoils. Extensions of this analysis were made by Serafini [20] to a supersonic airfoil and by Dorsch and Brun [21] to a swept wing. Droplet trajectory calculations were also performed about axisymmetric bodies [22-24] to simulate the nose of an aircraft or missle. The trajectory calculations made by NACA researchers proved to be very accurate and provided valuable insight into aircraft icing, data for the design of de-icing systems, and guidance to the experimentalists.

Early in the NACA icing program an extensive study was made of the natural icing environment. Numerous experimental studies were performed to determine typical combinations of cloud properties such as horizontal and

vertical size, droplet diameter, liquid water content, and air temperature experienced by aircraft. These data were compiled and summarized in three reports [25-27] which were ultimately used to compile the FAR Part 25 Appendix C [28] icing envelope. This icing envelope is still in use and defines the range of conditions over which any de-icing system must function to obtain FAA certification.

Many experimental studies were conducted in the NACA six by nine foot icing tunnel located at NASA Lewis. One important test program developed the dye-tracer technique for experimentally obtaining impingement characteristics of arbitary bodies [29]. In the dye-tracer technique a body is configured with blotter paper and exposed to an airstream containing a dyed-water spray cloud. The blotter paper is then calorimetrically examined in order to obtain local collection efficiencies, total collection efficiencies, and maximum rearward extents of impingement. This technique has been used on airfoils [30,31] and other bodies [32,33] and provides the only direct experimental data for use in the verification of droplet trajectory calculations.

Airfoil icing experiments conducted in the icing wind tunnel served two main objectives. These tests documented the change in airfoil performance characteristics due to ice accretion while also serving as test beds for new de-

icing and anti-icing systems. In the first test [34,35] no quantitative measure was made of the ice growth. Aerodynamic data was obtained from a heated wake survey probe measuring the changes in drag, while lift and moment coefficient changes were not measured. The tests were primarily to evaluate the ice protection systems. Bowden [36] in 1956 presented a fairly complete aerodynamic evaluation of icing effects on a NACA 0011 airfoil. A six component force balance system was used to enable the measurement of changes in lift, drag, and pitching moment. As in earlier tests the documentation of the ice shapes from which the aerodynamic penalties resulted was only described qualitatively.

The most complete airfoil icing analysis performed is reported by Gray [1,37]. Here theoretical and experimental impingement efficiencies, ice shape measurements, and an aerodynamic analysis was performed on an NACA 65A004 airfoil section. The experimental and theoretical impingement characteristics compared well for some cases, but the failure of the predicted values in some situations was not understood. Gray [34] presented the first empirical relation to be used to predict the changes in drag coefficient due to icing. This equation was based on the NACA 65A004 icing data and was good only for this particular airfoil.

In approximately 1958 icing research at the NACA was stopped. The advent of jet engined aircraft reduced the icing hazard and required that research efforts be shifted to new areas. At its completion the NACA program had provided good ice protection for the aircraft of the day. The analytical prediction of impingement rates had begun, but no methods for ice shape calculation or the resulting airfoil performance degradation were developed. Experimental results were confined to only a few specialized airfoils and had consisted primarily of ice protection system evaluation. Two compilations of NACA data were published in 1964. Gray [3] compiled all the iced airfoil drag data to expand his empirical equation and Bowden et. al. [38] presented an exhaustive summary of existing aircraft icing technology.

Interest in aircraft icing research was renewed in the early seventies in Europe and Canada. These studies have been primarily involved with the thermodynamics of the ice accretion process. Lozowski, Stallabrass, and Hearty [39] in 1979 presented a summary of thermodynamic modelling and their current state-of-the-art approach. All of these studies are hampered by the lack of good droplet impingement methods. Research has been conducted in Western Europe in several areas which are summarized in reference 40. Recent aerodynamic studies have been

conducted in Sweden and the Soviet Union [2] to determine experimentally the performance of iced airfoils. Similar tests conducted in the United States have in general not been published since they were conducted by manufacturers for icing certification and not government sponsored. One recent exception is the work by Wilder [41] from Boeing. Wilder presents the results of theoretical impingement calculations, experimental ice shape correlations, and iced airfoil tests. Unfortunately little information is provided as to the analytical or experimental methods used to obtain these data.

Recognizing the need for an organized icing research effort in the United States, NASA Lewis Research Center established a program of icing research in 1980. The nasa program includes a broad range of research objectives. The evaluation of de-icing systems and anti-icing systems [42] has recently begun in the Lewis Icing Tunnel. Analytical efforts include a three dimensional droplet trajectory code [43], and preliminary results of this dissertation [44]. Hopefully the need to apply current technology to the icing problem, as revealed by this review of past research efforts, will be met by the current NASA icing research program.

III. THEORETICAL ANALYSIS

Before the aerodynamic performance of an airfoil with rime ice can be determined, the geometry of the ice accretion must first be calculated. This section presents the theoretical method for the prediction of rime ice shapes which accrete on unprotected airfoils. Therefore the first step in the theoretical analysis is to formulate and analyze the equation governing the trajectory of a single spherical particle in a moving fluid.

Trajectory Equation

Aircraft rime icing occurs when super cooled water droplets impact the leading edge of an aircraft component. These droplets have diameters of 10 to 50 microns [28] and experience Reynolds numbers low enough to ensure that the particles remain spherical in shape [43]. For rime icing clouds the liquid water content which exists rarely exceedes 2.0 grams of water per cubic meter of air. Due to this low concentration of water droplets in the free stream, the flow may be considered uncoupled [45] and the influence of the droplet on the flowfield ignored.

By applying Newton's Second Law, F=ma, to the particle, the governing equation can be derived. This

equation has been presented by Soo [46] and Rudinger [47] as

$$m\left(\frac{d^2\bar{x}}{dt^2}\right) = \bar{D} + \bar{P} + \bar{M}_a + \bar{B} + m\bar{g} \qquad (1)$$

This equation may be significantly reduced for the present application. For a water droplet moving in air the density of the particle is much greater than that of the fluid. Therefore, the pressure gradient term, $\bar{P}$, and, $\bar{Ma}$, the apparent mass term may be neglected [46,47]. The fourth term in equation (1), $\bar{B}$, represents the Bassett force. This term accounts for the deviation of the flow pattern around the particle from that of steady state and represents the effect of the history of the motion on the instantaneous force [47]. This term is significant if the particle density is of the same order as that of the fluid, or if the particle experiences large accelerations. Droplets can experience large accelerations when in the leading edge region of an airfoil. Norment [43], using the work of Keim [48] and Crow [49], has shown that for the icing problem the accelerations experienced by the droplets are not large enough for the Bassett term to be significant. Therefore the Bassett term, $\bar{B}$, can also be dropped from the analysis. With these assumptions, eq. (1) reduces to.

$$m\left(\frac{d^2\bar{x}}{dt^2}\right) = \bar{D} + m\bar{g} \qquad (2)$$

For the small water droplets considered in the icing problem, and for the small time scales involved, the gravity or settling term may in general be dropped from the analysis. However, it will be retained here to allow a more general application of the method. The viscous drag term, $\bar{D}$, can be expressed in the conventional manner as

$$\bar{D} = \frac{1}{2} \rho C_D S \left|\bar{u} - \frac{d\bar{x}}{dt}\right| \left(\bar{u} - \frac{d\bar{x}}{dt}\right)$$

Where S is the cross sectional area of the sphere and C_D the drag coefficient derived from experimental results. Note that here the drag is evaluated using the slip velocity, that is the velocity between the droplet and the local airstream. Substituting in for the drag and dividing through by the mass, eq. (2) becomes

$$\frac{d^2\bar{x}}{dt^2} = \frac{3}{4} \frac{\rho C_D}{\delta \sigma} \left|\bar{u} - \frac{d\bar{x}}{dt}\right| \left(\bar{u} - \frac{d\bar{x}}{dt}\right) + \bar{g} \qquad (3)$$

Nondimensionalizing eq. (3) yields

$$\ddot{\bar{\eta}} = \frac{1}{K} \left(\frac{C_D R}{24}\right) \left(\bar{u} - \dot{\bar{\eta}}\right) + \frac{1}{\bar{F}_r 2} \frac{\bar{g}}{g} \qquad (4)$$

which is the governing equation for a droplet trajectory. The nondimensionalization was performed with respect to the characteristic velocity, U, the free stream velocity, and the characteristic length, c, the airfoil chord. Differentiation is with respect to nondimensional time, τ,

where $\tau = Ut/c$.

In eq. (4) two dimensionless parameters occur. The inertia parameter, K, is

$$K = \frac{\sigma\delta^2 U}{18c\mu} \tag{5}$$

and is essentially a nondimensional particle mass. The second parameter, Fr, is the Froude number

$$F_r = \frac{U}{\sqrt{cg}} \tag{6}$$

which is the ratio of inertia to gravitational forces. A third similarity parameter appears due to the form of the CdR/24 term in eq. (4).

The drag coefficient of a sphere in a non-accelerating stream has been measured as a function of Reynolds number by many researchers. Sphere drag is also in general a function of particle Mach number. However, for rime icing which occurs at low flight velocities, the particle Mach numbers are low and the compressibility effects on sphere drag are not significant. Here Reynolds number is based on droplet diameter and the relative velocity between the stream and the particle. Reynolds number as used here is given by

$$R = \frac{\rho\delta U|\bar{u}-\dot{\bar{n}}|}{\mu} \tag{7}$$

A standard drag curve has been established from these

results and is presented in Schlichting [50]. For low Reynolds numbers the well known classical Stokes solution for sphere drag is

$$C_D = \frac{24}{R}$$

However this theoretical result is for creeping motion and is not valid for the higher Reynolds numbers experienced by icing droplets. Stokes drag law is however a limiting case used to establish empirical fits to the standard sphere drag curve good for higher Reynolds numbers. Langmuir [9] presented one of the earliest empirical fits of the standard sphere drag curve given by

$$\frac{C_D R}{24} = 1 + 0.197R^{0.63} + 2.6 \times 10^{-4} R^{1.38} \qquad (8)$$

This equation provides good drag coefficients up to a Reynolds number of 1000. A somewhat simpler form proposed independently by Klyacho [51] in 1934 and Putnam [52] in 1961 is

$$\frac{C_D R}{24} = 1 + \frac{1}{6} R^{2/3} \qquad (9)$$

Both eq. (8) and (9) represent good fits to the experimental results as do several other similar equations proposed by other researchers. The standard drag curve, Stokes law, eq. (8), eq. (9), and the recent and more accurate measurements of Beard and Pruppacher [53] are

compared in Table 2.

Table 2 Comparison of Particle Drag Coefficients, C_D

R	Std	Stokes	Eq. (8)	Eq. (9)	Beard and Pruppacher
0.01	2400.	2400.	2426.	2420.	
0.1	243.	240.	251.	249.	242.7
1.	26.9	24.0	24.5	28.0	26.45
10.	4.33	2.40	4.43	4.26	4.149
100.	1.09	0.24	1.14	1.10	1.073
500.	0.568	0.048	0.588	0.552	
1000.	0.469	0.024	0.477	0.424	

The empirical fits for the sphere drag coefficient including equations (8) and (9) are of the general form

$$\frac{C_D R}{24} = \sum_{i=1}^{N} C_i R^{Yi} \tag{10}$$

Using eq. (7) for R, eq. (10) can be written as

$$\frac{C_D R}{24} = \sum_{i=1}^{N} C_i R_U^{Yi} |\bar{u}-\dot{\bar{\eta}}|^{Yi} \tag{11}$$

where R_U is the free stream droplet Reynolds number

$$R_U = \frac{\rho \delta U}{\mu} \tag{12}$$

Therefore, since the droplet drag coefficient can be expressed in the form of eq. (11), the Stokes parameter, CdR/24, appearing in eq. (4), yields the additional similarity parameter R_U, the free stream droplet Reynolds number.

The trajectory of a liquid droplet, for the rime icing problem, has been shown to be governed by the differential equation (4). Eq. (4) contains the three similarity

parameters R_U, K, and Fr. In the next section R_U and K are combined into a single parameter which greatly simplifies the analysis. The flowfield which enters equation (4) as u, will also be discussed in a later section.

Trajectory Similarity Analysis

In the derivation and discussion of eq. (4) it has been shown that the droplet trajectory, ignoring the flowfield, is a function only of the three similarity parameters R_U, K, and Fr, and the initial droplet conditions. To simplify this analysis the Froude number, Fr, will be dropped, since it can be shown to be negligible for the rime icing problem. The scaling of the gravity force and other terms in eq. (1) will be discussed later. Neglecting the gravity term eq. (4) becomes

$$\ddot{\bar{\eta}} = \frac{1}{K}\left(\frac{C_D R}{24}\right)\left(\bar{u}-\dot{\bar{\eta}}\right) \qquad (13)$$

Now the trajectory depends only on R and K, assuming the initial conditions in nondimensional form are constant.

The identification of the proper similarity parameters for a problem is very important. Not only do the parameters simplify the analysis, but they also aid in the presentation of experimental and numerical data, and serve as scaling parameters in the design of scale model tests. For aircraft icing scale model tests, using R_U and K to

establish test conditions violates other similarity parameters. For example, often only the model speed and droplet diameter can be varied. Holding R_U and K constant then requires that

$$\delta_m = \left(\frac{c_m}{c}\right) \delta \quad \text{and} \quad U_m = \left(\frac{c}{c_m}\right) U$$

As a result, for small scale models the test velocities are very large and violate the Mach number scaling of the flowfield. Similar problems in the scaling of drops in aircraft wakes have been reported by Ormsbee and Bragg [54]. Recent icing tests by a Swedish-Soviet research group [2] chose to ignore the Reynolds number scaling and hold only the inertia parameter constant in an attempt to avoid this problem.

Methods are available to alleviate this scaling problem by reducing the number of similarity parameters. Combining the similarity parameters R_U and K into one parameter would also greatly simplify data presentation. The first attempt to combine R_U and K was made by Langmuir when he presented the modified inertia parameter, K_o. This parameter will be discussed here and a new derivation presented which for the first time yields an analytical solution. In addition, a method is presented which is much simpler to use, and in many cases more accurate.

Modified Inertia Parameter : The modified inertia parameter, K_o, was presented by Langmuir [9] in 1946 to be used to present aircraft icing data. In fact, this parameter is still in wide use in the aircraft icing community athough no theoretical proof of its validity is available [38]. Currently no closed form solution for the parameter exists and a graphical technique or curve fit to the numerically generated data is used. Here the K_o parameter will be derived from the governing differential equation and a closed form solution obtained.

The modified inertia parameter, K_o, is defined as

$$K_o = K\left(\frac{\lambda}{\lambda_s}\right) \tag{14}$$

where K is the inertia parameter and λ/λ_s is the ratio of the trajectory of a droplet in still air, with an initial Reynolds number of R_U and gravity neglected, divided by the same trajectory of the droplet if the drag is assumed to obey Stokes law. So K_o combines K and R_U into a single parameter since λ/λ_s is a function of R_U alone. Langmuir showed that λ/λ_s is given by

$$\frac{\lambda}{\lambda_s} = \frac{1}{R_U}\int_0^{R_U} \frac{dR}{\frac{C_D R}{24}} \tag{15}$$

Using the standard sphere drag curve for $C_dR/24$, Langmuir performed this integration numerically to generate λ/λ_s as a function of R_U which is still in use today.

By using the differential eq. (13) we can examine more carefully the origin of Langmuir's K_o parameter. It is not clear from reference 9 if Langmuir derived K_o in this way, but the basic relationship between K_o and the governing differential equation was suggested in 1952 in reference 55.

By rearranging eq. (13), it becomes

$$\left(\frac{K}{\frac{C_D R}{24}}\right)\ddot{\bar{\eta}} = (\bar{u} - \dot{\bar{\eta}}) \tag{16}$$

Here $CdR/24$ is a complex function of R, with R varying along the particle trajectory. If some suitable average of the term on the left hand side of eq. (16) could be found, the R_U and K parameters can be combined into a single similarity parameter. Assume that the particle experiences Reynolds numbers from zero to R_U, the value based on the free stream velocity. Then averaging this term yields

$$K_o = \frac{K}{R_U}\int_o^{R_U} \frac{dR}{\frac{C_D R}{24}} \tag{17}$$

The modified inertia parameter is merely the average value of the single coefficient which appears in the droplet trajectory equation (16). K_o is not an exact similarity parameter, but does have valid theoretical justification as it is a straightforward simplification of the governing particle trajectory equation. The modified inertia

parameter provides good data correlation, provided the range of Reynolds numbers experienced is consistent with the range zero to R_U.

A closed form solution for K_o can be found if an integrable form of the droplet drag coefficient is used in eq. (8). Putnam [52] and Klyacho [51] developed such an equation valid up to a Reynolds number of 1000 as

$$\frac{C_D R}{24} = 1 + \frac{1}{6} R^{2/3} \qquad (18)$$

Following the work of Putnam, and after considerable integration and algebra, a closed form of K_o is given as

$$K_o = 18K\left[R_U^{-2/3} - \sqrt{6}\, R_U^{-1}\mathrm{Tan}^{-1}\left(\frac{R_U^{1/3}}{\sqrt{6}}\right)\right] \qquad (19)$$

This equation is within one percent of Langmuir's calculated values until R_U approaches 1000 where Langmuir's values deviate from those of eq. (19). This is due in part to the different droplet drag values used, eq. (3) and (18), and probably some accumulation of error in the numerical procedure.

The lower limit of eq. (19) can be used to check the derivation of K_o. By definition K_o must approach the inertia parameter for small values of the Reynolds number where the particle drag is essentially governed by Stokes law. By expanding the inverse tangent function and taking the limit as R_U approaches zero, eq. (19) reduces as

expected to K_o equals K. By examining eq. (19) as R_U approaches infinity K_o takes the form

$$K_o = 18K\ R_U^{-2/3} \qquad (20)$$

It is also interesting to compare the curve fit developed by Stallabrass and Lozowski [39] for K_o where

$$K_o = \frac{K}{1+0.0967\ R_U^{.6367}} \qquad (21)$$

This compares well to eq. (19); note the similarity in the $1/R_U^{.6367}$ term in eq (21) and the $R_U^{-2/3}$ expression in eq. (19).

The use of eq. (19) should improve the usefullness of the existing icing data correlated with K_o. Eliminating interpolation or curve fits to Langmuir's tabulated data should also improve accuracy. Eq. (19) could be used to reduce other droplet trajectory data, however, the analysis to follow will result in a parameter which is easier to use and more accurate and versatile than the K_o parameter.

Trajectory Scaling Parameter : An alternative approach can be taken to simplify the single coefficent appearing in the trajectory eq. (16). Instead of assuming that $C_dR/24$ is a constant, as was done to derive K_o, here assume that

$$\frac{C_DR}{24} = CR^Y \qquad (22)$$

which is the first term of the general equation (10). This appears as a straight line on the log-log plot of $C_dR/24$ vs. R, figure 3. A similar approximation has been made before by Ormsbee and Bragg [54,56] and by Armand et. al. [57] to scale droplet trajectories. The trajectory equation becomes

$$\ddot{\bar{\eta}} = \left(\frac{CR_U^{\gamma}}{K}\right)|\bar{u}-\dot{\bar{\eta}}|^{\gamma}(\bar{u}-\dot{\bar{\eta}}) \qquad (23)$$

Now define the trajectory similarity parameter, $\bar{K}$, as

$$\bar{K} = \frac{K}{CR_U^{\gamma}} \qquad (24)$$

where the coefficient in eq. (23) has been inverted to follow the convention established by the modified inertia parameter.

The appearance of the $|\bar{u} - \dot{\bar{\eta}}|^{\gamma}$ term in eq. (21) simplifies the use of this parameter while decreasing the expected increase in accuracy over the K_o parameter. Since a γ occurs outside of the $\bar{K}$ term, C and γ cannot in general be functions of R_U, but must be chosen from a single best fit of $C_dR/24 = CR^{\gamma}$ over the entire range of Reynolds numbers to be experienced by all particles under consideration. Then after C and γ have been chosen for a particular application, a simple parameter combining K and R_U is available to be used for data presentation or establishing scale model test conditions. Note that if

the gravity term need be included, this requires only that the Froude number, Fr, also be considered in addition to $\bar{K}$.

A careful analysis of the modified inertia parameter, K_o, and the trajectory scaling parameter, $\bar{K}$, shows that the two parameters are related. If the approximate drag law of eq. (22) is assumed and used in eq. (17) the result is

$$K_o = \frac{K}{C(1-\gamma)R_U^{\gamma}}$$

For this special case then K_o differs from $\bar{K}$ by only a constant. While the general form of K_o given by eq. (19) is more complicated, it too can be seen to be in a functional form similar to that of $\bar{K}$. Taking the limit of both K_o and $\bar{K}$ as R_U approaches zero yields just K in both instances. As R_U approaches infinity the limit of K_o is

$$K_o = 18KR_U^{-2/3}$$

as given earlier in eq. (20). This is exactly eq. (22) for $\bar{K}$ if $\gamma = -2/3$ and $1/C = 18$. Therefore it has been shown that K_o and $\bar{K}$ are the same within a constant if a simple drag law is assumed in deriving K_o. So K_o and $\bar{K}$ are certainly closely related but do vary slightly in their working range.

A method for selecting the γ to be used in the $\bar{K}$ parameter must be determined. The selection of a γ depends on the range of Reynolds numbers to be experienced by the particles during their trajectories. Since a γ term occurs in the differential equation outside the $\bar{K}$ term (see eq. 23) only one γ may be selected for each application of $\bar{K}$. So for a scaling application a different γ may be selected for each particle considered, however, when $\bar{K}$ is used to present data, an average value of γ must be used which is good over all possible particle trajectories to be presented. The value of the constant C appearing in the $\bar{K}$ parameter has no effect on the use of the term and is considered to be equal to one for convenience.

Before γ can be determined the Reynolds number range experienced by a rime icing particle must be estimated. The super cooled water droplets are assumed to be at rest with respect to the atmosphere initially, and therefore the lower bound on the Reynolds number range is zero. The droplet experiences its maximum Reynolds number when it is in the immediate proximity of the airfoil leading edge where the velocity gradients, and therefore the relative velocity between the drop and the fluid, are large. In figure 4 the Reynolds numbers experienced by droplets along their trajectory is shown. This information was generated using the computer code described in Section IV.

The droplets were started five chords in front of a typical general aviation airfoil operating at a cruise condition. Note that all the particles experience Reynolds numbers in the Stokes law range for the first nintey percent of their trajectories. Only as the droplets approach the body do the Reynolds numbers increase dramatically. This analysis has shown that the droplets usually experience maximum Reynolds numbers of less than one-half R_U.

Using this information on the typical Reynolds number range along with figure 5 a value of γ can be determined. Figure 5 summarizes the results of a least squares fit program which calculates the value of γ which provides the best fit of the approximate sphere drag expression of eq. (22) to the standard sphere drag curve. The fit is performed from a Reynolds number of zero to R. It has been found that for the aircraft icing problem a γ of 0.35 represents a good average value to be used for preliminary scaling calculations and for data presentation. To select a γ to use in scaling a particular droplet, the average value of R for the full scale and scaled particle is found and then figure 5 can be used to determine γ. In general this is an iterative procedure, but by using $\gamma = 0.35$ to select the initial scaled R_U it converges rapidly; usually the first step is sufficiently accurate.

A systematic procedure has been presented to reduce by one the number of similarity parameters governing this class of particle trajectories. The method of Langmuir, previously little understood, has been derived from the governing differential equation and a closed form solution has been presented. This result should clarify the theoretical basis for the modified inertia parameter and make the existing data correlated using K_o easier to interpret.

A new dimensionless number, $\bar{K}$, the trajectory scaling parameter is derived. This parameter is more accurate and versatile than the modified inertia parameter. The trajectory scaling parameter may be used to simplify any trajectory analysis. All that is required is the determination of the exponent, γ, in the approximate drag law used in deriving $\bar{K}$. The exponent may be found by the following procedure:

1) Determine the range of Reynolds numbers experienced by the class of particles for which the K parameter is to be used.

2) By using a least squares or other best fit scheme, determine the γ for which the approximate drag law best fits the standard drag curve in the Reynolds number range of interest.

Experimental and numerical results in support of the $\bar{K}$ parameter, and a comparison of K_o and $\bar{K}$ will be presented in Section VI.

Flowfield

To calculate the trajectory of a particle in the vicinity of an airfoil the detailed flowfield must first be determined. The dimensionless flowfield velocity appears in the differential equation (4) as $\bar{u}$, and also in the Reynolds number, R. The effect of a compressible flowfield on water droplet trajectories has been studied [10] and found to be negligible for cases up to the critical Mach number. In addition, the viscous effects near the leading edge of an airfoil are confined to a very thin boundary layer. Since for most applications the water droplets only impact the airfoil near the leading edge, the effects of the viscous region near the airfoil are assumed negligible. It is therefore sufficient for this purpose to describe the flowfield about the airfoil by an inviscid, incompressible, potential flow solution.

Both singularity and conformal mapping methods are currently in use for predicting the flowfield about an airfoil. Both methods were used in some form by the NACA to make droplet calculations in the 1950's. This present analysis uses a modified version of a transformation scheme for arbitrary airfoils first presented by Theodorsen [58,59]. This method as formulated by Woan [60], replaces the Joukowski transformation used by Theodorsen for the first step by a Karman-Trefftz

transformation. This provides a better near circle for airfoils with finite trailing edge angles. The second important feature of this method is in the solution for the exact circle. For most applications only the velocity on the airfoil surface is desired. To obtain only the surface velocities a simplified approach is available which eliminates the need to calculate all the coefficients in the complex Fourier series which transforms the near circle to an exact circle. However, the Fourier coefficients are needed to determine the velocity in the flowfield at some point not on the airfoil. The analysis of Woan provides for the determination of sufficient Fourier coefficients to solve for the entire flowfield.

The Theodorsen method has been criticized in the past for failing to reproduce the flowfield accurately, particularly in the vicinity of the leading edge. It now appears that this was a characteristic of early numerical schemes and not of the method itself. The velocity distribution computed about a typical general aviation airfoil by this method is compared to the sophisticated singularity method of Eppler [61] in figure 6. Only the leading edge region is shown where the calculated velocity distributions are practically identical. The comparison of the surface velocities over the rest of the airfoil is

also excellent. This demonstrates the validity of the Theodorsen flowfield code.

The method provides an accurate velocity anywhere in the flowfield. This information is used in the solution of eq. (4). In addition this method has proven to be very successful in handling leading edge shapes required later in the analysis.

Droplet Impingement Parameter

By analyzing the information gathered from several droplet trajectory calculations much useful information can be extrapolated. Glauert [8] first combined droplet trajectories to determine the mass of water striking a circular cylinder as a function of theta, the angle measured from the stagnation point. Langmuir [9] extended Glauert's analysis to determine the mass striking an arbitrary body as a function of S, the arc length along the surface. The analysis presented here will follow that of Langmuir with some extensions, particularly in the area of clouds containing distributions of droplet sizes.

Assuming the droplet trajectory information is available, the first step is the calculation of β, the impingement efficiency. The impingement efficiency is a dimensionless mass flux of the material impinging at a particular point on the airfoil surface. β is nondimensionalized with respect to the mass flux in the

free stream. An impingement efficiency of one is just that in the free stream, or it is the dimensionless mass flux on an imaginary flat plate, which does not alter the free stream flow, placed perpendicular to the free stream.

The impingement efficiency on an airfoil surface can be deduced from figure 7. The position on the airfoil surface is given by S, the arc length along the surface measured from the leading edge. S is measured in chords and is positive on the upper surface and negative on the lower surface. The vertical position, dimensionless with c, in a plane perpendicular to the free stream is given by y_o. The mass of water droplets between the two particle trajectories a distance δy_o apart in the free stream is distributed over a length δS on the airfoil surface. As the length δS approaches zero, the local impingement efficiency becomes

$$\beta = \frac{dy_o}{dS} \tag{25}$$

Note that in the free stream δy_o equals δS so that $\beta = 1$ as required. β can now be calculated by taking the derivative of the y_o as a function of S curve derived from individual droplet trajectory calculations.

The total mass flow rate of water caught per unit span by the airfoil is then given by

$$M = U\lambda c \int_{S_L}^{S_U} \beta ds \tag{26}$$

Here the limits S_U and S_L are, respectively, the maximum limits of droplet impingement on the airfoil upper and lower surfaces. By substituting eq. (25) for β in eq. (26), M becomes

$$M = U\lambda c\Delta y_o \tag{27}$$

The total mass collected by the airfoil then depends on Δy_o, the distance in the free stream between the upper and lower tangent trajectories, figure 7. It is convenient to define an overall collection efficiency, E, to evaluate and compare the impingement or catch rates of various airfoils. The collection efficiency is defined by the rate of mass caught divided by that of the free stream

$$E = \frac{\Delta y_o}{h} \tag{28}$$

Here h can have two different values. Some researchers take h as the maximum airfoil thickness to chord ratio, while others use the maximum projected frontal height, which is a function of angle of attack. This paper uses the later definition unless otherwise specified.

The preceding discussion describes the calculation of β where the icing cloud contains only a single droplet size. In general clouds contain a distribution of particle sizes about some volume mean diameter, VMD. To represent the total impingement efficiency, β_t, for a point on the

airfoil including the particle size distribution effect, the equation is

$$\beta_t(S) = \int_{\delta_{min}}^{\delta_{max}} \beta(\delta, S)\left(\frac{dV}{d\delta}\right)d\delta \qquad (29)$$

Here $\beta(\delta,S)$ is the impingement efficiency at a point S on the airfoil surface due to a particle size δ. Langmuir [9] has defined four particle size distributions about the VMD which are fairly representative of actual icing clouds. The distributions are defined by V, the cummulative volume of water in the cloud, as a function of δ, the droplet diameter. The $(dV/d\delta)$ term in eq. (29) is the derivative of this curve and is a function of only δ. Considering the entire range of droplet sizes also complicates the calculation of the total mass and collection efficiency. the total mass becomes

$$M_t = U\lambda c\int_{S_L}^{S_U}\int_{\delta_{min}}^{\delta_{max}} \beta(\delta,S)\left(\frac{dV}{d\delta}\right)d\delta dS \qquad (30)$$

and the collection efficiency is

$$E_t = \frac{1}{h}\int_{\delta_{min}}^{\delta_{max}} \Delta y_o(\delta)\left(\frac{dV}{d\delta}\right)d\delta \qquad (31)$$

Here $\Delta y_o(\delta)$ is the difference in the y_o values in the free stream between the tangent trajectories for a particle of size δ. The value $\Delta y_o(\delta)$ can be determined directly from the analysis or is given by

$$\Delta y_o(\delta) = \int_{S_u}^{S_L} \beta(\delta, S)\, dS \qquad (32)$$

The impingement efficiency, β, and as a result the total mass caught, M, and the collection efficiency, E, can now be determined by combining the results of several droplet trajectory calculations. For the rime ice case, knowing β as a function of S and the free stream conditions permits the prediction of an ice shape.

Ice Shape Calculation

Using the information provided by the β curve an ice shape can be predicted for the case of dry accretion (rime ice). Glauret [8] recognized this relationship between and the rime ice deposit. However he was only able to give a pictorial representation of the shape by measuring out from the surface a distance proportional (to an arbitrary scale) to the local rate of droplet impingement. Wilder [41] has calculated rime ice shapes assuming the ice grows out normal to the airfoil surface, but has ignored the local curvature of the airfoil surface. Here the equation for ice growth will be derived including the effect of surface curvature and an arbitrary direction of ice growth.

Consider an area dA perpendicular to the free stream velocity vector. The mass of water passing through this area in a time Δt is

$$m = U\lambda\Delta t\beta dA$$

Note β is the collection efficiency on the surface dA.

The volume of ice, $\ell' dA'$, represented by m is

$$\ell' dA' = \frac{U\lambda\Delta t\beta dA}{\rho_{ice}}$$

Rearranging and nondimensionalizing ℓ' by c

$$\ell = A_c\beta \tag{33}$$

where Ac is a new similarity parameter given as

$$A_c = \frac{U\lambda\Delta t}{\rho_{ice} c} \tag{34}$$

The accumulation parameter can be interpretted as the length of the ice growth in airfoil chords that would occur on an imaginary flat plate place perpendicular to the free stream in a time Δt. Note that $\beta = 1$ on this flat plate. The accumulation parameter governs the rime icing process once a β curve has been determined. It is convenient to represent the cross sectional area of an ice shape in terms of Ac using the expression

$$A = \int_{S_U}^{S_L} A_c\beta dS$$

Performing the integration the area becomes

$$A = A_c\Delta y_o \tag{35}$$

Since Ac and Δy_o are both dimensionless, the area given by eq. (35) has units of square chords.

Now using the concepts of accumulation parameter, Ac, and local impingement efficiency, β, the ice shape can be determined. Figure 8 shows the ice growth (cross-hatched) on a small segment of the curved airfoil surface dS. Here ϕ is the assumed direction of ice growth and r' the effective radius of curvature of the surface. (The effective radius of curvature will be defined later.) From geometry and noting that the ice area must equal Ac βdS,

$$\ell + \frac{\ell^2}{2r'} = \frac{A_c\beta}{\cos\phi} \qquad (36)$$

This may be solved for ℓ, and is the general expression for the length of the rime ice accretion, for a given Ac, at a point, S, on the airfoil surface. Here β, ϕ, and r' are all functions of S. Two special cases of eq. (36) are of particular importance.

The first case is to allow the ice to grow out normal to the surface. Here $\phi = 0$ and r' is just r, the local radius of curvature of the airfoil surface. Eq. (36) then becomes for-normal growth

$$\ell + \frac{\ell^2}{2r} = A_c\beta \qquad (37)$$

Here a nonlinear term arises due to the radius of curvature of the airfoil, r. This term has been dropped by other researchers when calculating ℓ. This assumption is justifiable for small values of Ac or for airfoils with

a large leading edge radius. Note that when r is large, eq. (37) shows that the length of the ice is just $Ac\beta$. The importance of the nonlinear term can easily be evaluated by comparing the integrated area of the ice shape to the exact area $Ac\Delta y_o$.

A second mode of ice growth has been suggested in which the ice grows back out along the particle trajectory [39]. In this case ℓ is directed along the tangent to the particle trajectory and is given by eq. (36). Here ϕ is the angle between the normal to the surface and the tangent to the incoming trajectory, figure 9. The r' in eq. (36) is the equivalent radius of curvature. It is a measure of the rate at which the trajectories are converging or diverging as they intersect the airfoil surface and is given by

$$r' = -\frac{dS}{d\psi} \tag{38}$$

Here S is the arc length along the surface and the direction of growth Ψ is as shown in figure 9. It is not unusual for r' to be negative for tangent ice growth. This occurs when two adjacent trajectories are diverging as they intersect the airfoil. In this case ℓ will be imaginary for Ac larger than some critical value and this limits the amount of ice growth that can be predicted in a single step.

Two modes of ice growth, normal and tangent, have been discussed in relation to the solution eq. (36). However eq. (36) can be used for any ice growth scheme if the trajectory tangent in figure 9 is replaced by the assumed direction of growth and r' and ϕ are determined accordingly. No matter what scheme is used, after eq. (36) is solved for ℓ, it is easy to calculate the ice shape by moving out from the airfoil surface a distance in the Ψ direction.

Time Effects

As the ice accumulation builds on the leading edge of an airfoil, the flowfield must slowly adjust to the new boundary conditions imposed by the change in shape. This change in the airfoil shape, and the resulting change in the flowfield, will naturally alter the impingement rates on the surface. As the impingement rates change, the shape of the resulting ice accretion will also change with time. Therefore the ice accretion process is a function of time, and must be modelled accordingly if accurate analytical predictions are to be realized. The failure of initial icing rate calculations [37], or shapes based on them, to accurately predict the experimental results reinforces the need to include time dependence in the model. One method of modelling the effect of time is a time-stepping approach. The time-stepping method assumes

that the ice accretion can be broken down into a series of steady state processes. The accuracy of the method is due in part to the step size chosen.

The scheme used to perform the time stepping is itself relatively straight forward. Each time step can be broken down into three parts:

1) The flowfield is generated
2) The β curve is calculated from the particle trajectories
3) An ice shape is generated

These steps are then repeated until the desired icing time is reached. In practice the procedure may be very difficult since the iced airfoil coordinates generated in step 3 may be too "rough" to permit the calculation of a flowfield. A scheme for smoothing these coordinates is discussed in Section IV along with the numerical formulation of the problem.

IV. NUMERICAL FORMULATION

The theoretical analysis presented in Section III has been programmed for computer solution. This section describes the numerical procedures and computer codes used to predict the rime ice growth on airfoils. The solution is formulated into three steps which utilize four computer programs. The three steps are:

1) Droplet trajectory calculation including flowfield generation and the determination of impingement rates
2) Rime ice shape calculation
3) Iteration and coordinate smoothing

Step 1 contains two computer programs, while step 2 and 3 contain one each. A flowchart for the entire rime ice methodology is given in figure 10. Only the flowfield code was not written especially for this study.

Droplet Trajectory Calculation

To calculate the droplet trajectory requires the numerical solution of eq. (4). Eq. (4) is solved in the cartesian coordinate system shown in figure 11. The x-y axis is used for the trajectory calculation while the x'-y' system is used in the flowfield code. All inputs and

outputs to the trajectory code are in the x-y system. The initial conditions needed to solve eq. (4) are the droplet velocity and position in the free stream. The particle is assumed to be travelling with the free stream at some finite distance in front of the airfoil, usually five chord lengths. The initial y coordinate is selected so the particle either strikes or misses the airfoil as desired.

Eq. (4) is a second order, nonlinear, ordinary differential equation. Equations of this type are generally written in component form and reduced to first order for numerical solution. This results in a system of four simultaneous differential equations which can be solved by a step integration method. However this system is stiff, and requires special numerical treatment for a stable solution.

A stiff system has in its general solution eigenvalues which may be orders of magnitude different in absolute value and therefore each dominates the solution in different regions. If not handled properly this leads to unstable solutions [62]. This numerical formulation uses a variable step size, predictor-corrector scheme suitable for stiff systems by Gear [63,64]. When compared with the Adams method on this system of equations, the stiff method reduces the computation time by at least a factor of two.

The system of differential equations can now be solved if a local velocity vector, $\bar{u}$, and a droplet drag law are provided. The flowfield velocity calculation will be discussed in detail in the next section. This program calls a subroutine which provides the velocity at any point (x,y) in the flowfield. Several droplet drag equations are available as discussed in Section III. This program uses the drag law of Langmuir [9] given in eq. (8).

A trajectory calculation is terminated when the particle strikes the airfoil surface or misses and moves past the body. Polynomial fits to the trajectory and airfoil surface are used to determine the exact impact point, θ as shown in figure 9, and the surface length S as in figure 7. The tangent trajectories, figure 7, are calculated using an extrapolation procedure based on the impingement angle.

Using this method the program can supply the Δy_o, and $y_o = y_o(S)$ needed to calculate the local and overall collection efficiencies. All these calculations are controlled internally by the computer program, by error limits input by the user.

Figure 12 shows a typical y_o versus S plot generated by the program. The symbols are the results of actual droplet trajectory calculations. These points are curve

fit using a cubic spline which forces the slope to zero at each end point. This scheme for spline fitting the y_o vs S curve must be modified for certain special cases. For large values of $\bar{K}$ the airfoil upper or lower surface, depending on the angle of attack, may collect ice all the way to the trailing edge. In this case β does not equal zero at this limit of impingement and therefor the second derivative, rather than the first, is set equal to zero at this endpoint.

Another special case results when an area of the airfoil, between the maximum limits of impingement, collects no ice. This results in a discontinuous y_o vs S curve. In this case the curve is fit in two pieces which are connected by a region of zero impingement, $\beta = 0$. This second case occurs on airfoils with cusps, such as the NACA six series airfoils. Here the most forward region of the cusp may collect no ice for large $\bar{K}$'s and high α's, while the aft segment does collect ice. This may also occur near the leading edge when time stepping leads to a concave region in the ice shape.

The spline fit is then used to calculate the local impingement efficiency, β, which is the slope of the curve, figure 13. The β distribution and airfoil geometry are stored on disc to be used for the ice shape calculation.

Flowfield

The flowfield velocities required for the solution of eq. (4) are generated using the Theodorsen method. A modified version of the flowfield code by Woan [60] is run once and the transformation results are stored on disc. Input to the flowfield code are the airfoil coordinates in the x'-y' coordinate system, figure 11. The droplet trajectory code reads in the results of the transformation.

When the velocity at any x-y point is required, the velocity subroutine in the droplet trajectory code first must rotate to the x'-y' system, then transform the x'-y' point to the circle plane of the transformation. The transformation to the circle plane is nonlinear and therefore a Newton-Raphson iterative technique is used. Once in the circle plane the velocity calculation is straightforward. Note that this method calculates the velocity from the transformation at each point required by the step integration differential equation solver; a matrix of stored velocities with an interpolation scheme is not used by this program.

A second program by Woan [60] is available to calculate an inviscid C_ℓ, Cm, and α_{LO} if desired. This program also generates a Cp plot which is useful in ensuring smooth airfoil coordinates.

Ice Shape Calculation

Eq. (36) must be solved for ℓ to determine the rime ice shape. The ice shape prediction code reads in β as a function of S, θ (see figure 9) as a function of S, and the the airfoil coordinates from the disc file written by the droplet trajectory code. The accumulation parameter, Ac, is the only physical variable read in directly by the program. Internally the program must calculate ϕ, ψ, and ε, figure 9, and either the surface radius of curvature, r, or the effective radius of curvature, r', in order to solve for ℓ and calculate the ice shape coordinates.

For normal ice growth, eq. (37), the surface radius of curvature, and the direction of the outer normal, ε, are needed as a function of S. Both terms can be found from a polynomial fit to the airfoil coordinates. For airfoils with rough coordinates, ε is calculated at the droplet impact points and ε vs. S is fit using a cubic spline. From the cubic spline ε and r ($r = -dS/d\varepsilon$) can be calculated at any S location. This procedure provides smoother values of ε and r.

For non-normal ice growth, eq. (36), r', ϕ, and ψ must be determined. For the tangent case θ is known at each particle impact point and ε can be calculated from a polynomial fit of the airfoil. Then ψ ($\psi = \varepsilon + \pi/2 - \theta$)

versus S can be spline fit and r', eq. (38), ψ, and ϕ can be found for any S location. The code allows for ice growth directions other than normal, ε, and tangent, ψ. By redefining the angles ψ and ϕ to be measured with respect to the assumed ice growth direction, instead of the trajectory tangent, the same method that was used for the tangent case can be used here. Then the assumed ice growth direction ψ can be chosen arbitrarily.

With ℓ and the direction of growth determined, each airfoil coordinate affected by the ice is recalculated. This generates the iced airfoil coordinates. A trapezoidal integration is used to determine the ice shape area to be checked against the exact area, eq. (35). The original and iced airfoil coordinates are written on disc for input to the next code.

Iteration and Smoothing

Airfoil analysis codes are in general very sensitive to both the first and second derivatives of the airfoil shape as provided by the input coordinates. After the airfoil has been iced, the coordinates are often too rough to run well in these programs. Existing airfoil coordinate smoothing programs were not designed for, and therefore can not handle the types of airfoil shapes that result from the icing analysis. Therefore, a coordinate smoothing program was written specifically for the icing

problem.

The smoothing is accomplished by force fitting a polynomial of the form [65]

$$y = C_{N+1}X^{P} + C_{N}X^{N} + C_{N-1}X^{N-1} + \ldots + C_{1}X + C_{o} \quad (39)$$

to both the upper and lower surface of the ice shape. The exponent p is a fraction to allow the matching of the leading edge radius of the ice, and N is the order of the polynomial. The desired first derivative is automatically satisfied at the leading edge, and the function is forced to match the slope of the airfoil surface just aft of the ice accretion.

An additional smoothing routine is available when the ice shape is not of the form of eq. (39). In this case the ice shape is essentially smoothed by hand with the help of an interactive computer graphics program. The program displays the original airfoil leading edge and the new iced airfoil shape. By using the cursors the iced airfoil coordinates can be adjusted to provide the desired smoothing and coordinate distribution.

When time-stepping an ice build-up the smoothing program is available to generate iced airfoil coordinates to be used in the flowfield code. Depending on the value of the accumulation parameter, coordinate smoothing may or may not be required for every time step. On the last time

step smoothing may be required before the aerodynamic analysis of the resulting iced airfoil can be accomplished.

V. AERODYNAMIC ANALYSIS

The most serious effects of ice formations on airfoils are the reductions in maximum lift coefficient and a significant rise in drag. Rime ice changes the airfoil geometry and adds roughness to the airfoil. These two effects are primarily responsible for the change in airfoil performance due to rime ice. Existing airfoil analysis codes are able to analyze the iced airfoil shape, but do not properly handle the roughness effects. As a result, the effect of the change in airfoil shape and surface roughness must be handled separately. The new airfoil shape will be handled analytically, while the roughness effects will be accounted for using empirically based corrections.

Ice Shape Analysis

Rime ice accretions are streamlined in shape but do not blend smoothly into the airfoil shape. In addition the shape itself may not be "smooth" with respect to the requirements for good airfoil leading edge geometries. Due to the geometry of the ice shape severe adverse pressure gradients occur in the leading edge region. These gradients trigger the formation of small zones of

separated flow (separation bubbles) which at higher angles of attack may lead to massive separation and stall. While surface roughness may also trigger premature stall, This analysis assumes that the reduction in maximum lift coefficient of iced airfoils is due to the change in leading edge shape alone.

The Eppler [61] airfoil analysis code is used to predict the effect of the ice shape. The code uses a sophisticated potential flowfield model of distributed surface singularities with parabolic strengths on curved surface panels. The version of the code used has been modified to include the compressibility effects on the potential flow. Under this potential flow an integral boundary layer method is used to calculate the skin friction. A roughness factor is included but its only effect is to cause early transition from laminar to turbulent flow. A special feature of the program is an approximate calculation of the maximum lift coefficient. The lift is calculated by using the two dimensional lift curve slope and a corrected absolute angle of attack. The correction reduces the angle of attack based on the size of the separated zone.

The airfoil analysis program is used to analyze both the original airfoil and the airfoil with the rime ice shape. The program provides the lift, drag, and pitching

moment coefficients for both cases as well as detailed pressure distributions. The drag prediction for the ice shape must still be corrected for roughness effects.

Roughness Effects

The roughness caused by rime icing is large compared to the boundary layer thickness. This roughness not only increases the local skin friction, but it can remove a considerable amount of kinetic energy from the boundary layer. This increases the skin friction drag and adds pressure drag due to the base drag of the roughness elements and the reduction in pressure recovery due to the thickening of the boundary layer [2]. This reduction in pressure recovery can lead to premature stall due to boundary layer separation at lower than expected angles of attack.

In a recent paper Brumby [66] has compiled the existing data on the effect of roughness on maximum lift coefficient. This summary is shown in figure 14. The data shows the rather dramatic reduction in maximum lift due to relatively moderate levels of roughness. Also presented in Brumby's paper is a good discussion of the operational aspects of wing surface roughness. Although figure 13 will not be used directly in this analysis, it does provide a good check on the analytical results.

Gray [3] presented an empirical correlation to predict drag increments due to airfoil icing.

$$\Delta C_d = \left[8.7 \times 10^{-5} \frac{tU}{c}\sqrt{\lambda \beta_{max}}\left(32-T\right)^{0.3}\right]\left(1 + 6\left\{\left(1 + 2.52r^{0.1}\sin^4 12\alpha\right)\sin^2\left[543\sqrt{\lambda}\left(\frac{E}{32-T}\right)^{1/3} - 81 + 65.3\left(\frac{1}{1.35^{\alpha i}} - \frac{1}{1.35^{\alpha}}\right)\right] - \frac{0.17}{r}\sin^4 11\alpha\right\}\right) \quad (40)$$

This equation was, however, developed primarily for the glaze ice case which was felt to be the more serious problem. The correlation is linear with time which does not accurately represent the rime data. Therefore a new correlation is needed which is developed specifically for the rime ice case.

The amount of good data available for the drag of airfoils with rime ice is very limited. Therefore the problem was formulated to take advantage of the data on airfoils with leading edge roughness. (When good iced airfoil drag data is available, this correlation could be easily modified to include this new information.) Figure 15 shows the drag increase versus ice accumulation (a function of time) for both glaze and rime conditions [36]. Note that the increase in drag for the glaze case is approximately linear as predicted by Gray's eq. (40). However for the rime case, the drag increases rapidly at first, then levels off and increases linearly at a reduced

rate. This analysis, as shown by the dotted line, ignores the initial rapid increase and matches the linear section assuming a step increase in drag as soon as icing begins.

The intercept of the linear drag law proposed can be obtained from figure 16. These empirical curves were obtained from published experimental results on airfoils with leading edge roughness. Note that different types or families of airfoils are affected differently by roughness. These differences are due primarily to the amount of laminar flow the clean airfoil experiences. Gray allowed for this change by including terms based on the airfoil leading edge radius. Given a particular airfoil, figure 16 can be used to estimate the step drag rise. A value of $k/c = 0.001$ is representative of the initial roughness of the ice.

With the constant term in the proposed drag correlation determined, the form of the time dependent term must be developed. The independent variable must be dimensionless to remove the scale effect. For example, two airfoils of different chord lengths which have the same scaled ice accumulations should have the same increase in drag. Representing the drag rise as a function of ice accumulation would however give these two airfoils different drag increments. A better choice of the independent variable is the dimensionless collection

parameter, AcE. This is just the cross sectional area of the ice shape divided by the projected height of the airfoil. Here the initial value of E from the theoretical analysis is used and note Ac is linear with time.

Figure 17 shows some of the available rime ice data plotted versus the collection parameter, AcE. Note that for all the airfoils the slope of the curve is the same. The predicted results shown on figure 17 use the values from figure 16 for the AcE = 0 drag increments. Expressing the results of figures 16 and 17 in equation form

$$\Delta C_d = .01\left[15.80\ \ln\left(\frac{k}{c}\right) + 28000\ A_c E + I\right] \qquad (41)$$

where I is the constant which depends on the airfoil type, Table 3.

Table 3 Constants For The Drag Equation

Airfoil Type	Drag Constant, I	Typical k/c
4 and 5 Digit	184	.001
63 Series	218	.001
64 Series	232	.001
65 Series	252	.001
66 Series	290	.001

The new drag of the iced airfoil is then given by

$$C_{d_{iced}} = \left(1. + \Delta C_d\right) C_d$$

Note that in all cases ΔCd is based on the Cd for the

hydraulically smooth airfoil at the given angle of attack. This removes a possible source of error since all models may have different roughness levels due to the construction techniques or condition of the surface.

Analysis Procedure

The aerodynamic analysis can be summarized as:

1) Calculate the icing characteristics and rime ice shape using the procedures described in Sections III and IV

2) Use the airfoil code to analyze the clean airfoil

3) use the airfoil code to analyze the smooth iced airfoil to predict the change in maximum lift coefficient

4) Use eq. (41) to correct the drag analysis for roughness effects

Step 1 not only predicts the ice shape but the collection efficiency, E, which is needed to determine the drag in step 4. Next the clean airfoil performance is analyzed to provide a baseline and also to generate the value of Cd which the correlation of step 4 is based. The smooth ice shape is then analyzed using the airfoil code to determine the maximum lift and pitching moment. Finally the empirical corrections are made to yield the effect on drag due to the rime ice. This correlation relies upon published data and the results of steps 1 and 2. This method for analyzing the aerodynamic effects of

rime ice on airfoils uses the analytical methods which are available or have been developed here, and supplements these with empirical results when needed.

VI RESULTS AND DISCUSSION

The purpose of this study was to develop an analytical method to analyze the rime icing of airfoils. Therefore, this section deals primarily with the validation of this method. The analysis will be compared to other analytical results and to the experimental data which are available or were generated specifically for this validation. In addition, limited use of the method has been made to analyze the effects of certain parameters on icing rates.

Trajectory Analysis Validation

Langmuir [9] first formulated the droplet trajectory equation for numerical solution on a differential analyser. Several calculations were made for the case of a circular cylinder, since this flowfield can be expressed in closed form. Langmuir's results were often used as test cases for the NACA and other trajectory calculation methods.

Table 4 is a summary of some of the analytical predictions of icing rates on circular cylinders.

Table 4 Comparison of The Present Method to That of Langmuir [9] and Lozowski [67] for Cylinder Icing Rates

	Langmuir		Lozowski		Bragg	
Case No.	1	2	1	2	1	2
R	600	100	600	100	600	100
K	18	0.5	18	0.5	18	0.5
Vx	1.056	0.494	1.056	0.477	1.026	0.425
Vy	0.193	0.725	0.196	0.650	0.196	0.623
E	0.819	0.156	0.814	0.170	0.812	0.155
β_{max}	0.885	0.348	0.898	0.376	0.900	0.363
θ_m	79.8	34.2	79.5	35.6	79.1	34.4

Included in the table are the results of Langmuir and Blodgett [9], Lozowski and Oleskiw [67], and the present method. The results of two test cases are shown. Here Vx and Vy are the dimensionless velocity components of the tangent trajectory particle as it strikes the cylinder. β_{max} is the maximum impingement efficiency which for a circular cylinder with no circulation occurs at $\theta = 0$ degrees. Here θ is the angle which defines a point on the cylinder with $\theta = 0$ being the forward stagnation point. The limit of impingement for the symmetric case is then θ_m.

As indicated, all three methods agree very well on the first test case, table 4. The agreement is within one percent on the value of E and θ_m, while the values of β_{max} are within two percent. However for case two, while the agreement is good, there are some more significant differences. Case 2 is a more severe test than Case 1

since the value of K is almost 20 times smaller. This small value of K results in particles which are much more affected by the flowfield and therefore their trajectories are more difficult to calculate accurately. Here Langmuir's method and the present method agree closely, while Lozowski's calculations are about ten percent higher in collection efficiency.

The source of the differences is not obvious. All three methods use different equation solvers, drag laws, and flowfield models. The allowable errors in the numerical schemes may also be different. The present method was run with the allowable error in E not to exceed one percent. No error tolerances were reported by Langmuir or Lozowski. The most likely explanation of the difference in Lozowski's calculations is the drag law chosen. Since these particles do have low inertia, a small change in the assumed Cd could have a large effect on the results.

Droplet trajectory calculations can also be compared to early NACA results for impingement on a NACA 65A004 airfoil. Figure 18 shows the early calculations [19] compared to the present method for the airfoil at zero degrees angle of attack. The comparison is quite good considering the errors involved in the early calculations. Brun [17] estimates the error in β for the NACA method to

be about ten percent. This is due to the severe velocity gradients around the small leading edge radius and the difficulty in curve fitting, and determining the slope of, the y_o versus S curve to get β. The present method performs this calculation routinely to within one or two percent.

Recently analytical results of airfoil droplet impingement have been published by Lozowski and Oleskiw [67]. Lozowski's general numerical scheme is the same as the present analysis, while the details of the solution varies in several areas. Figure 19 is a comparison of Lozowski's results and the present method for a NACA 0015 airfoil at eight degrees angle of attack. The results of the two methods are in good agreement in all areas. The limits of impingement, β_{max}, and the β curve itself are practically identical. Lozowski's reported collection efficiency of 0.501 seems high when compared to the two curves and the value of 0.473 for the present method.

Figure 20 shows a similar comparison at a slightly different condition. However here Lozowski [67] has included the Bassett unsteady memory term which was dropped from the differential equation used in this method. The comparison is still good, with Lozowski's results showing more droplet impingement. The addition greatly complicates the droplet trajectory calculation and

results in only a small change in β. This correction is, however, within the the error caused by the difficulty in measuring the droplet size distribution in a cloud, and also the error inherent in a sphere drag curve fit.

Limited experimental data is available for water droplet impingement rates on airfoils [30]. These data were taken using the dye tracer technique in the NACA Icing Research Tunnel. Impingement data taken on a NACA 65-212 airfoil at four degrees angle of attack are compared to the theoretical results of this method in figure 21. The comparison between the theoretical and experimental results is quite good. The absolute value of β from the experiment may not be accurate due to the problems in the calibration of the free stream conditions. However the limits of impingement and overall character of the curves compare very well. It should be noted that in the experiment the droplets were not of a single uniform size as was assumed in the present calculation. This point will be discussed in the next section.

The present method and computer code for calculating droplet trajectories and ultimately impingement rates has been compared to earlier works. Results from two very early analytical methods and a recent Canadian method compare very well to the present results. These comparisons were made on both airfoils and cylinders.

Comparison of the present method to experimental results was also shown to be very good. The present method has therefore been shown to be valid and yield very accurate droplet impingement results.

VMD Approximation

Actual icing clouds contain a distribution of water droplet sizes. Figure 22 shows the resulting β curves for droplets from 10 to 50 microns impinging on a NACA 0012 airfoil at an angle of attack of five degrees. The trajectories of the smaller particles are dominated by the drag term in the differential equation since the inertia is small. The droplets follow the streamlines more closely and therefore few impinge on the leading edge. For the larger droplets the inertia term dominates and a large percentage of the particles impinge on the airfoil leading edge. Note that the area under the β curve is proportional to the total mass striking the airfoil, therefore clouds of larger particles will increase the mass of ice accreted.

Using the method of Section III and a Langmuir D distribution of particle sizes, a β curve for the entire cloud of nonuniform droplet sizes can be predicted, figure 23. Also depicted in figure 23 is the β curve for a single droplet size, the volume median diameter, VMD. The VMD is the droplet diameter for which half the volume of water in

the cloud is made up of droplets larger than the VMD, and half the volume from droplets smaller than the VMD. As seen in the figure, the VMD β curve is a very good approximation to the actual icing cloud results. The VMD approximation slightly over predicts the β max and has reduced maximum limits of impingement. However these errors are acceptable in exchange for the reduction in computer time. Ignoring the droplet size distribution effects saves an order of magnitude in computer time by reducing the number of droplet diameters which must be run. In addition it eliminates completely the calculations needed to combine this information into one curve. Therefore, unless stated otherwise, all impingement calculations presented here will use the VMD approximation.

Scaling Parameter Validation

The simplified similarity parameters K_o and $\bar{K}$ have been derived in Section III. Both parameters combine R_U and K into a single dimensionless quantity which greatly simplifies the icing problem. These parameters can be used to facilitate data presentation and to define test conditions for scale model tests. Here experimental and numerical data are used to compare and evaluate the modified inertia parameter, K_o, and the trajectory similarity parameter, $\bar{K}$.

Historically icing data has been presented using the modified inertia parameter. The degree to which K_o compresses this data to a single curve provides a measure of the accuracy of the approximation. Figure 24 shows the airfoil collection efficiency, E, for three different free stream Reynolds numbers and for various values of K plotted versus K_o. The results are from an early NACA analytical study [17] of a NACA 65A004 airfoil at four degrees angle of attack. The same data are plotted as a function of $\bar{K}$ in figure 25. Here C is taken as one and $\gamma = 0.35$ as discussed earlier. Both parameters reduce the data toward a single curve, but the $\bar{K}$ parameter shows somewhat less deviation from the curve. It is not clear from these results if the scatter in the data is caused by the similarity parameter approximation, or if the error is in the numerical results for E.

To attempt to resolve this uncertainty the present droplet trajectory code was used to generate similar data. Here a NACA 0012 airfoil at zero degrees angle of attack was analyzed at three different values of R_U and five values of K. These results, plotted as a function of K_o and $\bar{K}$, are given in figures 26 and 27, respectively. Here both K_o and $\bar{K}$ do an excellent job of reducing the data to a single curve. This suggests that the scatter in figures 24 and 25 is error in the early numerical data, and not a

reflection upon the accuracy of K_o and $\bar{K}$.

Both the modified inertia parameter and the trajectory similarity parameter simplify the droplet trajectory data presentation. An additional numerical check on the validity of the parameters can be made by comparing scaled droplet impingement efficiency curves. The results of using K_o and $\bar{K}$ as scaling parameters for a one-sixth scale model are shown in figure 28. These curves were generated using the method and computer code described earlier.

For scaling droplet trajectories the $\bar{K}$ parameter has a definite edge over K_o since γ may be optimized for each droplet size (the VMD if a distribution is considered). The procedure used for determing γ described earlier yields a γ of 0.30 for the 15 micron full scale droplet and 0.39 for the 30 micron size droplet size droplet. The values of R_U and K used as well as the droplet diameter, are given in table 5.

Table 5 Scaled Variables for Analytical Icing Test Using $\bar{K}$ and K

	Full Scale	One-Sixth Scale Model	
		$\bar{K}$	K_o
δ (μm)	15.0	5.23	5.05
R_U	115.6	40.30	38.93
$K_{\bar{U}}$	0.0393	0.0286	0.0267
δ (μm)	30.0	9.86	9.60
R_U	231.2	75.97	73.98
K_U	0.1572	0.1018	0.0966

Note that for this example it was assumed that only the particle diameter would be changed to provide the scaling. All other variables such as the aircraft velocity, droplet density, air density, etc would be held constant. This yields an equation for the droplet diameter of

$$\delta_m = \left(\frac{C_m}{C}\right)^{\frac{1}{2-\gamma}} \delta$$

The important results of the scaling comparison of figure 28 are summarized in table 6.

Table 6 Results of The Droplet Trajectory Scaling Comparison

	Full Scale	One-Sixth Scale	
		$\bar{K}$	K_o
	δ= 15 μm		
E	0.0555	0.0557	0.0508
β_{max}	0.332	0.331	0.323
	δ= 30 μm		
E	0.173	0.174	0.166
β_{max}	0.568	0.563	0.563

While K_o does a reasonable job of reproducing the full scale trajectories, the added flexibility in the $\bar{K}$ parameter allows for an excellent trajectory scaling. No experimental results are available to evaluate the similarity parameters for the airfoil icing scaling problem.

However, recently published experimental results by Ormsbee and Bragg [54] are available for a similar droplet trajectory case. In these tests conducted in the NASA Langley Vortex Research Facility, three geometrically scaled agricultural aircraft models were used to inject scaled spherical particles into the model wake. Using the complete set of similarity parameters for the droplet dynamics R_U, K, and Fr results in a unique scaled test

particle of low density and large diameter. Relaxing the constraints on the scaled particles by replacing R_U and K by $\bar{K}$ yields an infinite number of candidate test particles. This greatly simplifies the task of obtaining the test particles. While Ormsbee and Bragg did not use $\bar{K}$ in the same form as it was derived here, their method is completely equivalent in that they made a similar scaling approximation.

In these tests a hypothetical full scale aircraft and droplet test conditions were chosen. These were then scaled to determine the equivalent test conditions for a 0.10, 0.15, and 0.20 scale model. Table 7 shows the full scale and model test conditions while the particle trajectory results are summarized in figure 29.

Table 7 Scaled Physical Variables for Droplets in Aircraft Wake

	Model Scale			
	0.10	0.15	0.20	1.0
Wing semispan, m	1.22	1.83	2.44	40.0
Model velocity, m/sec	16.8	20.6	23.8	53.3
Altitude, m	.622	.933	1.24	20.4
Angle of attack, deg	2.00	2.00	2.00	2.00
Particle diameter, μm	105.	125.	105.	490.
Particle density, g/cm^3	2.42	2.42	3.99	1.00

Presented in the figure is the lateral transport of the particles by the wake vortex system as a function of the

initial injector location. For all three models the lateral transport of the scaled particles is the same, verifying the $\bar{K}$ scaling analysis. Scaling tests were also conducted [54] in which other lift coefficients, aircraft altitudes, and full scale droplet sizes were used and in all cases the particle trajectories scaled well.

Trajectory Results

Although the objective of this study was to generate rime ice shapes and evaluate their aerodynamic performance, the trajectory calculations alone provide much useful information. The droplet trajectory computer program can be used to conduct a sensitivity analysis and provide physical insight into the impingement process. The information provided by the analysis such as the overall collection efficiency and maximum limits of impingement can be used directly in the design of ice protection systems.

Figure 30 shows the paths of water droplets around a NACA 0012 airfoil. Trajectories are shown at both zero and five degrees angle of attack. Note that at five degrees the droplets which impingement on the airfoil start out below the airfoil in the free stream. This is of course due to the upwash in front of a lifting airfoil. The particles which miss the airfoil by passing over the leading edge gain a large amount of kinetic energy in the

leading edge region. These particles are therefore less influenced by the flowfield over the aft part of the airfoil. Although little quantitative information is obtained from the trajectory plots, some physical feel for the problem can be gained from them. For example, droplet trajectory plots proved very valuable in identifying regions on the airfoil where no particles hit the surface. This led to modifications in the spline fitting program as described in Section IV.

The effect of airfoil angle of attack on droplet impingement efficiency is shown in figure 31. As expected the area of impingement moves more toward the lower surface as the angle of attack is increased. Also the area under the β curve, the total mass collected, increases with angle of attack. A slight change in the location and value of β max, the maximum local impingement, occurs with the increase in angle of attack. This effects the shape of the leading edge ice shape which may cause large differences in the aerodynamic performance of airfoils iced at different angles of attack.

A sensitivity analysis may also be performed by varying the value of K, the inertia parameter. Varying K while holding R_U constant corresponds physically to subjecting airfoils of different chord lengths to the same icing conditions. Note that the airfoil chord, c, appears

in the denominator of K, so reducing c increases the value of K. Increasing K while holding R_U constant means that $\bar{K}$ increases linearly with K.

Figure 32 demonstrates the effect of varying K, or equivalently $\bar{K}$. Here the case of a NACA 0012 of chord six, three, and two feet (increasing K) is shown. Then as the airfoil chord decreases the overall collection efficiency, area under the β curve, increases. Since the smaller airfoils have more severe velocity gradients near the leading edge, the droplets are not able to follow the streamlines as well, and more droplets impinge on the airfoil. This is observed in flight when tail surfaces, because of their smaller chord, accrete proportionately more ice than the main wing. It is interesting to note that for the range of $\bar{K}$ represented by figure 32, $\bar{K}$ = .008 to .025, the collection efficiency as given in figure 27 is almost linear. In fact for this special case as $\bar{K}$ increased 200 percent, so did the collection efficiency, E.

Figure 27 also represents another use of the method. Using K as the independent variable, the initial icing rates and other results may be generated to evaluate the susceptibility to icing of a particular airfoil. Here only E is presented as a function of $\bar{K}$, but a complete

airfoil analysis would include plots of β_{max}, s_U, s_L, and the actual β curves.

Ice Shape Calculation

Before the aerodynamic performance of an airfoil with rime ice can be determined, the ice shape must be accurately predicted. This involves the time-stepping procedure outlined in Section III. Having shown that the initial icing rates predicted by the method are valid, the accuracy of the time-stepping model to predict rime shapes will now be examined.

First the assumed direction of growth out from the airfoil surface must be determined. Figure 33 shows a normal and tangent growth predicted from the same initial droplet impingement information. Both shapes represent one large icing step, that is no time-stepping was performed. The predicted tangent shape grows out into the oncoming droplets. With its increased maximum growth and reduced leading edge radius it has the general shape of a measured ice accretion. However physical intuition would suggest the normal growth to be the correct mode. In the limit as the icing time goes to zero, the tangent growth approaches the same shape as the normal mode. It is felt that the normal growth model is the physically correct solution for a time-stepping procedure. The tangent growth appears to be an approximation to the time-stepping

method as will be more obvious later.

The time-stepping procedure is demonstrated in figures 34 and 35 on a modified NACA 64-215 airfoil at a cruise condition. Here the angle of attack is 0.7 degrees and K_U = 115.6 while K = 0.044. Three time steps were taken, each representing five minutes of icing with the accumulation parameter, Ac, equal to 0.0133. Figure 34 shows the predicted ice shapes from the β curves of figure 35. Note that in the time-stepping method first the impingement efficiency is calculated on the clean airfoil, step 1 figure 35. Then this β curve is used to predict the first ice shape figure 34. The flowfield is then recalculated, the step 2 β curve generated, the new ice shape 2 predicted, and the iteration is continued. Therefore figures 34 and 35 are intimately related.

Examing figure 35 the changing airfoil shape is seen to have a significant effect on the droplet impingement characteristics. This supports the need for a time-stepping approach. The change in the impingement values with time are summarized in Table 8.

Table 8 Time Step Parameters

Step	$\bar{A}c$	β_{max}	Δy_o	ΔS
1	0.0133	0.358	0.00983	0.0495
2	0.0133	0.411	0.00909	0.0379
3	0.0133	0.472	0.00910	0.0342

The maximum inpingement efficiency β max, increases with time while the iced surface length on the airfoil, ΔS, decreases. The overall collection efficiency decreases slightly for this case. Another interesting feature is the development of the second peak in the curve on the third time step.

All these effects of time are also reflected in the predicted ice growth, figure 34. The increase in β max and reduction in ΔS generates the reduced leading edge radius of the ice and the more pointed shape. The second peak in the β curve results in the reflexed upper surface "bump" on the third time step. The effect of time-stepping is then apparent from the change in the curves from steps 1 to 3.

The accuracy of the time stepping model will be a function of the size of the time step taken. Figure 36 shows the predicted ice shape for the same modified 64-215 airfoil with one, three, and six time steps. Here the corresponding Ac's are 0.04, 0.0133, and 0.067 respectively. The β curves for the six time step case are

given in figure 37. A significant change in shape is seen between one and three steps, while the change from three to six steps is relatively small. In fact the change in shape from three to six steps is probably due as much from numerical error as from an improvement in the physical modeling.

A similar study on the effect of step size was conducted using a NACA 65A413 airfoil. The airfoil was analyzed at one degree angle of attack with R_U = 147 and K = 0.118. The length of the icing encounter is eight minutes, which for the free stream conditions assumed, gives an accumulation parameter for the total time of 0.044. The predicted ice shapes for one, two, and four time steps are shown in figure 38. Figures 39 and 40 are the corresponding β curves. Here the shapes do change from the two to four time step case. The maximum amount of ice growth, and the shape of the ice near the limits of impingement, do not agree. The four time step case has essentially taken mass from near the limits of impingement and shifted it forward by extending the leading edge growth.

From these two cases, and other experience with the method, some guidelies in selecting the step size can be formulated. The critical area is the region near the maximum limits of impingement. The ice in this region

should not be allowed to grow more than that which generates a shape that blends in smoothly with the airfoil. A rule of thumb is that the maximum growth in a single step should not exceed one-half of one percent chord, x = 0.005. This corresponds roughly to holding $\Delta\beta_{max.} < 0.005$. The allowable step size is actually a function of the leading edge geometry and the shape of the β curve. With airfoils with small leading edge radii requiring the smaller step size. The rule of thumb given, however, provides guidance in selecting an acceptable step size. The lower bound on the step size is governed by the amount of computer time required per step and the accumulation of numerical error. Error accumulates primarily due to the coordinate smoothing process. The smoothing required is due in part to the discontinuous surface radius of curvature of some airfoils and this problem is aggravated as more steps are taken. From experience the step size suggested appears to be an optimum for reducing computation time and increasing accuracy.

With the time-stepping procedure established, this method for predicting ice shapes can now be compared to some experimental results. Experimental tests completed recently in the NASA Icing Research Tunnel have generated experimental rime ice shapes for the modified NACA 64-215

airfoil [68]. The experimental rime ice shape for the cruise condition is compared to the present analytical method in figure 41. The ice accretion is small and therefore only the first one percent of the airfoil is shown. the experimental shape and the time stepped prediction (from figure 36) compare very well. The no time step case is also shown to demonstrate the improvement in the prediction when the time effects are included.

The results of this comparison, and other test cases, permit some important conclusions to be drawn. The time-stepping was done for this case assuming normal ice growth. Comparing figure 41 to the normal and tangent growth in figure 33 a similarity is seen. The tangent growth has the same general shape as the time stepped prediction. This suggests that the tangent growth is an approximation to the time effects. Also note that the time stepped shape predicts the reflexed upper-surface region and bump as seen in the experimental shape. The upper node resembles the beginning of a second horn as on a glaze ice shape. However here it occurs solely as a result of the time effects on the flowfield and droplet dynamics. While glaze ice growth is certainly a thermodynamic process, this result suggests that impingement characteristics may also be very important.

For accurate glaze ice shape predictions, the time effects on the impingement rates should also be considered.

This method has also been compared to the experimental results reported by Gray [37] on a NACA 65A004 airfoil. The airfoil is at two degrees angle of attack, $R = 113$ and $K = 0.041$, and the icing time is five minutes, $Ac = 0.0215$. The experimental and analytical ice shape is shown in figure 42. The time-stepping improves the ice shape prediction over the no time stepped case, but the shape is off considerably along the lower surface.

The overall collection efficiency parameters, however, compare very well, Table 9.

Table 9 Comparison of Theory and Experiment on the NACA 65A004 Airfoil

	Experiment	Analysis
W (lb ice / ft span)	0.404	0.331
E	0.208	0.162
S_U	0.0035	0.0040
S_L	0.090	0.10
Ice Area, ft^2	0.0207	0.0062
Ice Density (% of H_2O)	31.	85.

The total mass collected, the collection efficiency, and the limits of impingement are very close for both the experiment and the analysis. However large discrepencies occur in the cross sectional area of the ice and the ice density. The error arises due to the assumed ice density,

85 percent the density of water. This value is within the range of 75 to 91 reported by Wilder [41] and close to the value of 89 used by Lozowski and Oleskiw [67]. All these values are far from the 31 percent measured in the icing tunnel test.

The very low measured value of ice density can be attributed to the formation of rime feathers on the lower surface ice shape. These ice formations can be seen in the photographs and sketchs of reference 37. Rime feathers are thin layers of ice separated by layers of air which sometimes form during rime ice accretions. the occurence of rime feathers, which drastically reduces the overall ice density, is difficult to predict. These feathers cause the effective ice density to be a function of S. If the correct ice density could have been used in the prediction of figure 42 the agreement would have been much better. The present method does not handle the rime feather case. However, when methods are available to predict the formation of rime feathers, this could easily be incorporated in the procedure.

Aerodynamic Analysis

The details of the prediction of iced airfoil performance is given in Section V. As noted there, little aerodynamic data is available for use in verifying the method. Therefore an airfoil test was performed on a

simulated rime ice shape to generate data for this purpose. the analytical method will first be compared to the simulated ice shape data. Then for the ice shape predictions already discussed, the predicted airfoil performance will be compared to the experimental data.

The simulated ice shape test was conducted on a NACA 65A413 airfoil with the shape being that predicted by the analysis in figure 38. The tests were conducted in the 6 by 22 inch transonic wind tunnel located at The Ohio State University's Aeronautical and Astronautical Research Laboratory. Four different configurations were tested to separate out the roughness and shape effects as are done in the analysis. Complete details of the experiment can be found in Appendix A. Here the data are compared to the analysis.

No detailed pressure data can be found in the literature for airfoils with ice shapes, real or simulated. Even the most recent work by the Soviet-Swedish group [2] on simulated ice shapes contains no airfoil pressure distributions. These data are necessary for a detailed evaluation of the airfoil analysis code. Figure 43 shows the measured and predicted Cp distribution on the clean airfoil. Here the comparison is made at a lift coefficient of 0.52, Reynolds number based on chord length of three million, and Mach number of 0.40. The

pressure distribution predicted by the Eppler code is very close to that measured in the tunnel. The leading edge discontinuity on both the upper and lower surfaces is predicted, although the upper surface is off somewhat in magnitude. The rest of the pressure distribution also agrees well. A slight deviation is seen near the trailing edge where the boundary layer thickness affects the pressures. This is not accounted for in the current version of the Eppler analysis code.

Figure 44 compares the measured and predicted pressure distributions on the airfoil with the simulated rime ice shape. The lift coefficient for this comparison is 0.45. The most noticeable feature of the experimental Cp distribution are the discontinuous pressure spikes on the upper and lower surface of the leading edge. These spikes are predicted fairly well by the analysis. The presence of the spikes will cause early boundary layer transition and probably the formation of leading edge separation bubbles. Therefore the ability of the airfoil code to accurately predict this pressure distribution is the first step toward the accurate analysis of airfoils with rime ice.

The comparison between the measured and predicted lift coefficients is shown in figure 45. The predicted angle of zero lift compares very well while the lift curve slope

is slightly greater than that measured in the tunnel. The maximum lift coefficient compares well when the prediction of Eppler is corrected for the airfoil roughness effects. The "clean" airfoil was actually slightly rough due to tarnish on the brass model. This is seen in the drag data where the hydraulically smooth airfoil would have a drag coefficient of 0.0055 while the model tested had a minimum drag of 0.0086. From the work of Brumby [66] even small amounts of surface roughness are seen to reduce $C_{\ell_{max}}$, figure 14. Therefore, using the results of figure 16, the roughness height on the clean airfoil was estimated as k/c = 0.0001. using this value of k/c in Brumby's plot of figure 14 a correction of -10 percent in the maximum lift coefficient is found. This is the correction that has been applied to the analytically predicted $C_{\ell_{max}}$ for the clean airfoil in figure 45.

The iced airfoil $C_{\ell_{max}}$ results compare reasonably well with the predicted value being slightly less than that measured in the tunnel. The iced airfoil had a measured $C_{\ell_{max}}$ of about 1.0 while the theory predicted a more conservative 0.90. The theoretical maximum lift coefficient was reduced from the clean case by a leading edge separation bubble which caused massive separation from the leading edge. Apparently in the tunnel the separation was delayed and the airfoil stalled at a

slightly higher $C_{\ell_{max}}$ and angle of attack. The method appears to do a reasonable job of predicting $C_{\ell_{max}}$ degradation due to rime ice accretion.

The experimental and-thheoretical drag polars are shown in figure-46. Here three sets of experimental and theoretical predictions are presented; the clean airfoil, the airfoil with roughness on the first three percent (k/c = 0.0025), and the airfoil with the same roughness on the simulated rime ice shape. The clean prediction is from Eppler with transition moved forward using his roughness parameter. This result compares well to experiment. When roughness is added to the airfoil the drag increases as expected. Using Eppler to determine the hydraulically smooth airfoil drag and eq. (41), the predicted drag values are very close to the measured ones. This provides a good check on the empirical roughness data used in developing eq. (41).

The drag of the simulated rime ice shape (with roughness) is also shown in figure 46. Here the roughness extends back to x = 0.03 on the airfoil and covers the entire rime ice shape. The drag prediction using eq. (41) with ACE = 0.00616 is conservative compared to the experimental results. The measured value of Cd is 0.0155 compared to a predicted value of 0.0185. This is an increse of 244 percent and 311 percent respectively over

the smooth value of 0.0045. Considering the difficulty of the analysis, this represents a reasonabl e comparison. Note also that the theory is based on actual iced airfoil data and a simulated ice shape was tested. Therefore, the error may be due in part to the way in which the ice shape was simulated. This error in the simulation can not be determined from these tests, and it suggests that an experimental program is needed to develop ice simulation techniques.

The analytical method for calculating iced airfoil performance has been compared to actual airfoil icing tests. The predicted ice shape of figure 34 has been analyzed and the results are shown in figures 47 and 48. The airfoil used is the modified NACA 64-215. The lift coefficient curve, figure 47, shows the expected reduction in $C_{\ell_{max}}$ due to a leading edge bubble. Unfortunately no lift coefficient data was taken on the actual iced airfoil to be used for comparison. This reduction in maximum lift coefficient does however seem reasonable when compared to similar airfoil results.

The analytically predicted drag polars for both the clean and iced airfoils are shown in figure 48. Here experimental values of drag coefficient at 0.7 degrees angle of attack are available for the clean and iced airfoil [68]. Since no ice roughness was reported, the

results are shown for values of k/c of 0.001 to 0.005 which bracket the usual range of rime ice roughness. Here the comparison between theory and experiment is very good, especially the increment in the drag due to the ice. Again the clean value is calculated using the Eppler program with his roughness correction and the increase in drag is based on eq. (41).

The NACA 65A004 airfoil has been analyzed using the rime ice shape predicted in figure 42. The predicted drag polar and the measured values are shown in figure 49. Here again the experimental drag values are only available at one angle of attack. The analysis does an excellent job of predicting the drag increase for values in the cruise range.

The effect of the ice shape on the maximum lift coefficient is very unusual for this particular airfoil. As seen in figure 42 the ice shape forms a leading edge flap for this thin airfoil. The measured increase for this case is approximately 23 percent while the analysis shows a 12 percent increase in maximum lift coefficient. Although numerically this comparison may seem less than desireable, it actually lends a great deal of confidence to the method. The 65A004 is a very severe test of the analysis since the airfoil is so thin. To predict an increase in $C_{\ell_{max}}$ which is conservative demonstrates that

the leading edge region is being handled correctly by the analysis.

The aerodynamic analysis has been compared to both simulated and actual rime ice on three very different airfoil sections. All the results, both lift and drag, have compared very well considering the dificulty in performing the analysis. The method for the aerodynamic analysis of airfoils with rime ice presented here has been shown to be a reliable procedure. Hopefully the empirical corrections to the drag predictions can eventually be replaced by analytical methods when they become available.

VII. SUMMARY AND CONCLUSIONS

A methodology has been developed to predict the growth of rime ice, and the resulting aerodynamic penalty, on unprotected airfoil surfaces. This method has for the first time included the time effects into the icing analysis. A large portion of this study was involved in the numerical formulation of the problem for digital computer solution. However, the derivation of two new similarity parameters was primarily an analytical exercise, while some experimental work was performed in a wind tunnel evaluation of the aerodynamic analysis.

The calculation of water droplet trajectories was performed by a step integration of the governing stiff system of ordinary differential equations. The required flowfield was provided by a modified Theodorsen method. Although calculations of this type have been performed earlier, by using state-of-the-art computational facilities and numerical proceedures a large improvement has been made. The present procedure was faster, more accurate, and more generally applicable than earlier methods.

An in depth analysis of the governing differential equation has lead to a simplified similarity parameter for the problem. By using a reduced form of the droplet drag equation the two similarity parameters, R_U and K, were combined into a single parameter, $\bar{K}$, the trajectory similarity parameter. This greatly simplified the analysis.

By making a further simplification to the droplet drag equation the modified inertia parameter, K_o, first suggested by Langmuir, was derived in the same manner. As a result of this analysis a closed form solution was found for K_o. This was the first derivation of K_o from the governing differential equation, and the first time a closed form solution for it has ever been found. Experimental and numerical results have been presented in support of K_o and $\bar{K}$. The new trajectory similarity parameter has been found to be superior to K_o, especially in scaling applications.

Using the results of droplet trajectory calculations rime ice shapes have been predicted. In the derivation of these equations a similarity parameter has been identified, the accumulation parameter, Ac. For a given geometry and $\bar{K}$ the accumulation parameter governs the growth of rime ice on airfoils.

As rime ice builds up on an airfoil leading edge the effective airfoil shape becomes a function of time. This then results in the surface flux of impinging water droplets also being a function of time. The present method has included these effects into the ice shape prediction. A time-stepping procedure was employed where the airfoil geometry, flowfield, and droplet impingement efficiencies were updated periodically during the ice accretion process. Comparison of predicted rime ice shapes to those measured in a icing wind tunnel compared well. A significant improvement was seen in the theoretical shapes when the time-stepping procedure was used.

The time-stepping procedure has provided insight into the ice accretion process. Some researchers have suggested that the ice actually grows out from the surface tangent to the incoming droplet trajectories. This tangent ice growth has been shown to be merely an approximation to the time effects where the usual growth out normal to the surface was used. With the importance of including time effects in the rime icing analysis demonstrated, the method is expected to provide similar improvements to glaze ice predictions.

The aerodynamic effects of rime ice accretions on airfoils includes a reduction in maximum lift coefficient

and an increase in drag. Earlier methods for predicting the degradation in airfoil performance with ice relied totally upon empirical correlations. These methods, however, dealt only with the changes in drag and were based on initial icing rates. The present method for evaluating the iced airfoil performance was based on an analytical analysis of the resulting airfoil shape after ice accretion. The mehtod postulated that the aerodynamic effects of rime ice were due to: 1) the surface roughness of the ice, and 2) the change in leading edge geometry due to the smooth ice shape. These two mechanisms were then handled separately by the analysis.

The smooth ice shape was analyzed using existing airfoil analysis codes. The surface roughness effect was handled by correcting the analytical results based on an empirical equation which was developed here.

Since no detailed aerodynamic data on an airfoil with rime ice was available, wind tunnel tests on an airfoil with simulated rime ice were conducted. The experiment identified the effect surface roughness and ice shape have on airfoil performance. In addition to lift and drag data, these tests generated the first detailed pressure measurements ever taken on an airfoil with simulated ice. The predicted pressure distributions compared well with the experimental results as did the values for C_ℓ and Cd.

The aerodynamic analysis was verified further using values of lift and drag from icing wind tunnel tests of actual ice accretions.

The present study has identified areas where additional work is needed. The analytical method could be improved by either removing the need to smooth the shape or improving the smoothing procedure. This would increase the accuracy of the ice shape prediction and allow smaller step sizes. In addition better information on the ice density would greatly improve the method. Future analytical research on rough airfoil drag could remove the need to use an empirical drag correlation. Experimentally the need is to expand the old, and very limited, data base in terms of accurate ice shapes, ice densities, and airfoil aerodynamic performance penalties. However the most serious need is to extend this work to the glaze ice case where a flowfield with large zones of separated flow must be accurately predicted.

In summary the rime icing methodology presented here has advanced the state-of-the-art in four major areas. First, the effects of time on the ice accretion process have been included in the analysis. By using the time-stepping method very accurate rime ice shapes can be predicted. Second, an aerodynamic analysis has been formulated which is based on the actual iced airfoil

geometry. Unlike early methods which estimated Cd from only initial icing rates, this method predicts C_ℓ and Cd from the new airfoil geometry with some empirical corrections.

The third major contribution came from the wind tunnel test of the simulated ice shape. Here for the first time detailed aerodynamic data, including surface pressure distributions, were taken on an airfoil with simulated rime ice. The data provided a great deal of insight into the problem and an excellent test case for the present, and for future aerodynamic analysis. The similarity analysis provided the final contribution. Two new parameters, $\bar{K}$, the trajectory similarity parameter, and, Ac, the accumulation parameter have been derived and shown to govern the accretion of rime ice on airfoils. In addition, K_o, the modified inertia parameter has been derived from the governing differential equation and the first closed form solution for K_o has been presented.

REFERENCES

1. Gray, Vernon H. and Von Glahn, Uwe H., "Aerodynamic Effects Caused By Icing of an Unswept NACA 65A004 Airfoil", NACA TN 4155, 1957

2. Ingelman-Sundberg, M., Trunov, O. K., and Ivaniko, A., "Methods for Prediction of the Influence of Ice on Aircraft Flying Characteristics", a joint report from the Swedish-Soviet Working Group on Flight Safety, 6th Meeting, 1977

3. Gray, Vernon H., "Prediction of Aerodynamic Penalties Caused by Ice Formations on Various Airfoils", NASA TN D - 2166, 1964

4. Peheim, Milton A., "Executive Summary of Aircraft Icing Specialists Workshop", Aircraft Icing, a workshop held at Lewis Research Center, July 19-21, 1978, NASA Conference Publication 2086, pp. 1-16

5. Bleeker, W., "Einige Bemerkungen uber Eisansatz an Flugzeugen", Meteorologische Zeitschrift, September 1932, pp. 349-354 (also available as NACA TM No. 1027)

6. Comite d Etude du Givrage Rapport du 19 Mai 1938, Bulletin des Services Techniques no. 85, Publications Scientifques et Techniques du Ministere de l Air (also available as NACA TM No. 919)

7. Taylor, G. I., "Notes on Possible Equipment and Technique for Experiments on Icing on Aircraft", R & M No. 2024, British A.R.C., Jan. 1940

8. Glauret, Muriel, "A Method of Constructing the Path of Raindrops of Different Diameters Moving in the Neighbourhood of (1) a Circular Cylinder, (2) an Aerfoil, Placed in a Uniform Stream of Air; and a Determination of the Rate of Deposit of the Drops on the Surface and the Percentage of Drops Caught", R & M No. 2025, British A.R.C., Nov. 1940

9. Langmuir, Irving, and Blodgett, Katherine B., "A Mathematical Investigation of Water Droplet Trajectories", Army Air Forces Technical Report No. 5418 (Contract No. w-33-038-ac-9151), Feb. 1946

10. Brun, Rinaldo J., Serafini, John S., and Gallagher, Helen M., "Impingement of Cloud Droplets on Aerodynamic Bodies as Affected by Compressibility of Air Flow Around the Body", NACA TN 2903, March 1953

11. Brun, Rinaldo J. and Mergler, Harry W., "Impingement of Water Droplets on a Cylinder in an Incompressible Flow Field and Evaluation of Rotating Multicylinder Method for Measurement of Droplet-Size Distribution, Volume-Median Droplet Size, and Liquid-Water Content in Clouds", NACA TN 2904, March 1953

12. Dorsch, Robert G., Saper Paul G., and Kadow, Charles F., "Impingement of Water Droplets on a Sphere", NACA TN 3587, November 1955

13. Bergrun, Norman R., "A Method for Numerically Calculating the Area and Distribution of Water Impingement on the Leading Edge of an Airfoil in a Cloud", NACA TN 1397, August 1947

14. Brun, R. J. and Vogt, Dorothea E., "Impingement of Cloud Droplets on 36.5-Percent-Thick Joukowski Airfoil at Zero Angle of Attack and Discussion of Use as Cloud Measuring Instrument in Dye-Tracer Technique", NACA TN 4035, September 1957

15. Bergrun, Norman R., " An Empirical Method Permitting Rapid Determination of the Area, Rate, and Distribution of Water-Drop Impingement on an Airfoil of Arbitrary Section at Subsonic Speeds", NACA TN 2476, September 1951

16. Brun, Rinaldo J., Gallagher, Helen M., and Vogt, Dorothea E., "Impingement of Water Droplets on NACA 65 -208 and 65 -212 Airfoils at 4 Angle of Attack", NACA TN 2952, May 1953

17. Brun, Rinaldo J., Gallagher, Helen M., Vogt, Dorothea E., "Impingement of Water Droplets on NACA 65A004 Airfoil and Effect of Change in Airfoil Thickness from 12 to 4 Percent at 4 Angle of Attack", NACA TN 3047, November 1953

18. Brun, Rinaldo J., Gallagher, Helen M., Vogt, Dorothea E., "Impingement of Water Droplets on NACA 65A004 Airfoil at 8 Angle of Attack", NACA TN 3155, July 1954

19. Brun, Rinaldo J. and Vogt, Dorothea E., "Impingement of Water Droplets on NACA 65A004 Airfoil at 0 Angle of Attack", NACA TN 3586, November 1955

20. Serafini, John S., "Impingement of Water Droplets on Wedges and Diamond Airfoils at Supersonic Speeds", NACA TN 2971, July 1953

21. Dorsch, Robert G. and Brun, Rinaldo J., "A Method for Determining Cloud Droplet Impingement on Swept Wings", NACA TN 2931, April 1953

22. Dorsch, Robert G., Brun, Rinaldo J., and Gregg, John L., "Impingement of Water Droplets on an Ellipsoid with Fineness Ratio 5 in Axisymmetric Flow", TN 3099, March 1954

23. Brun, Rinaldo J. and Dorsch, Robert G., "Impingement of Water Droplets on an Ellipsoid with Fineness Ratio 10 in Axisymmetric Flow", NACA TN 3147, May 1954

24. Brun, Rinaldo J. and Dorsch, Robert G., "Variation of Local Liquid-Water Concentration About an Ellipsoid of Fineness Ratio 10 Moving in a Droplet Field", NACA TN 3410, April 1955

25. James, Alun R. and Lewis, William, "Recommended Values of Meteorological Factors to be Considered in the Design of Aircraft Ice-Prevention Equipment", NACA TN 1855, March 1949

26. Hacker, Paul T. and Dorsch, Robert G., "A Summary of Meteorological Conditions Associated with Aircraft Icing and a Proposed Method of Selecting Design Criterions for Ice-Protection Equipment", NACA TN 2569, November 1951

27. Lewis, William and Bergrun, Norman R., "A Probability Analysis of Meteorological Factors Conducive to Aircraft Icing in the United States", NACA TN 2738, 1952

28. Airworthiness Standards: Transport Category Airplanes, Part 25, Federal Aviation Regulations, Effective 2/1/65

29. Von Glahn, Uwe H., Gelder, Thomas F., and Smyers, William H. Jr., "A Dye-Tracer Technique for Experimentally Obtaining Impingement Characteristics of Arbitrary Bodies and a Method for Determining Droplet Size Distribution", NACA TN 3338, March 1955

30. Gelder, Thomas F., Smyers, William H. Jr., and Von Glahn, Uwe H., "Experimental Droplet Impingement on Several Two-Dimensional Airfoils with Thickness Ratios of 6 to 16 Percent", NACA TN 3839, December 1955

31. Von Glahn, Uwe H., "Use of Truncated Flapped Airfoils for Impingement and Icing Tests of Full-Scale Leading-Edge Sections", NACA RM E56E11, July 24 1956

32. Lewis, James P. and Ruggeri, Robert S., "Experimental Droplet Impingement on Four Bodies of Revolution ", NACA TN 4092, December 1957

33. Gelder, Thomas F., "Droplet Impingement and Injestion by Supersonic Nose Inlet in Subsonic Tunnel Conditions", NACA TN 4268, May 1958

34. Gray, Vernon H. and Von Glahn, Uwe H., Effect of Ice And Frost Formations on Drag of NACA 65 -212 Airfoil for Various Modes of Thermal Ice Protection", NACA TN 2962, June 1953

35. Von Glahn, Uwe H. and Gray, Vernon H., "Effect of Ice Formations on Section Drag of Swept NACA 63A-009 Airfoil with Partial-Span Leading-Edge Slat for Various Modes of Thermal Ice Protection", NACA RM E53J30, March 15 1954

36. Bowden, Dean T., "Effect on Pneumatic De-Icers and Ice Formations on Aerodynamic Characteristics of an Airfoil", NACA TN 3564, February 1954

37. Gray, Vernon H., "Correlations Among Ice Measurements, Impingement Rates, Icing Conditions, and Drag Coefficients for Unswept NACA 65A004 Airfoil", NACA TN 4151, February 1958

38. Bowden, D. T., Gensemer, A. E., and Skeen, C. A., "Engineering Summary of Airframe Icing Technical Data", Federal Aviation Agency, Technical Report ADS-4, March 1964

39. Lozowski, E. P., Stallabrass, J. R., and Hearty, P. F., "The Icing on an Unheated Non-Rotating Cylinder in Liquid Water Droplet-Ice Crystal Clouds", National Research Council of Canada, Division of Mechanical Engineering, Report LTR-LT-96, February 1979

40. Pierre, Marcel and Vaucheret, Xavier, "Icing Test Facilities and Test Techniques in Europe", AGARD Advisory Report No. 127, November 1978, pp. 6-1 to 6-11

41. Wilder, Raymond W., "A Theoretical and Experimental Means to Predict Ice Accretion Shapes for Evaluating Aircraft Handling and Performance Characteristics", AGARD Advisory Report No. 127, November 1978, pp. 5-1 to 5-20

42. Kohlman, D. L., Schweikhard, W. G., and Evanich, P., "Icing Tunnel Tests of a Glycol-Exuding Porous Leading Edge Ice Protection System on a General Aviation Airfoil" Paper 81-0405 presented at the AIAA 19th Aerospace Sciences Meeting, St. Louis, Missouri, January 12-15 1981

43. Norment, Hillyer G., "Calculation of Water Drop Trajectories to and About Arbitrary Three-Dimensional Bodies in Potential Airflow", NASA Contract Report 3291, August 1980

44. Bragg, M. B., Gregorek, G. M., and Shaw, R. J., "An Analytical Approach to Airfoil Icing", AIAA Paper No. 81-0403 presented at the 19th Aerospace Sciences Meeting, St. Louis, Missouri, January 12-15 1981

45. Korkan, Kenneth D., "Theoretical and Experimental Studies of Multicomponent Flow Systems", Phd Dissertation, The Ohio State University, 1975

46. Soo, S. L., "Fluid Dynamics of Multiphase Systems", Blaisdell, Waltham, Mass., 1967, pp. 31-33

47. Rudinger, G., "Flow of Solid Particles in Gases", AGARDograph No. 222, 1963, pp. 55-86

48. Keim, S. R., Fluid Resistance to Cylinders in Accelerated Motion", J. Hydraulics Div., Proc. Amer. Soc. Civil Eng., Vol 6, 1956, paper 1113

49. Crowe, C. T., Nicholls, J. A., and Morrison, R. B., "Drag Coefficients of Inert and Burning Particles Accelerating in Gas Streams", Ninth Symposium (Int'l) on Combustion, Academic Press, 1963, pp. 395-405

50. Schlichting, H., "Boundary Layer Theory", 6th Edition, McGraw-Hill, 1968, pp. 15-19

51. Fuchs, N. A., "The Mechanics of Aerosols", Macmillan, 1964

52. Putnam, A., "Integrable Form of Droplet Drag Coefficient", ARS J., Vol. 33, 1961, pp. 1467-1468

53. Beard, K. V. and Pruppacher, H. R., "A Determination of the Terminal Velocity and Drag of Small Water Drops by Means of a Wind Tunnel", J. Atmospheric Sciences, Vol. 26, 1969, pp. 1066-1072

54. Ormsbee, Allen I., Bragg, Michael B., Maughmer, Mark D., and Jordan, P. L., "Scaling Wake Particle Interactions for Aerial Applications Research", Paper 80-1873 presented at the AIAA Aircraft Systems Meeting, Anaheim California, August 4-6 1980, AIAA Journal of Aircraft, Vol.18 No. ., pp. 592-596, July 1981

55. Sherman, P., Klein, J. S., and Tribus, M., "Determination of Drop Trajectories by Means of an Extention of Stokes Law", Project M992-D, Air Research and Development Command, USAF, Contract AF 18(600)-- 51, April 1952

56. Ormsbee, A. I. and Bragg, M. B., "Trajectory Scaling Laws for a Particle Injected into the Wake of an Aircraft", University of Illinois at Urbana-Champaign, Aviation Research Laboratory, Report ARL 78-1, June 1978

57. Armand, Claude, et. al., "Techniques and Facilities Used at the Oner Modane Centre for Icing Tests", AGARD Advisory Report No. 127, November 1978, pp. A6-1 to A6-23

58. Theodorsen, T., "Theory of Wing Sections of Arbitrary Shape", NACA Rept. 411, 1931

59. Theodorsen, T. and Garrick, I. E., "General Potential Theory of Arbitrary Wing Sections", NACA Rept. 452, 1933

60. Woan, C. J., "Fortran Programs for Calculating the Incompressible Potential Flow About a Single Element Airfoil Using Conformal Mapping", The Ohio Stae University, Aeronautical and Astronautical Research Laboratory, TR AARL 80-02, January 1980

61. Eppler, Richard and Somers, Dan M., "A Computer Program for the Design and Analysis of Low-Speed Airfoils", NASA TM 80210, August 1980

62. Lapidus, Leon and Seinfield, John H., "Numerical Solution of Ordinary Differential Equations", Academic Press, New York, 1971, pp. 267-293

63. Gear, C. W., "The Automatic Integration of Ordinary Differential Equations", Comm. ACM 14, March 1971, pp. 176-179

64. Gear, C. W., "DIFSUB for Solution of Ordinary Differential Equations", Comm. ACM 14, March 1971, pp. 185-190

65. Szelazek, C. A. and Hicks, Raymond W., "Upper Surface Modifications for C Improvement of Selected NACA 6-Series Airfoils", NASA TM 78603, August 1979

66. Brumby, Ralph E., "Wing Surface-Roughness, Cause and Effect", DC Flight Approach, January 1979, pp. 2-7

67. Lozowski, E. P. and Oleskiw, M. M., "Computer Simulation of Airfoil Icing Without Runback", AIAA Paper No. 81-0402 presented at the 19th Aerospace Sciences Meeting, St. Louis Missouri, January 12-15 1981

68. Shaw, R. J., Private Communication with M. B. Bragg, November 1980

69. Lee, John D., Gregorek, G. M., and Korkan, K. D., "Testing Techniques and Interference Evaluation in the OSU Transonic Airfoil Facility", AIAA Paper No. 78-1118 presented at the 11th Fluid and Plasma Dynamics Conference, Seattle Washington, July 10-12 1978

70. Freuler, R. J. and Petrie, S. L., "An Effective Mix of Minicomputer Power and Large Scale Computers for Complex Fluid Mechanics Calculations", Paper presented at the joint Conference of the American Chemical Society and Chemical Institute of Canada, June 1977

71. Freuler, R. J., "State-of-the-Art Data Acquisition and Reduction Techniques for Transonic Airfoil Testing", Paper presented at the International Congress on Instrumentation in Aerospace Simulation Facilities, Ottawa Canada, Sept. 1975

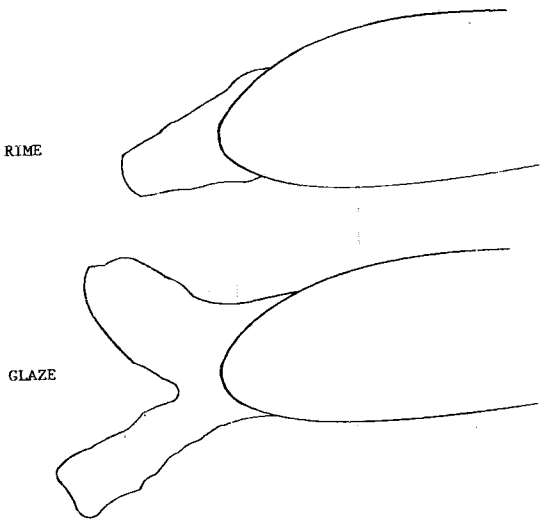

FIGURE 1. TYPICAL RIME AND GLAZE ICE ACCRETIONS ON AN AIRFOIL

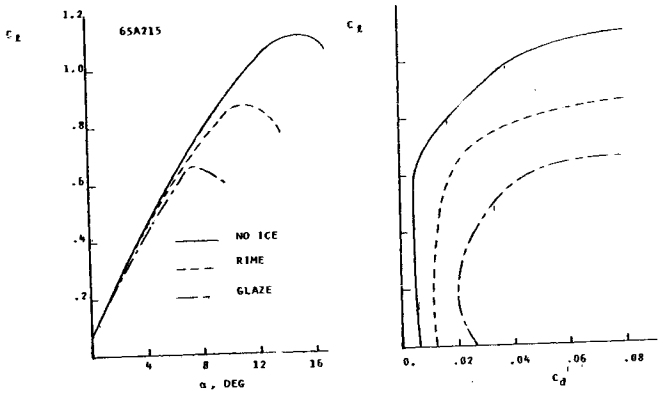

FIGURE 2. EFFECT OF ICE ON THE AERODYNAMIC CHARACTERISTICS OF A NACA 65A215 AIRFOIL

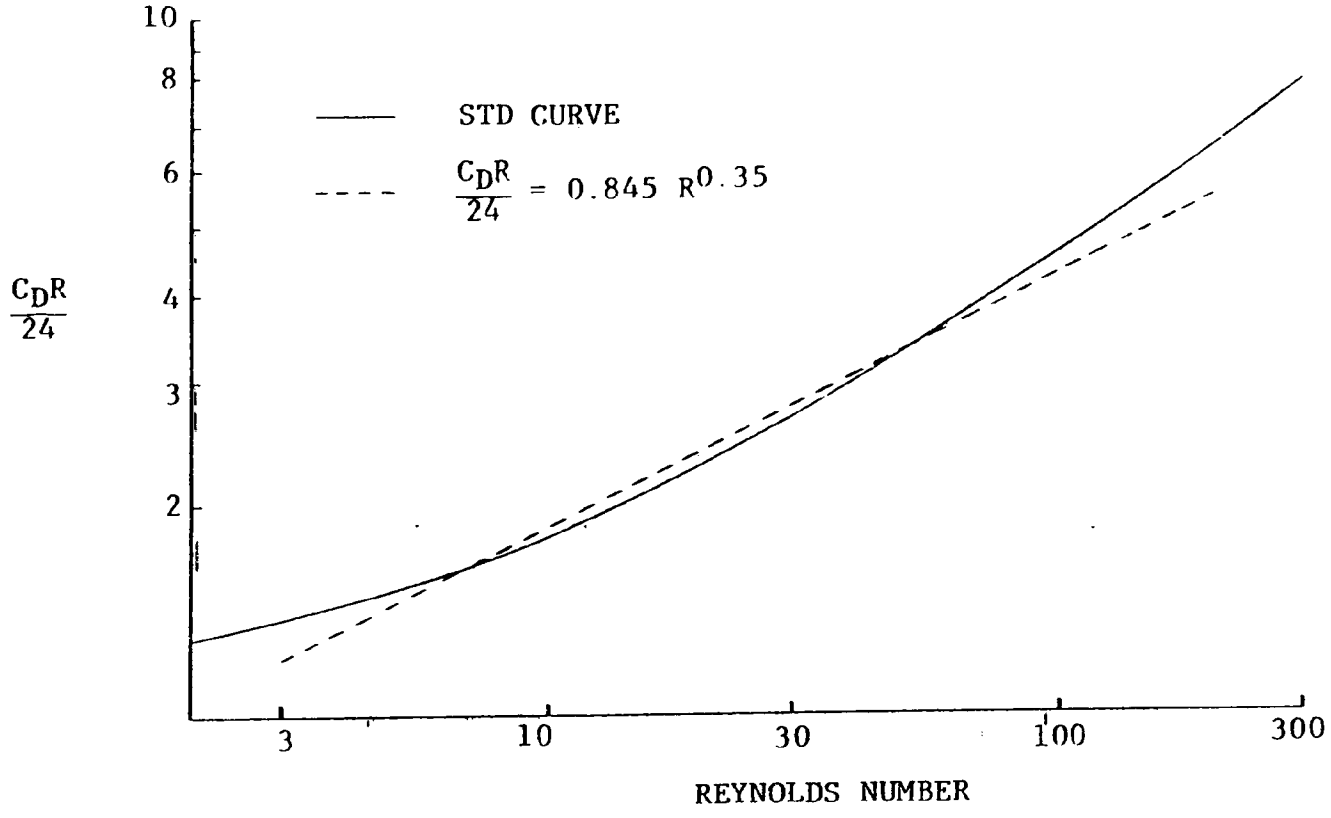

FIGURE 3. STANDARD SPHERE DRAG CURVE AND APPROXIMATION

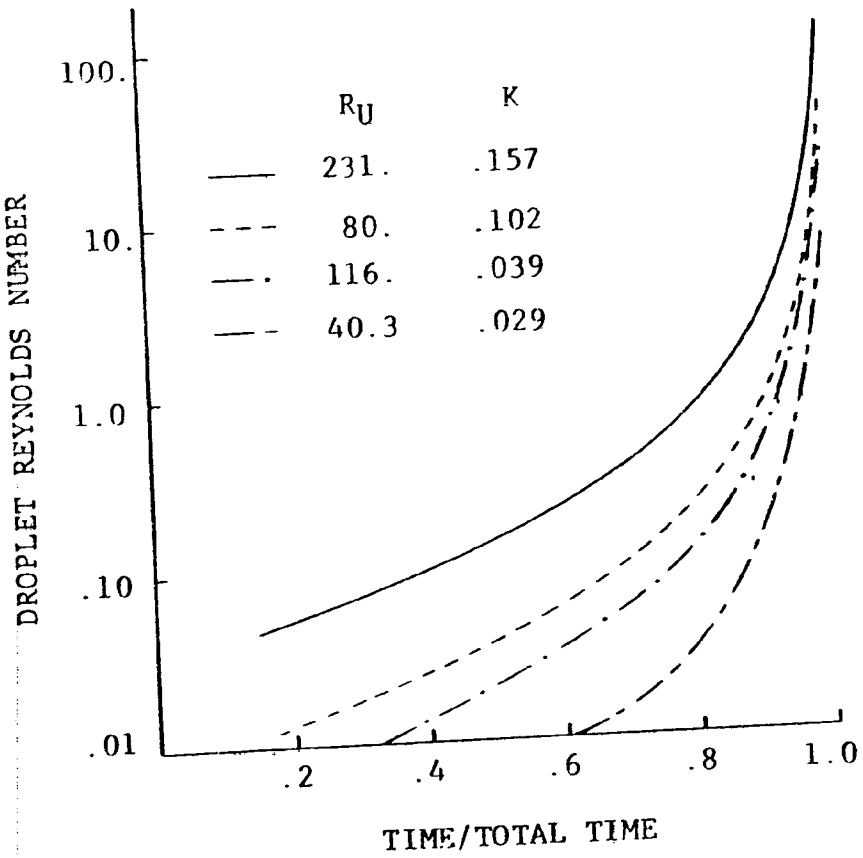

FIGURE 4. TYPICAL REYNOLDS NUMBER EXPERIENCED DURING DROPLET TRAJECTORY.

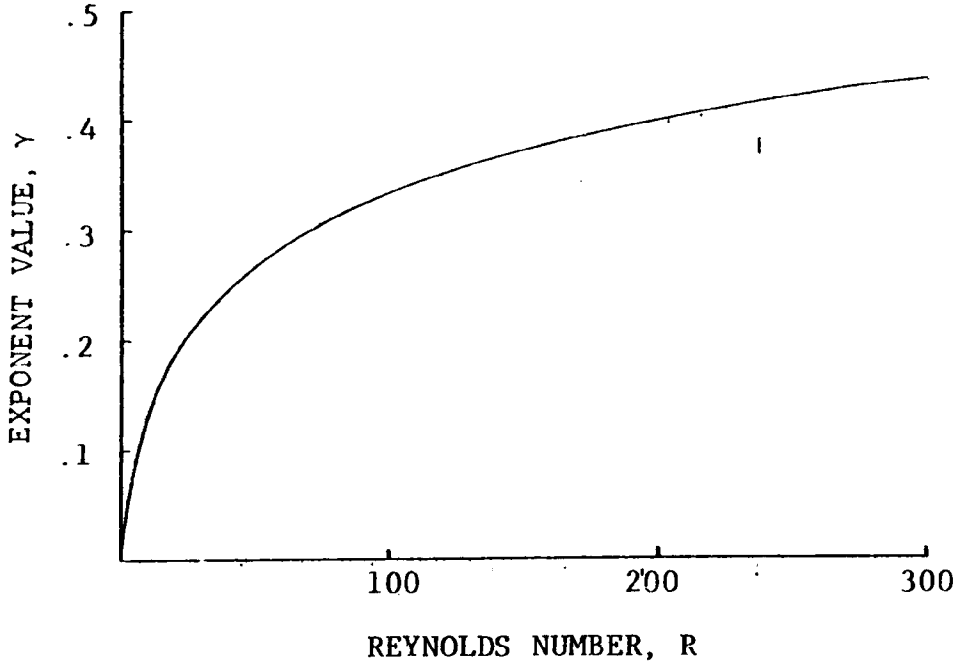

FIGURE 5. APPROXIMATE DRAG LAW EXPONENT FOR BEST FIT IN REYNOLDS NUMBER RANGE 0 TO R.

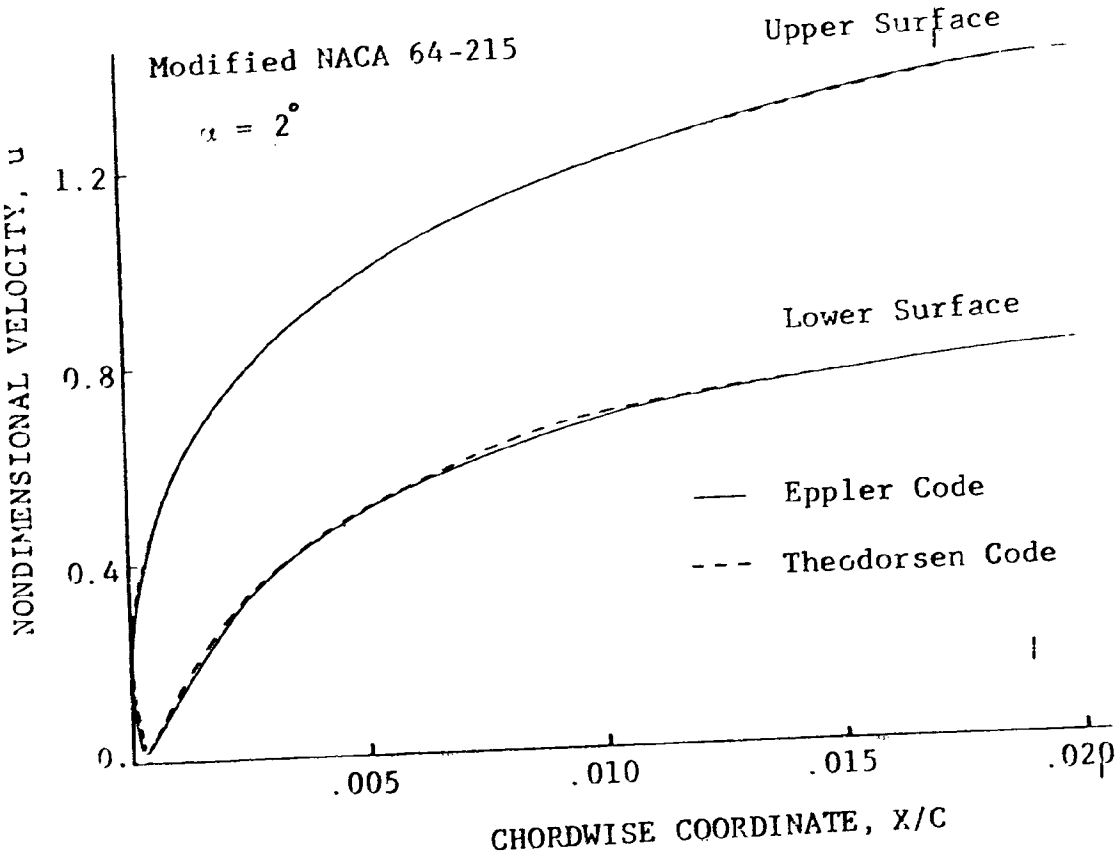

FIGURE 6. COMPARISON OF PREDICTED LEADING EDGE VELOCITY DISTRIBUTIONS FROM EPPLER AND THEODORSEN COMPUTER CODES

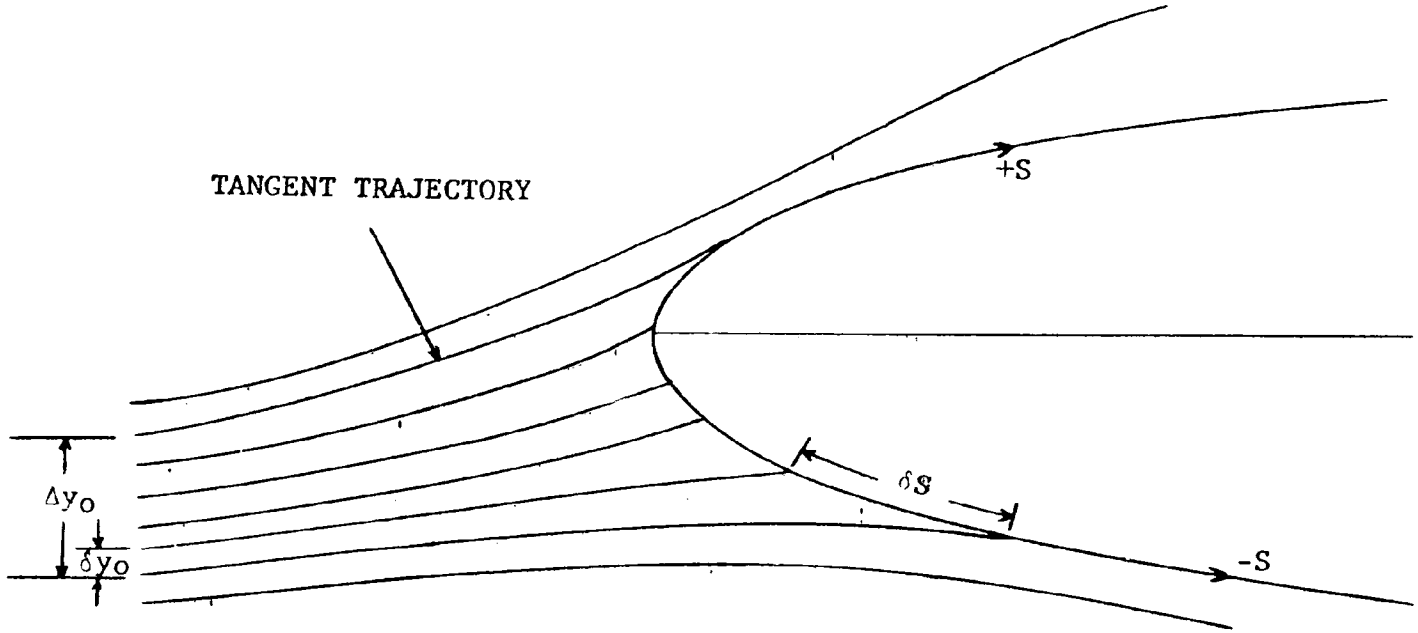

FIGURE 7. DROPLET TRAJECTORIES USED TO CALCULATE THE IMPINGEMENT EFFICIENCY

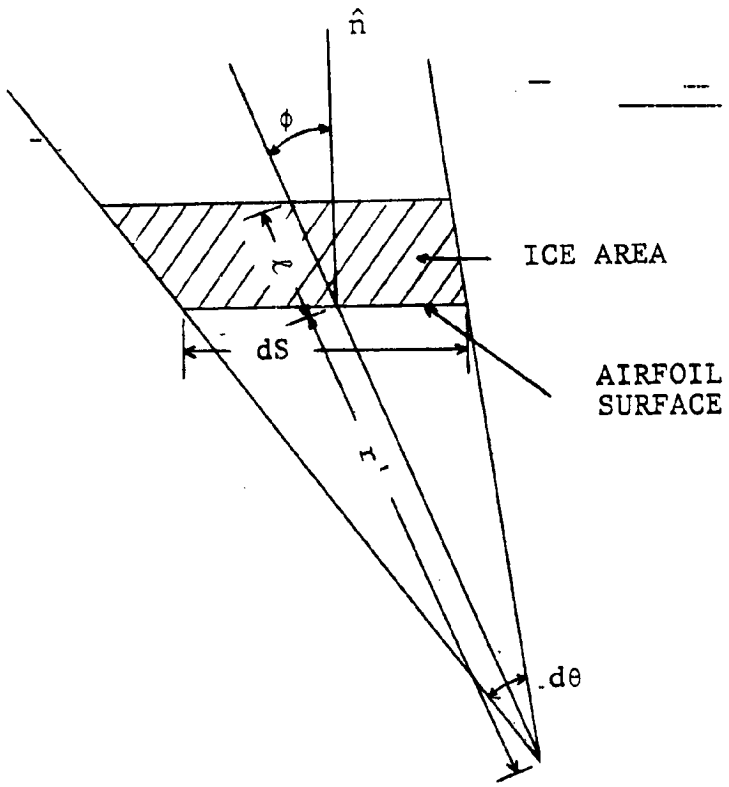

FIGURE 8. GEOMETRY OF THE ICE GROWTH CALCULATION

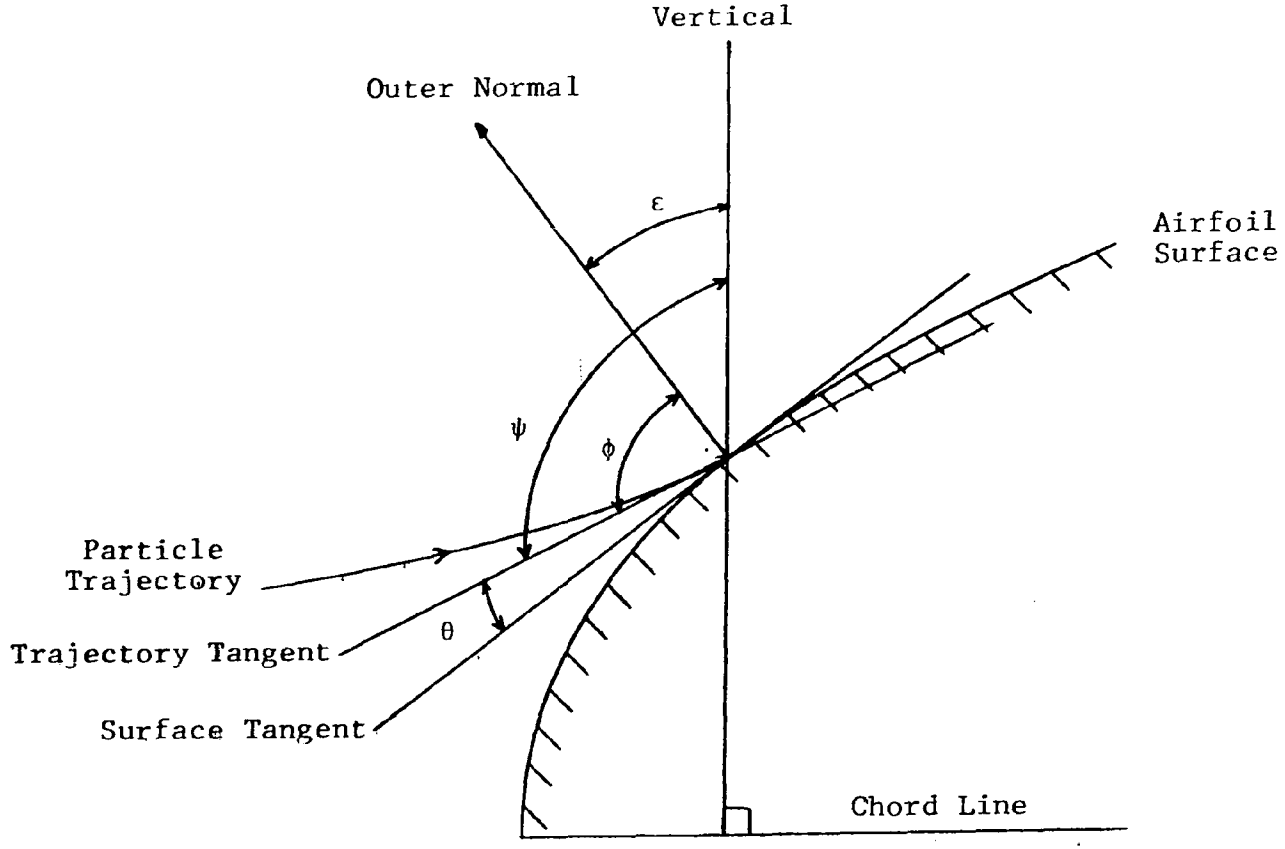

FIGURE 9. DEFINITION OF THE GEOMETRY INVOLVED WHEN A PARTICLE IMPINGES ON THE AIRFOIL SURFACE

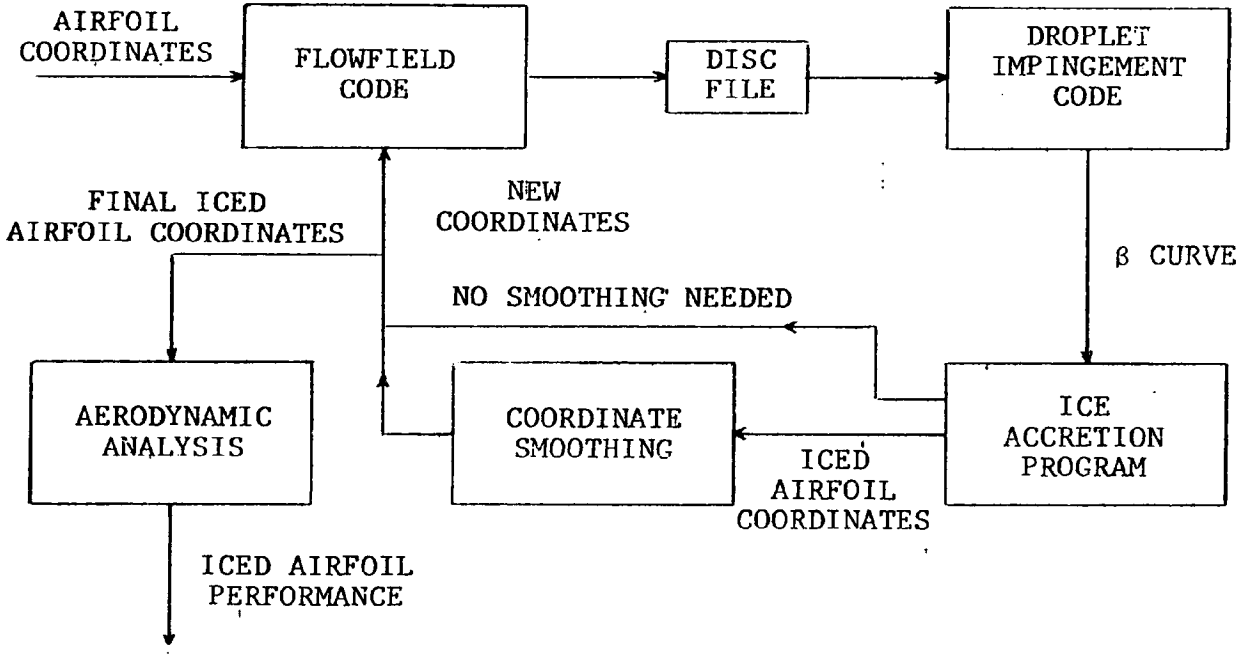

FIGURE 10. FLOWCHART FOR THE RIME ICE METHODOLOGY

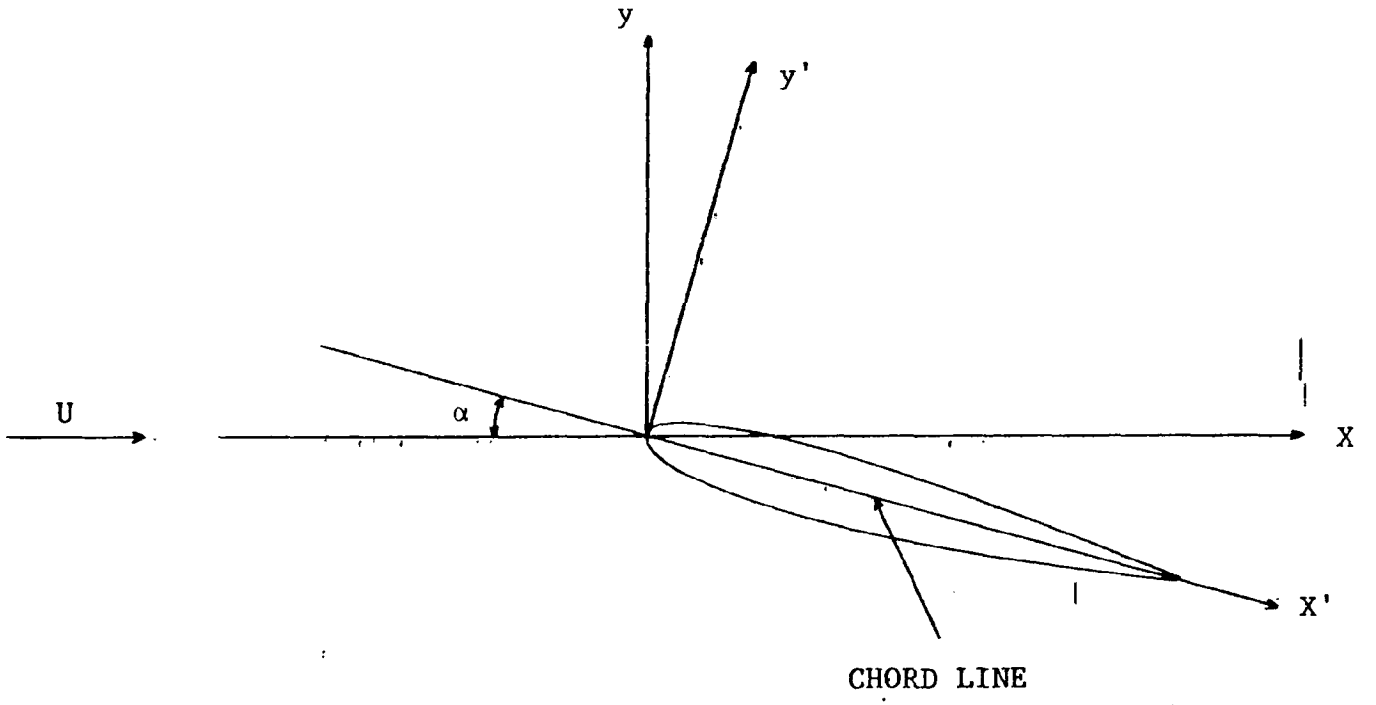

FIGURE 11. COORDINATE SYSTEMS USED IN THE TRAJECTORY CALCULATION

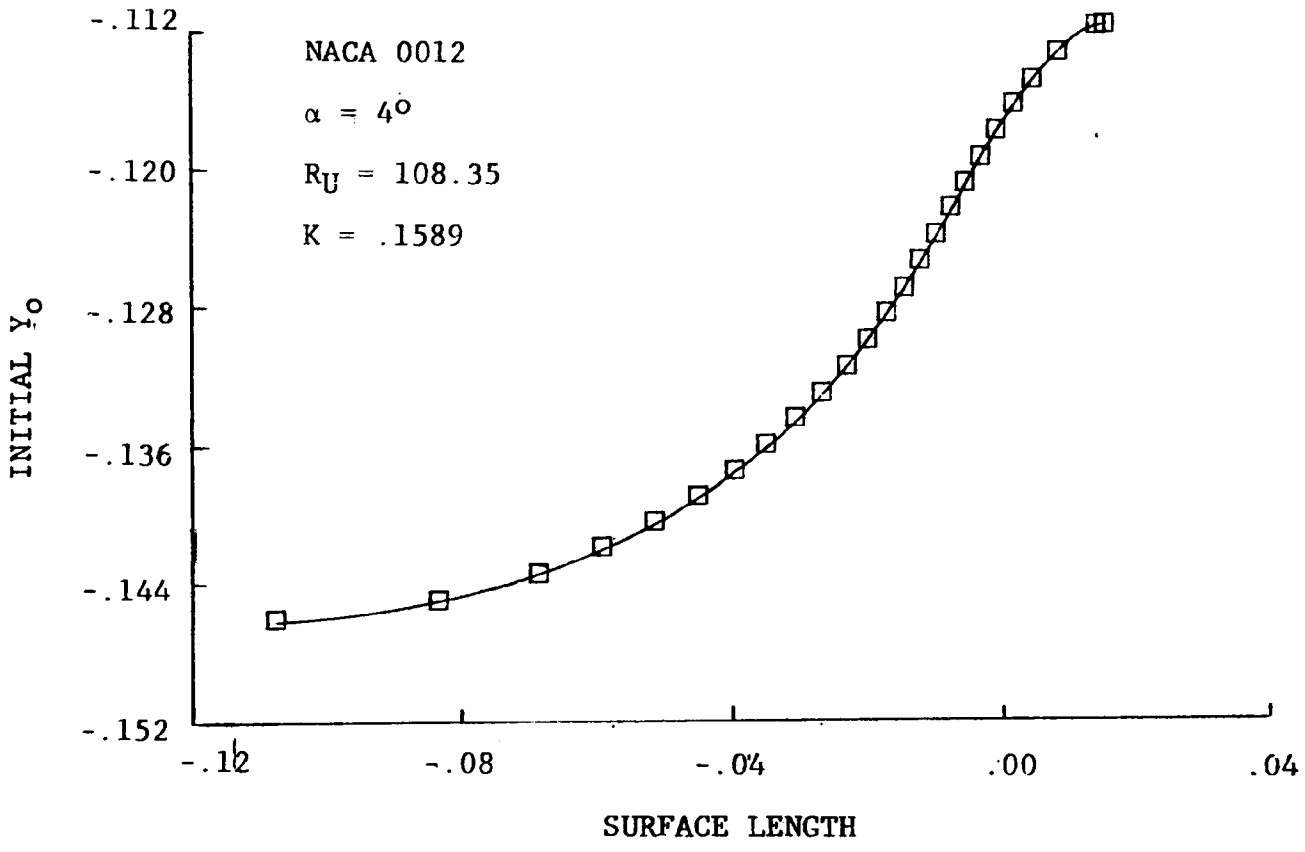

FIGURE 12. DROPLET INITIAL Y COORDINATE IN THE FREE STREAM AS A FUNCTION OF IMPINGEMENT POINT ON THE AIRFOIL

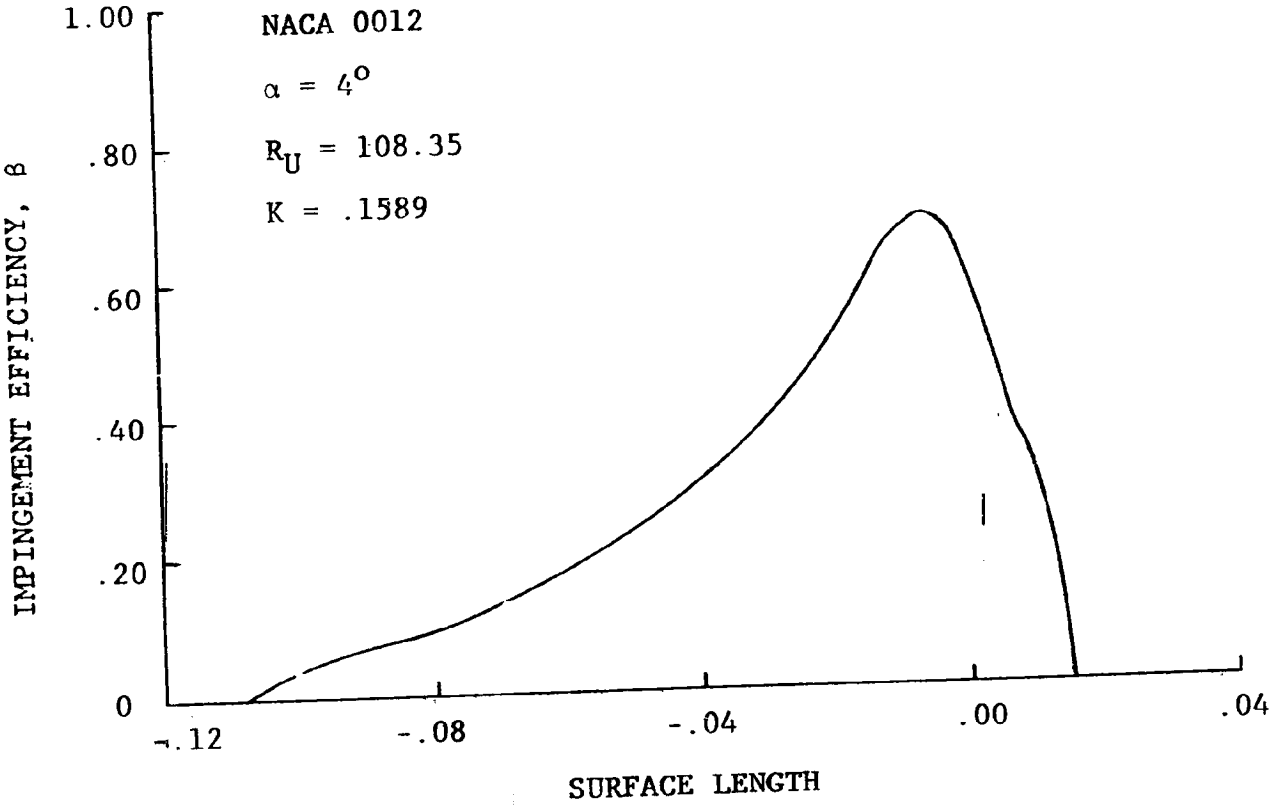

FIGURE 13. IMPINGEMENT EFFICIENCY AS A FUNCTION OF AIRFOIL SURFACE LENGTH (Derivative of the Curve in Figure 11)

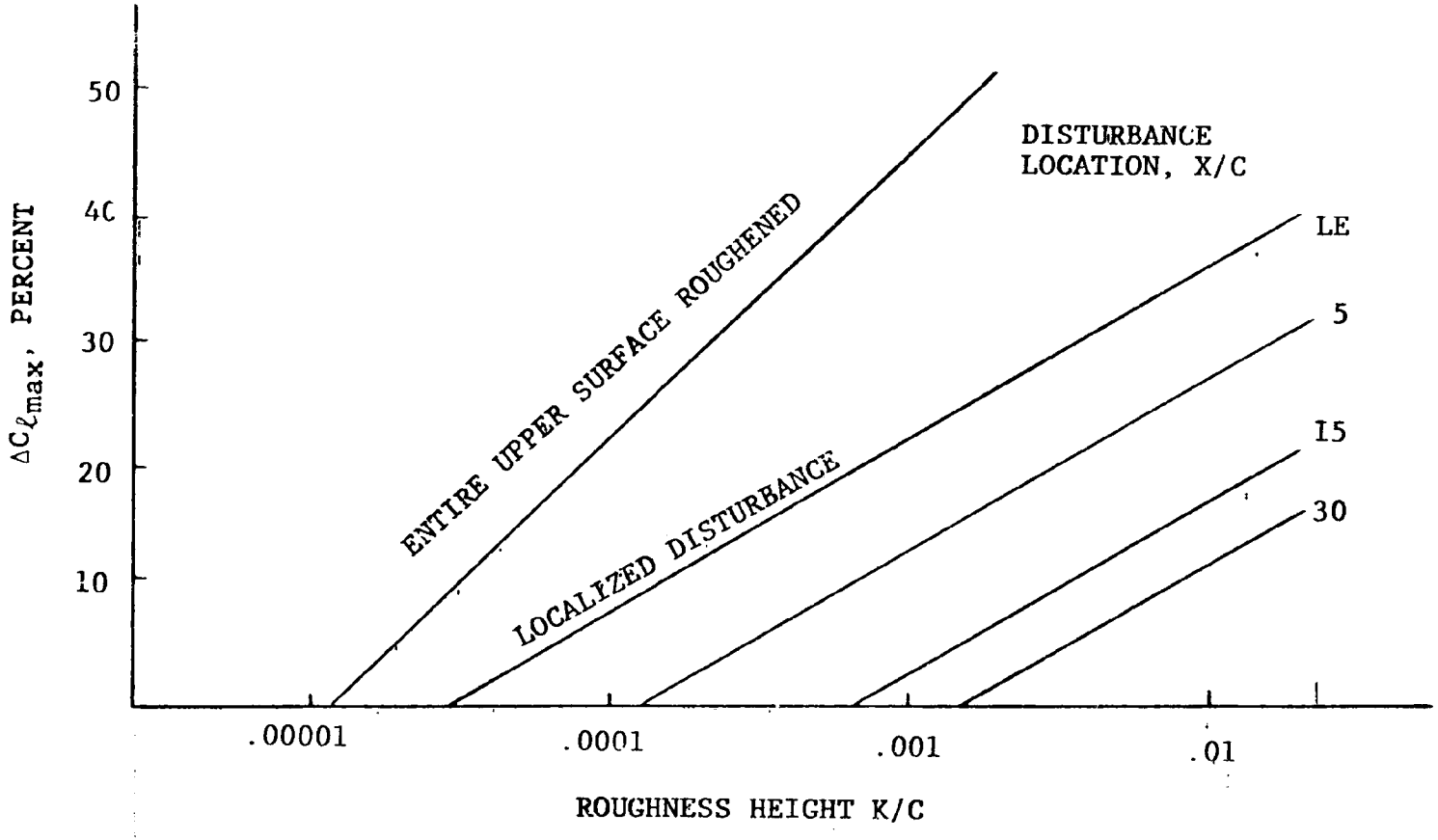

FIGURE 14. REDUCTION OF MAXIMUM LIFT COEFFICIENT DUE TO WING SURFACE ROUGHNESS

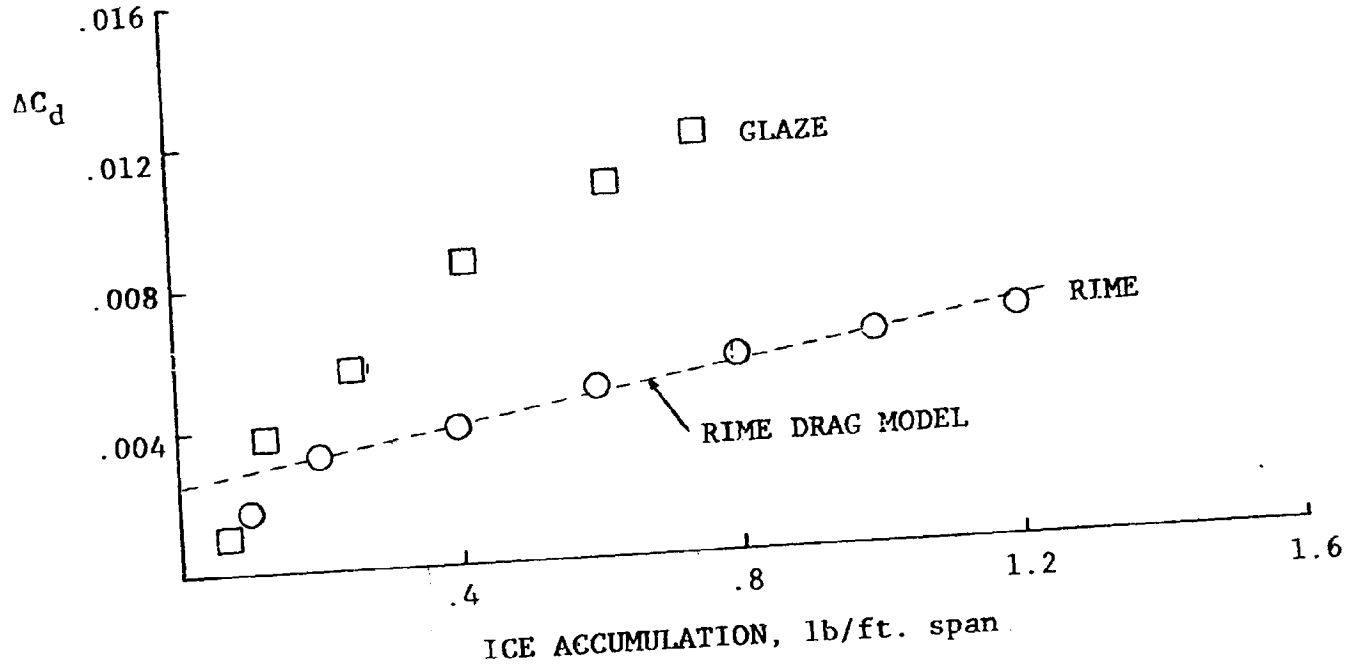

FIGURE 15. MEASURED INCREASE IN AIRFOIL DRAG FOR RIME AND GLAZE ICE COMPARED TO THE RIME ICE DRAG MODEL

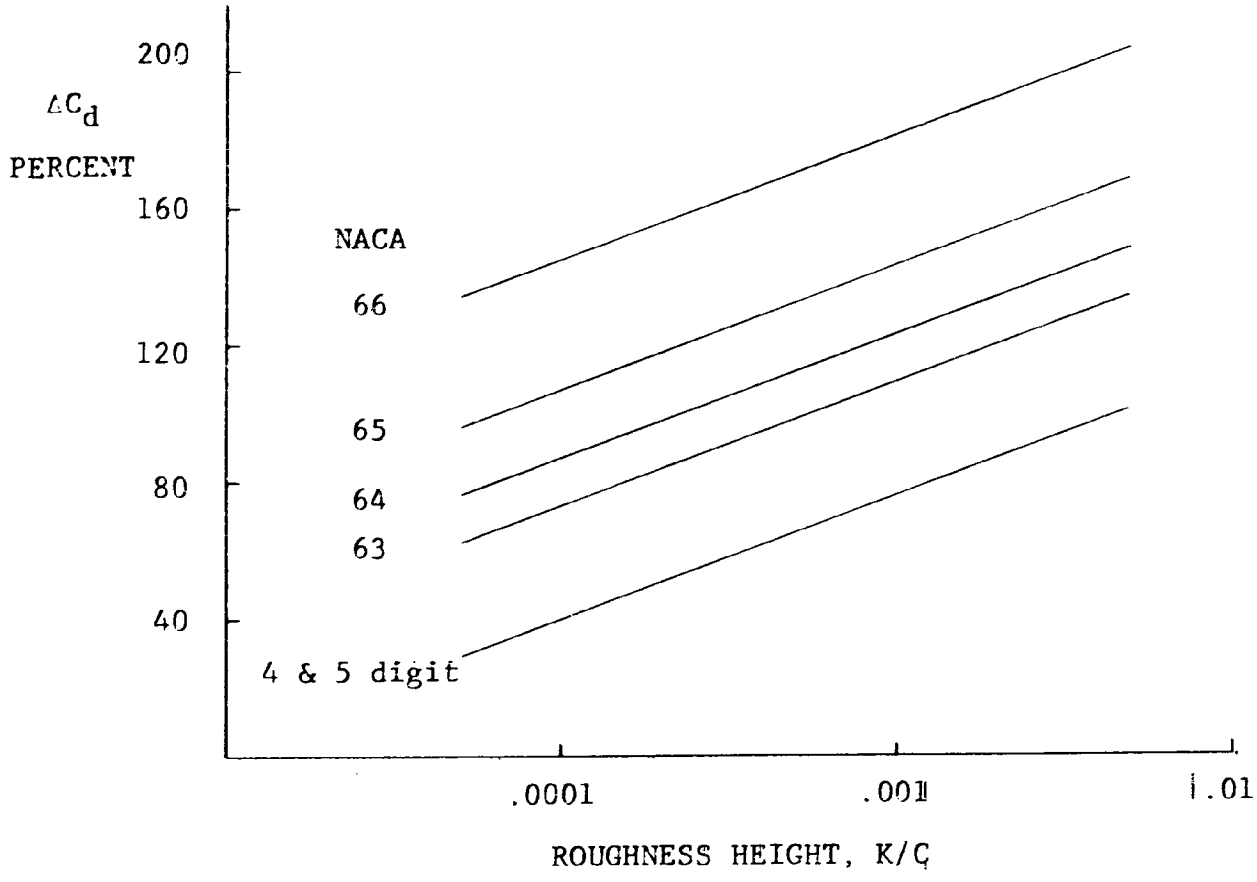

FIGURE 16. EFFECT OF LEADING EDGE ROUGHNESS ON AIRFOIL DRAG

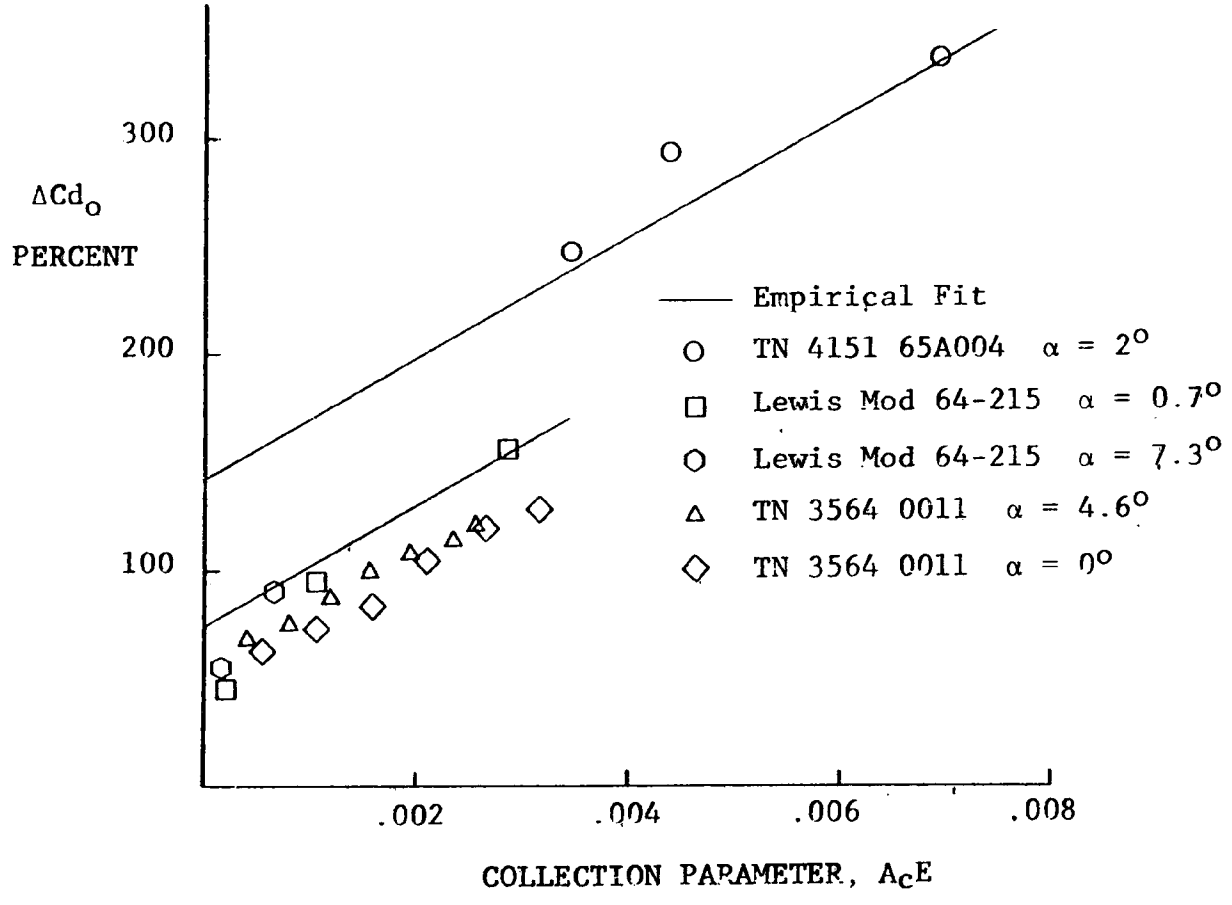

FIGURE 17. EMPIRICAL FIT TO ICED AIRFOIL DATA

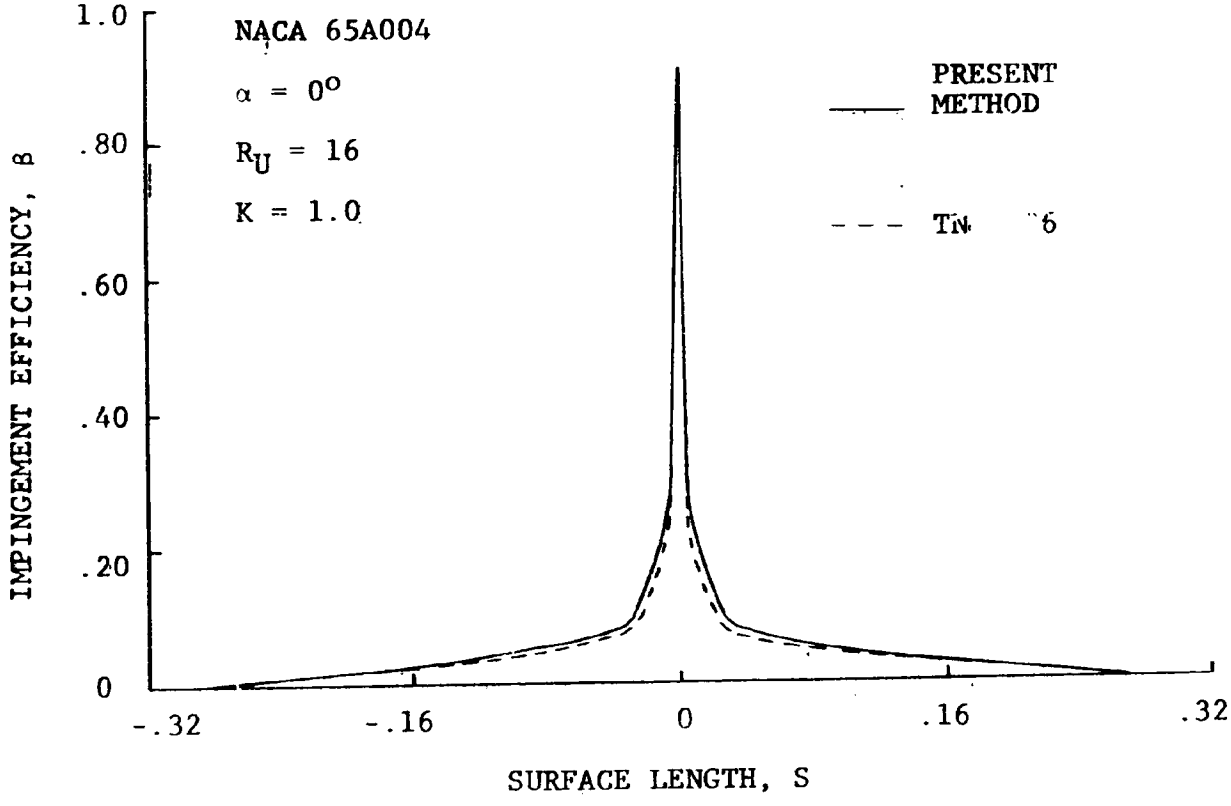

FIGURE 18. COMPARISON OF THE PRESENT METHOD TO NACA TN 3586 FOR IMPINGEMENT EFFICIENCY ON A NACA 65A004 AIRFOIL

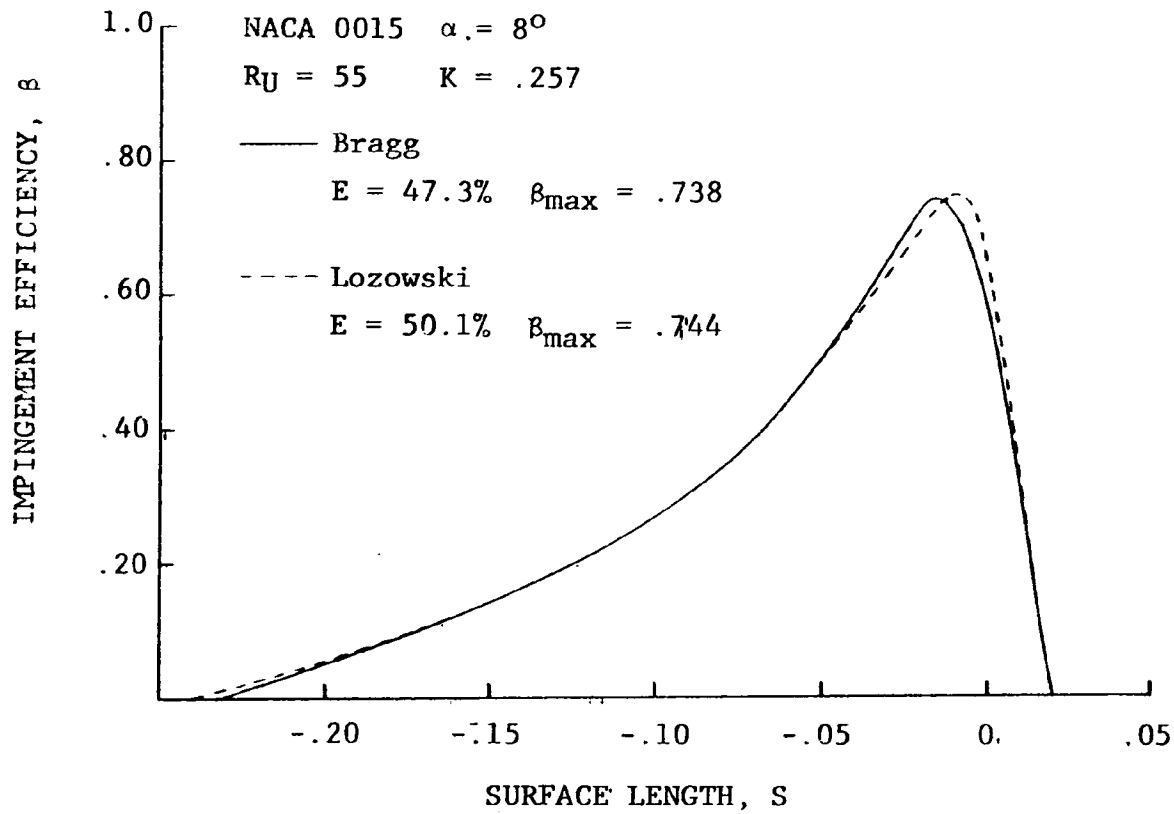

FIGURE 19. COMPARISON OF THE PRESENT METHOD TO THAT OF LOZOWSKI FOR THE IMPINGEMENT EFFICIENCY OF A NACA 0015 AIRFOIL

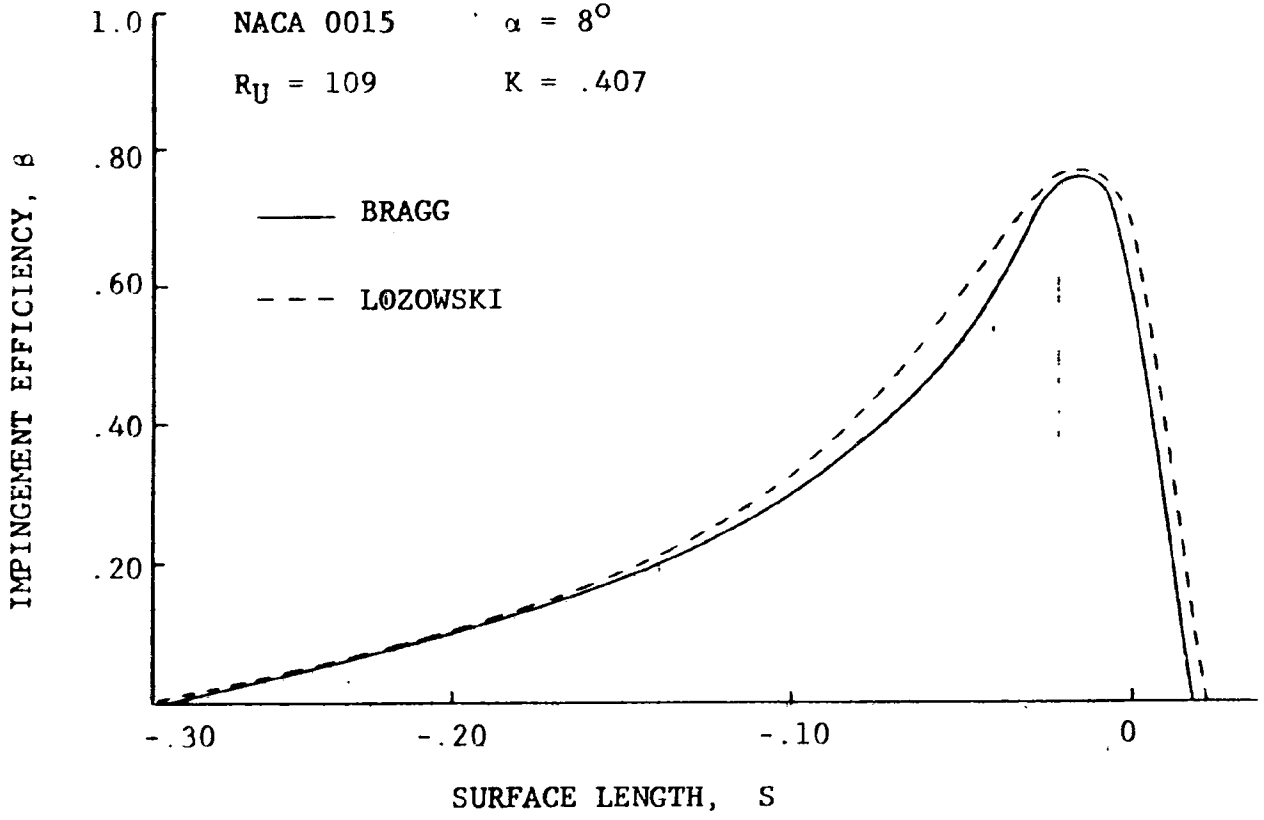

FIGURE 20. PRESENT METHOD FOR CALCULATING IMPINGEMENT EFFICIENCY COMPARED TO LOZOWSKI'S WITH DRAG DUE TO DROPLET ACCELERATION

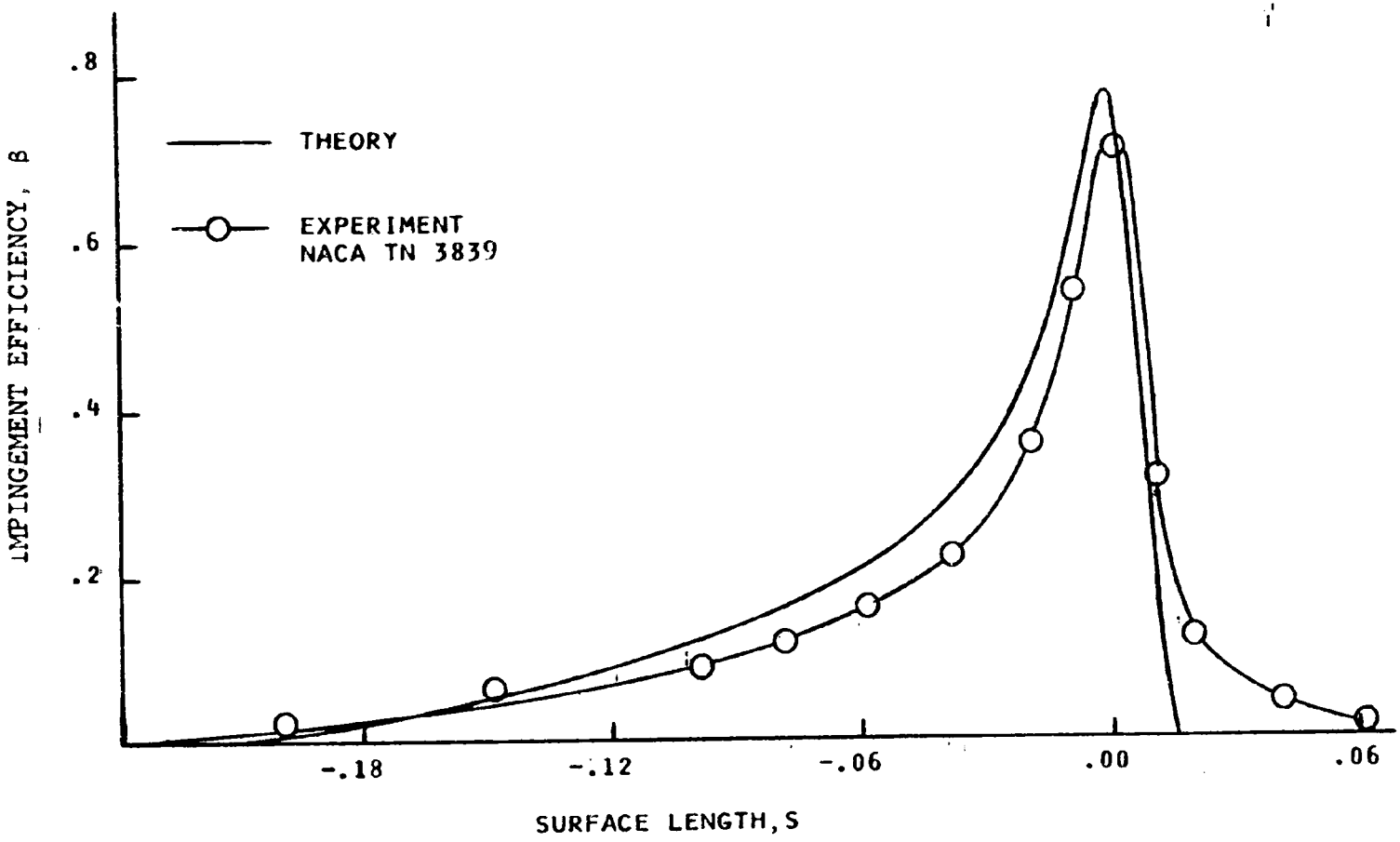

FIGURE 21. COMPARISON OF THEORETICAL IMPINGEMENT VALUES WITH EXPERIMENTAL RESULTS

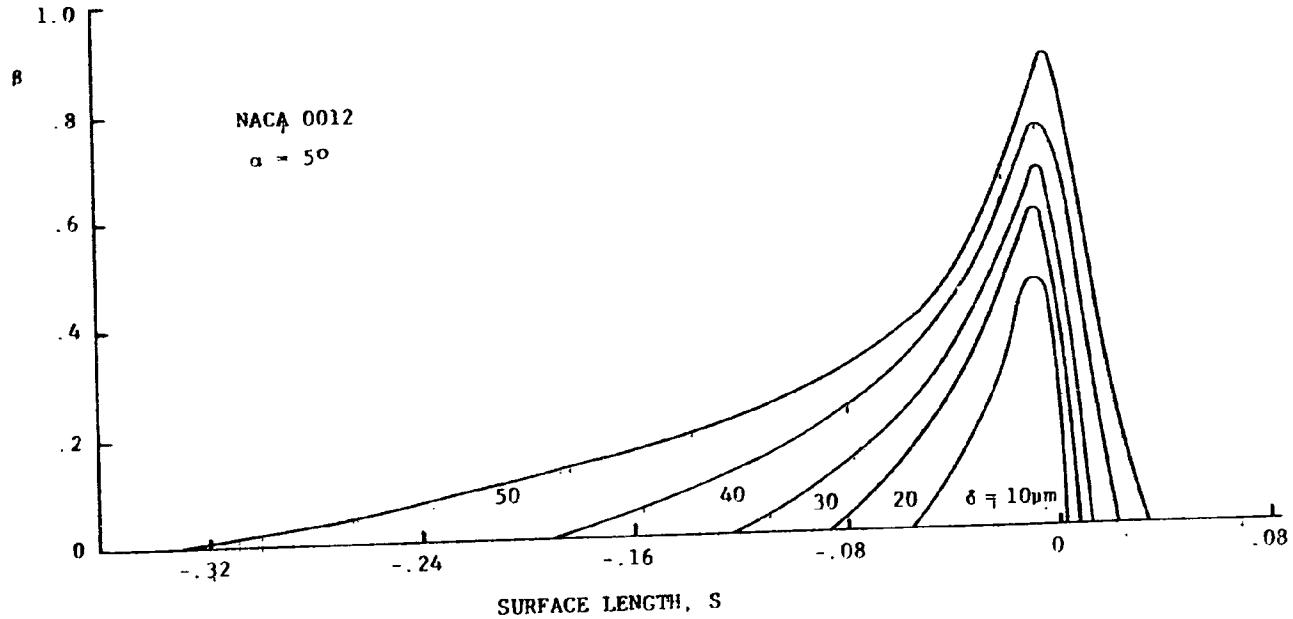

FIGURE 22. EFFECT OF DROPLET DIAMETER ON IMPINGEMENT EFFICIENCY

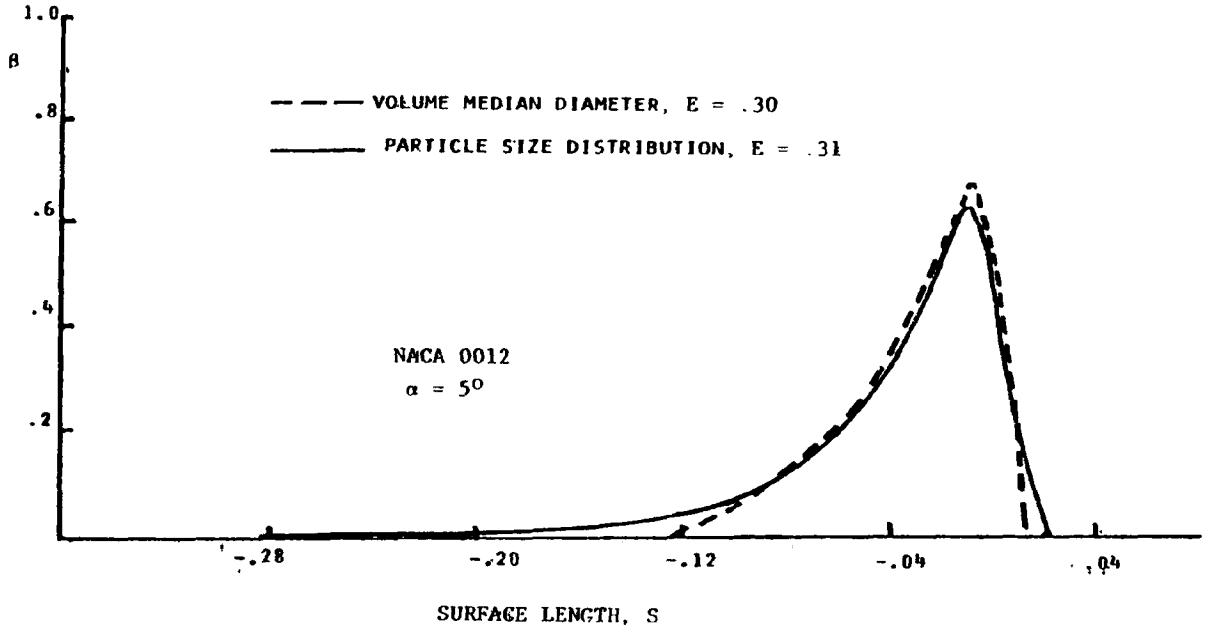

FIGURE 23. EVALUATION OF THE VOLUME MEDIAN DIAMETER APPROXIMATION FOR PREDICTING IMPINGEMENT EFFICIENCY

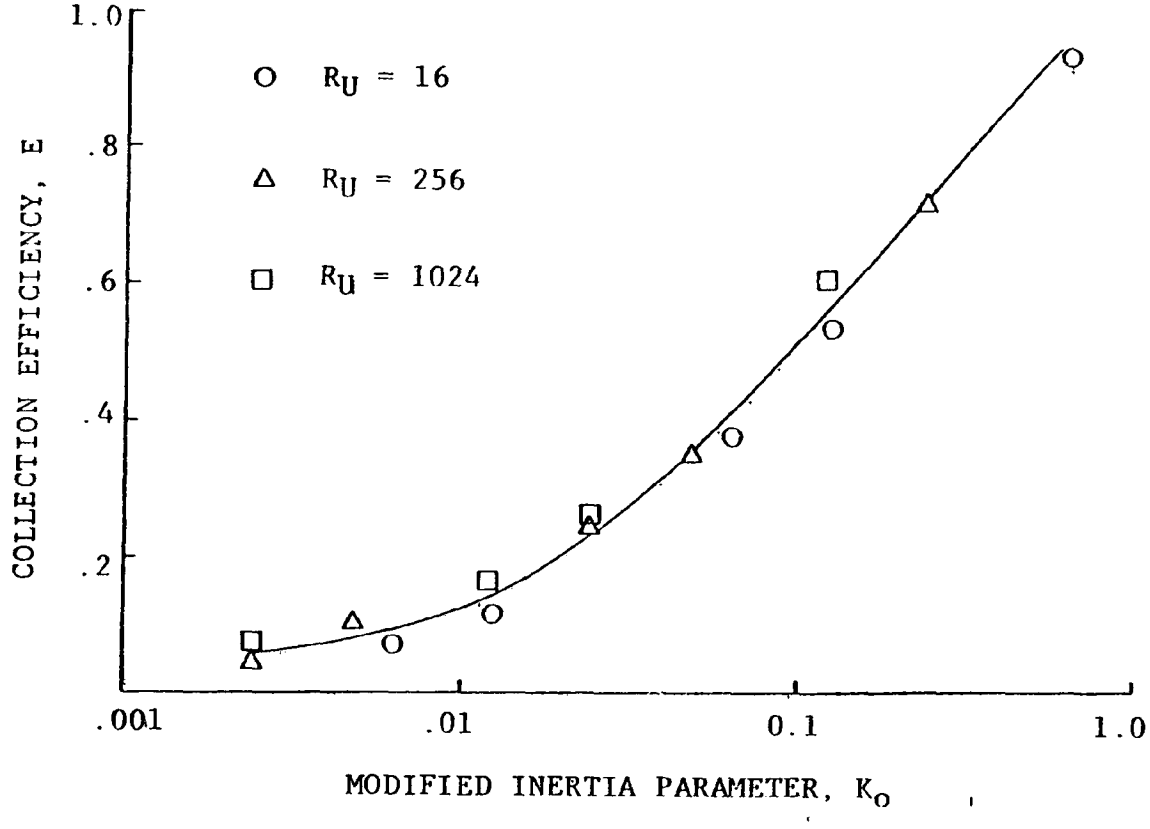

FIGURE 24. COLLECTION EFFICIENCY OF A NACA 65A004 AIRFOIL AS A FUNCTION OF K_o.

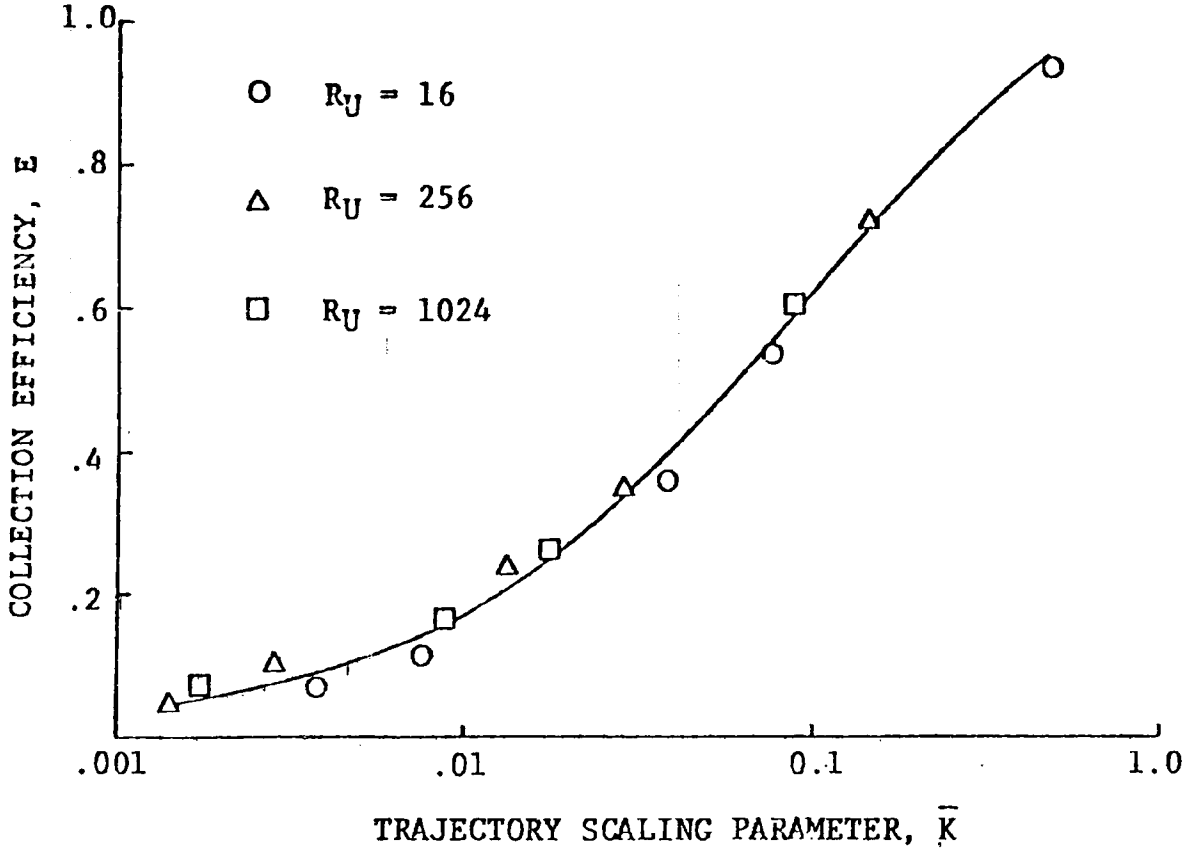

FIGURE 25. COLLECTION EFFICIENCY OF A NACA 65A004 AIRFOIL AS A FUNCTION OF $\bar{K}$.

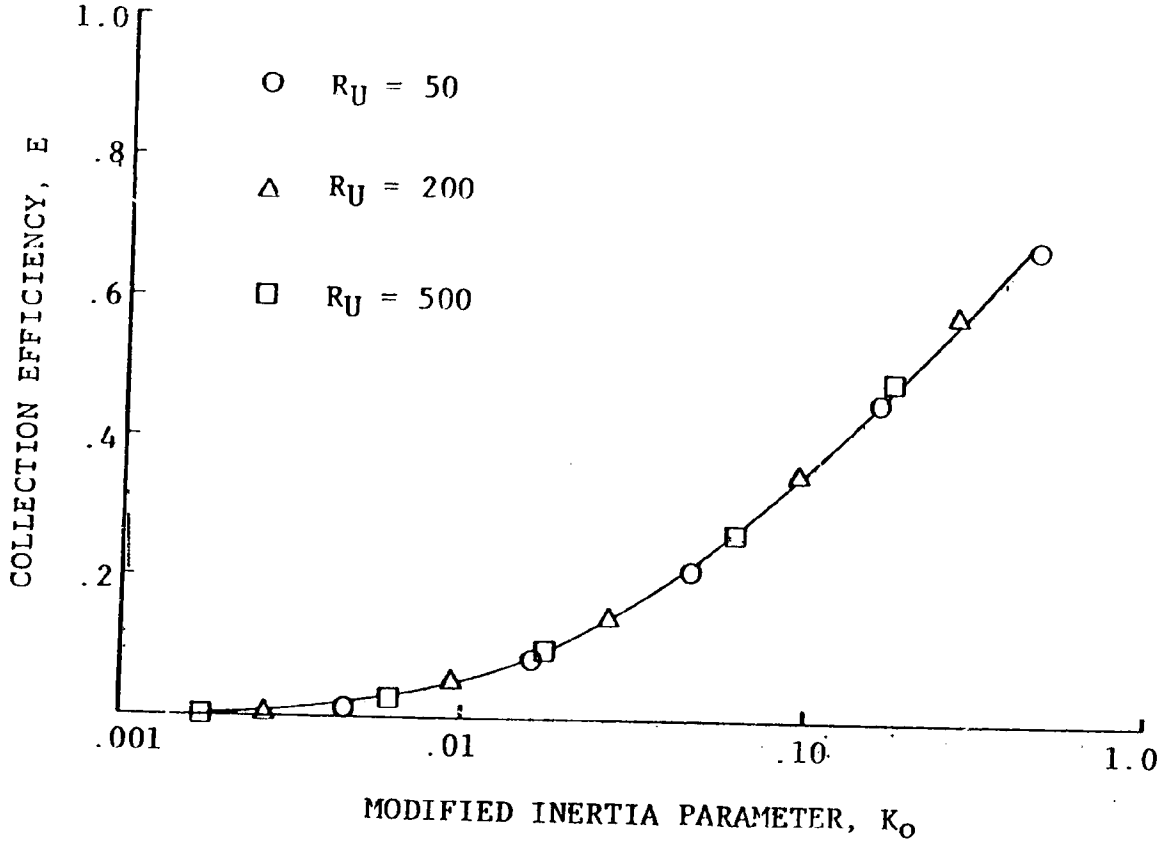

FIGURE 26. COLLECTION EFFICIENCY OF A NACA 0012 AIRFOIL AS A FUNCTION OF K_o.

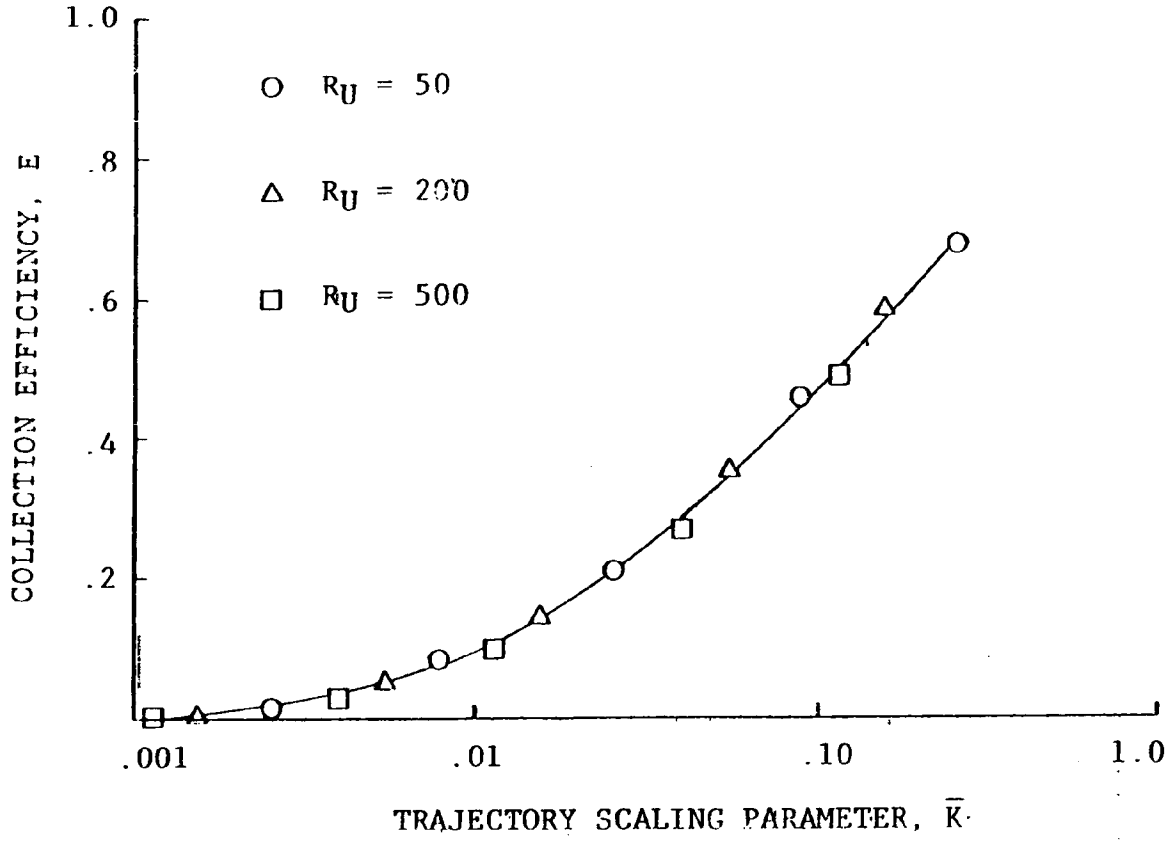

FIGURE 27. COLLECTION EFFICIENCY OF A NACA 0012 AIRFOIL AS A FUNCTION OF $\bar{K}$.

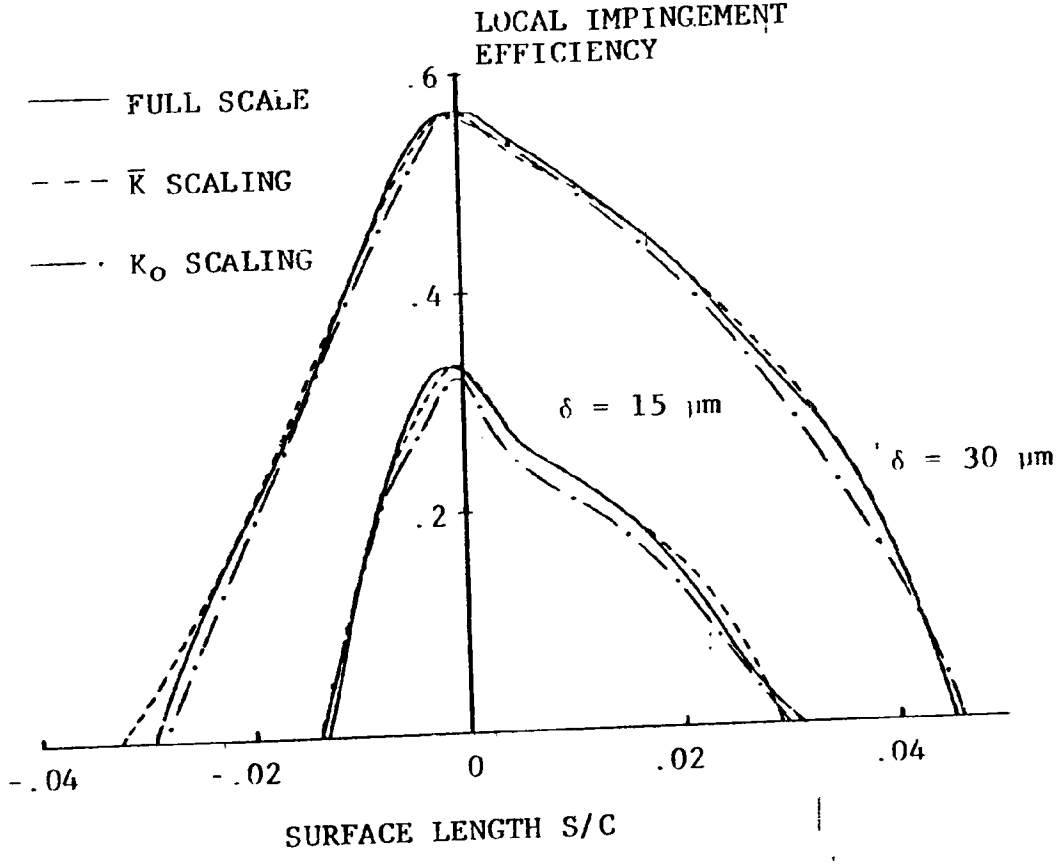

FIGURE 28. COMPARISON OF K_o AND $\bar{K}$ IN SCALING THE DROPLET IMPINGEMENT EFFICIENCY OF AN AIRFOIL.

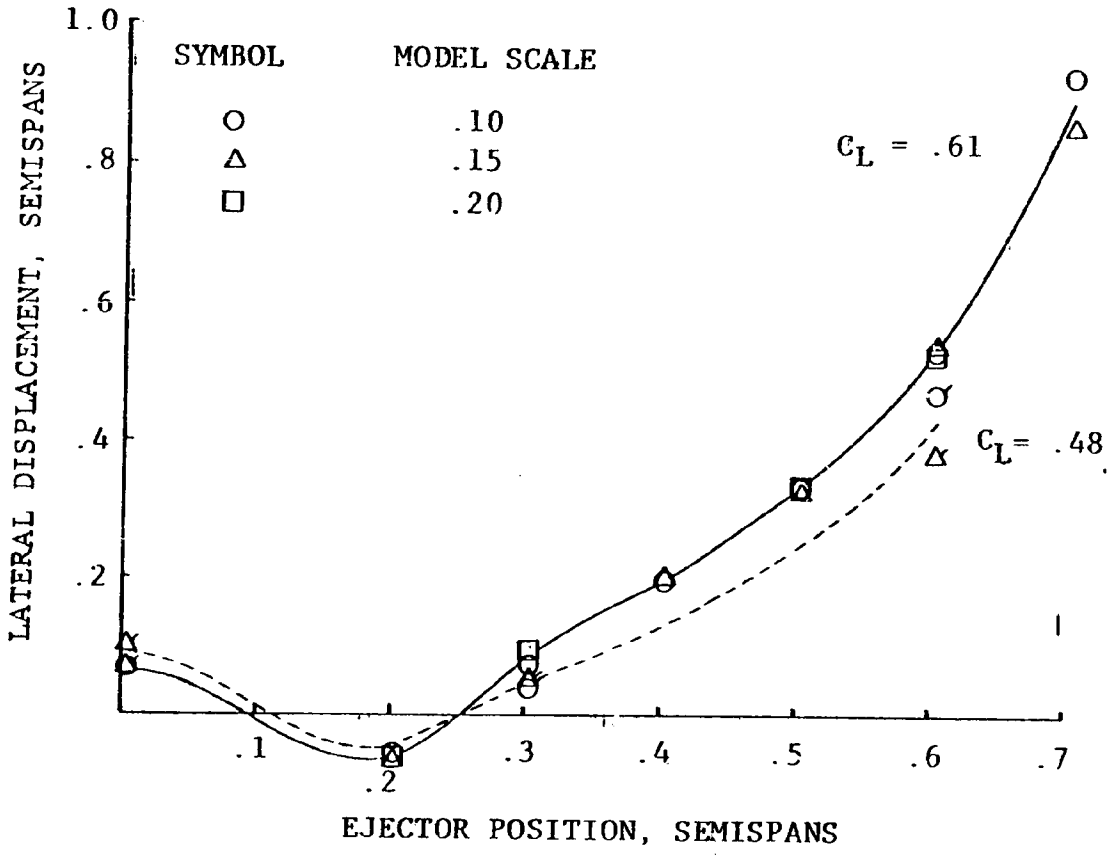

FIGURE 29. EXPERIMENTAL RESULTS SCALING DROPLET TRAJECTORIES IN AN AIRCRAFT WAKE.

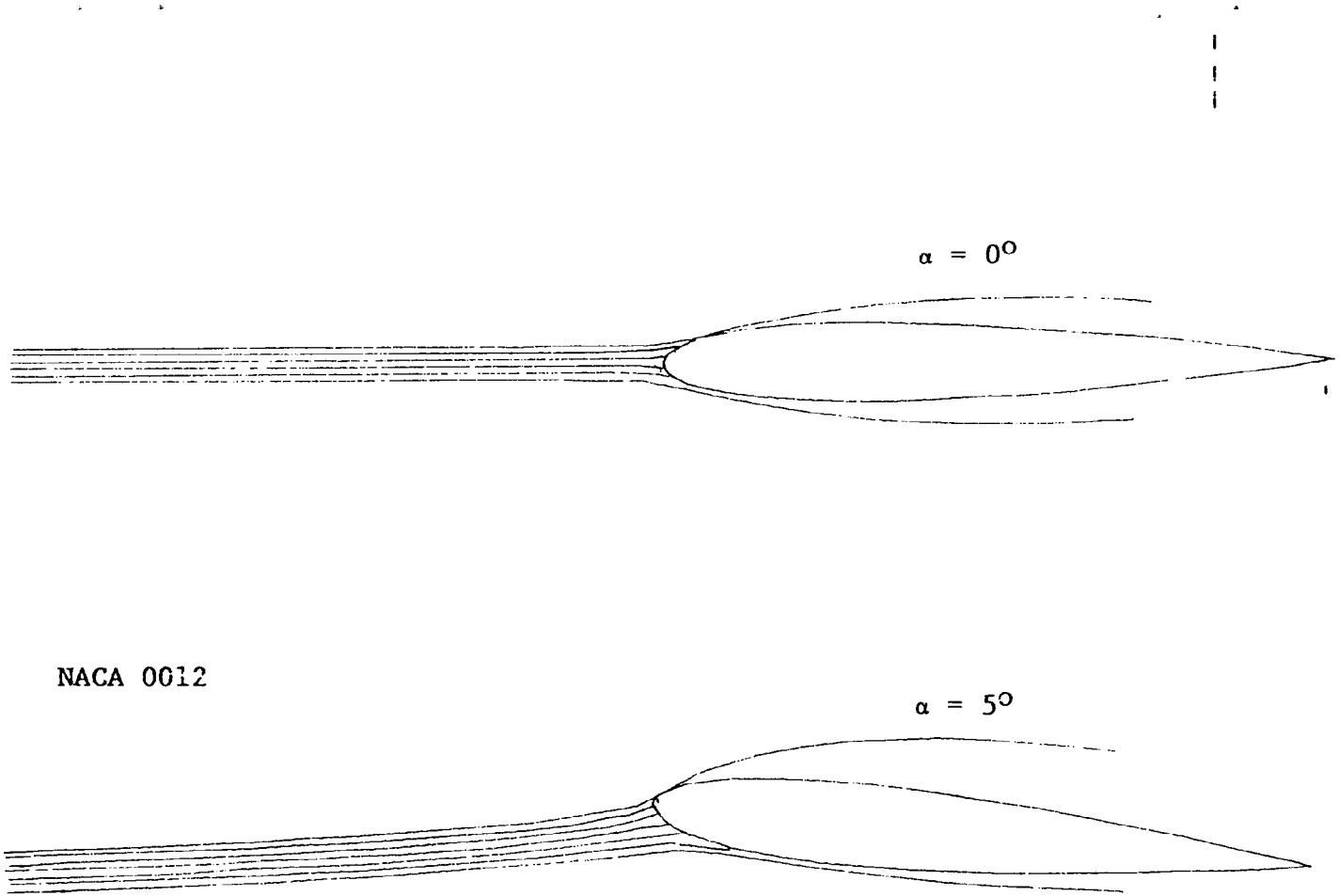

FIGURE 30. DROPLET TRAJECTORIES ABOUT A NACA 0012 AIRFOIL AT ZERO AND FIVE DEGREES ANGLE OF ATTACK

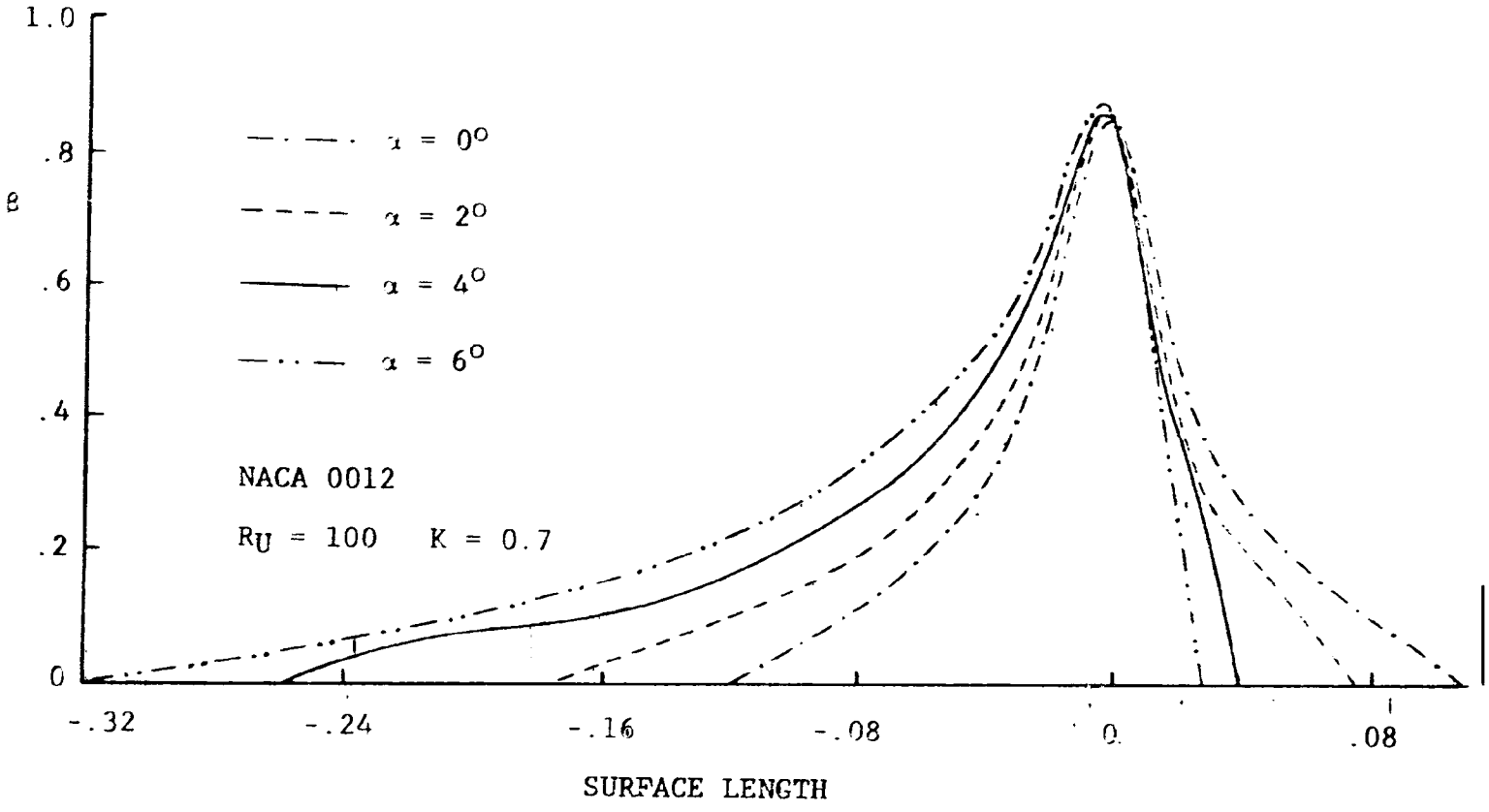

FIGURE 31. IMPINGEMENT EFFICIENCY OF A NACA 0012 AIRFOIL AT FOUR DIFFERENT ANGLES OF ATTACK

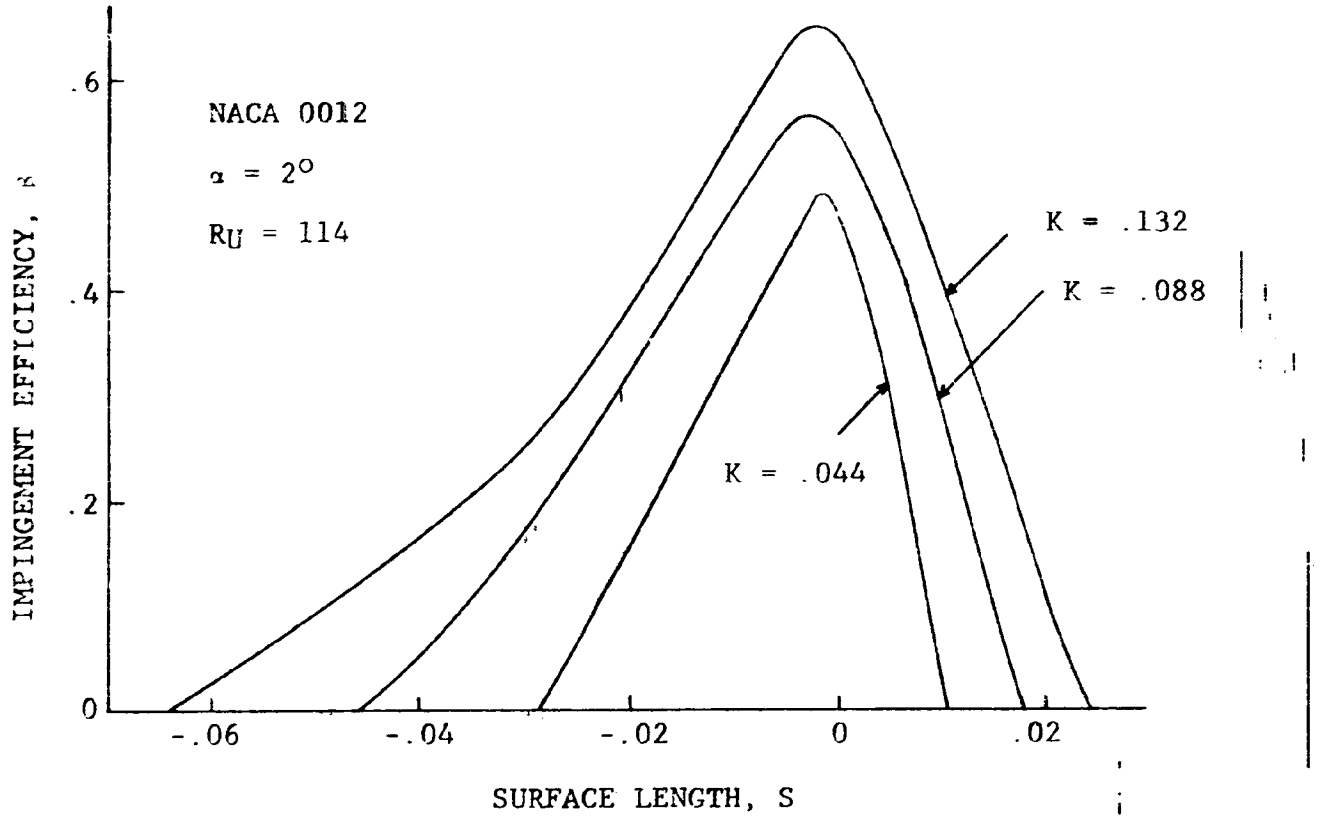

FIGURE 32. EFFECT OF THE INERTIA PARAMETER ON THE IMPINGEMENT EFFICIENCY

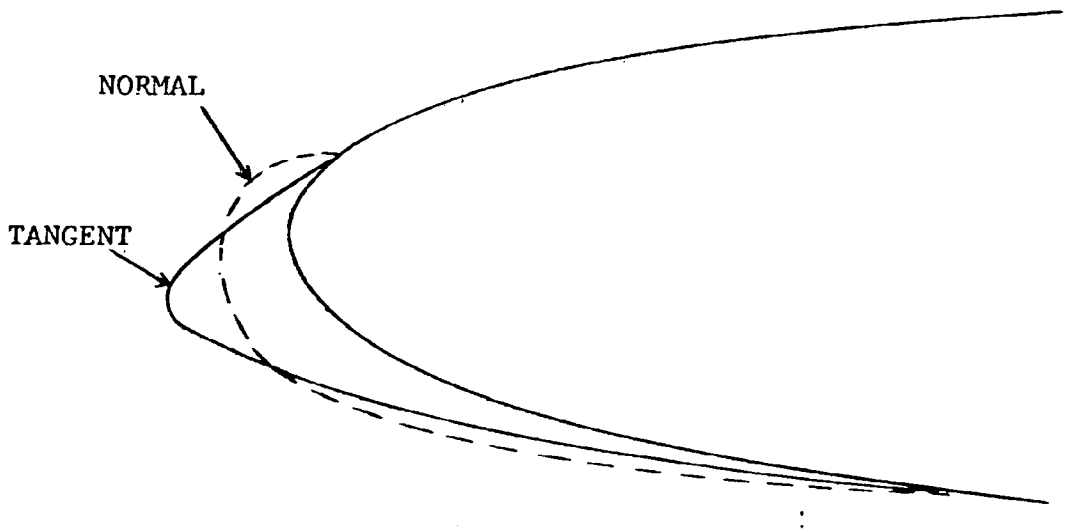

FIGURE 33. EFFECT OF THE ASSUMED DIRECTION OF GROWTH ON THE PREDICTED ICE SHAPE

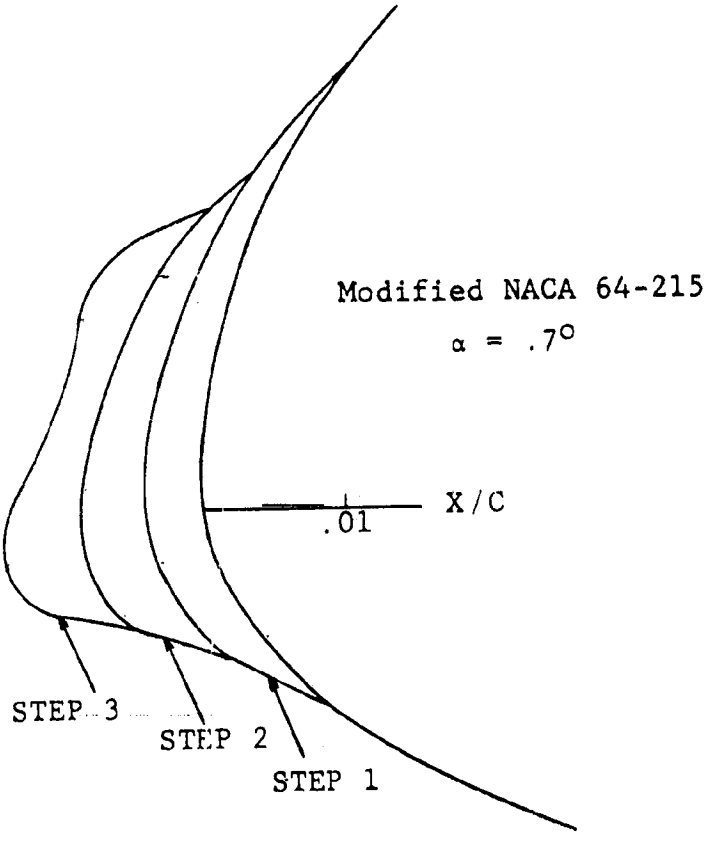

FIGURE 34. PREDICTED RIME ICE SHAPES FOR THREE FIVE MINUTE TIME STEPS

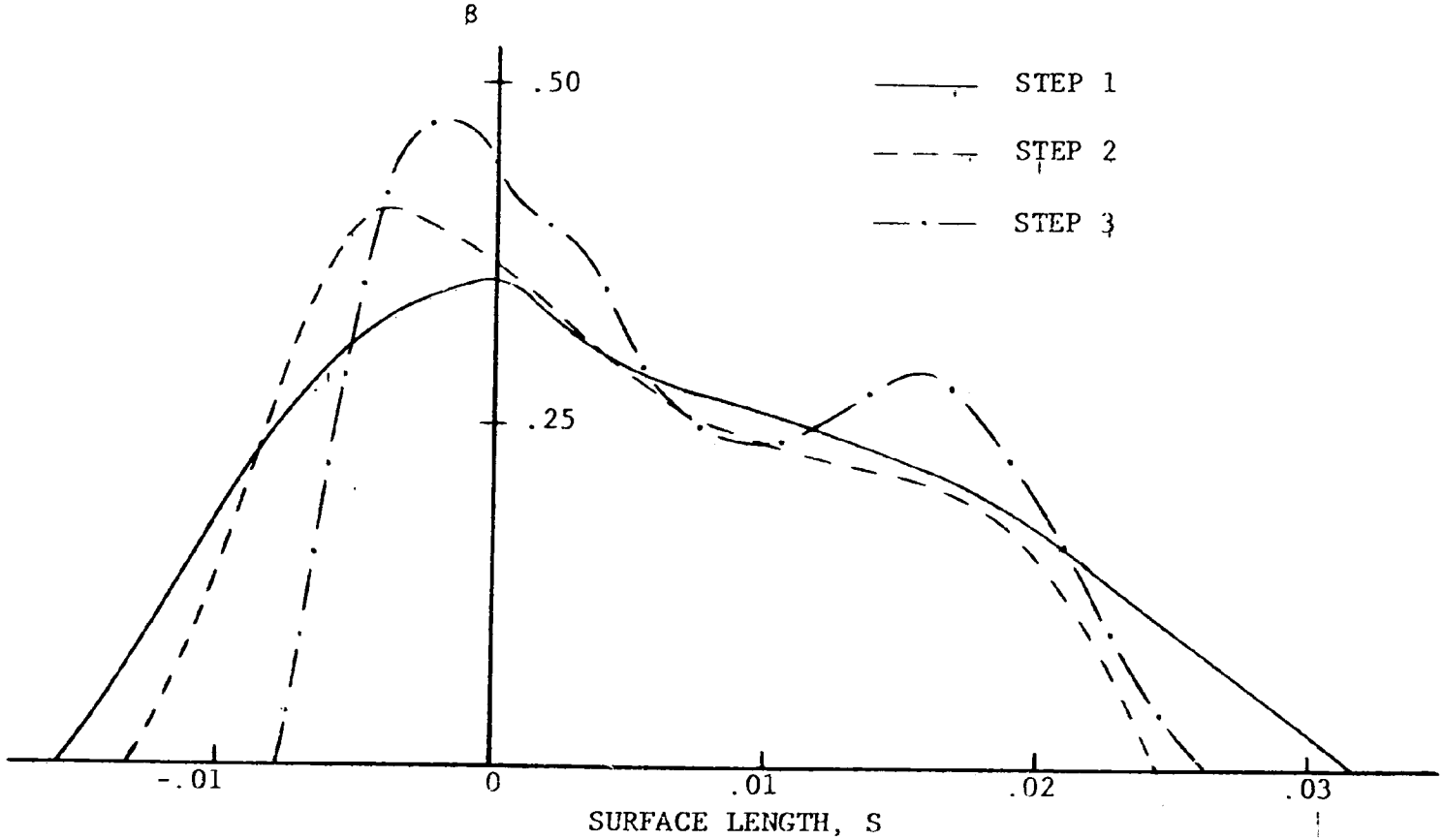

FIGURE 35. IMPINGEMENT EFFICIENCY CURVES FOR THE MODIFIED NACA 64-215 AIRFOIL ANALYZED USING THREE FIVE MINUTE TIME STEPS

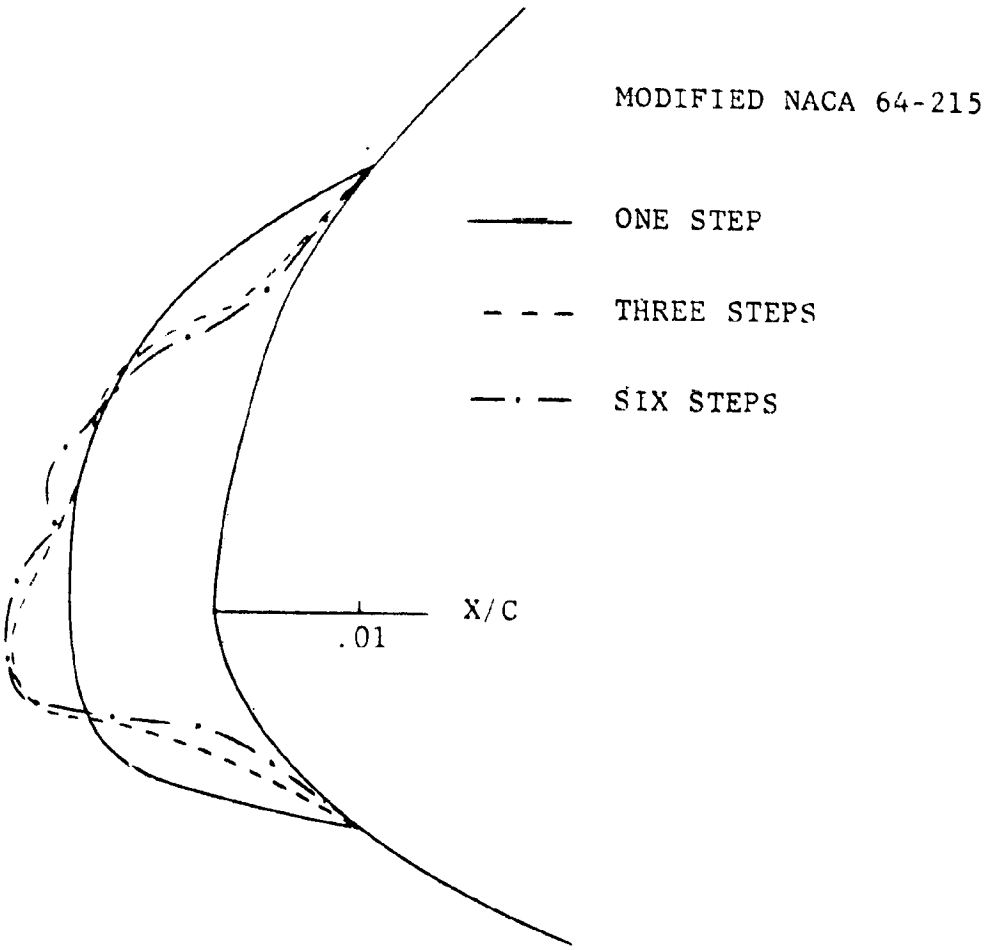

FIGURE 36. EFFECT OF THE NUMBER OF TIME STEPS ON THE ICE SHAPE PREDICTION

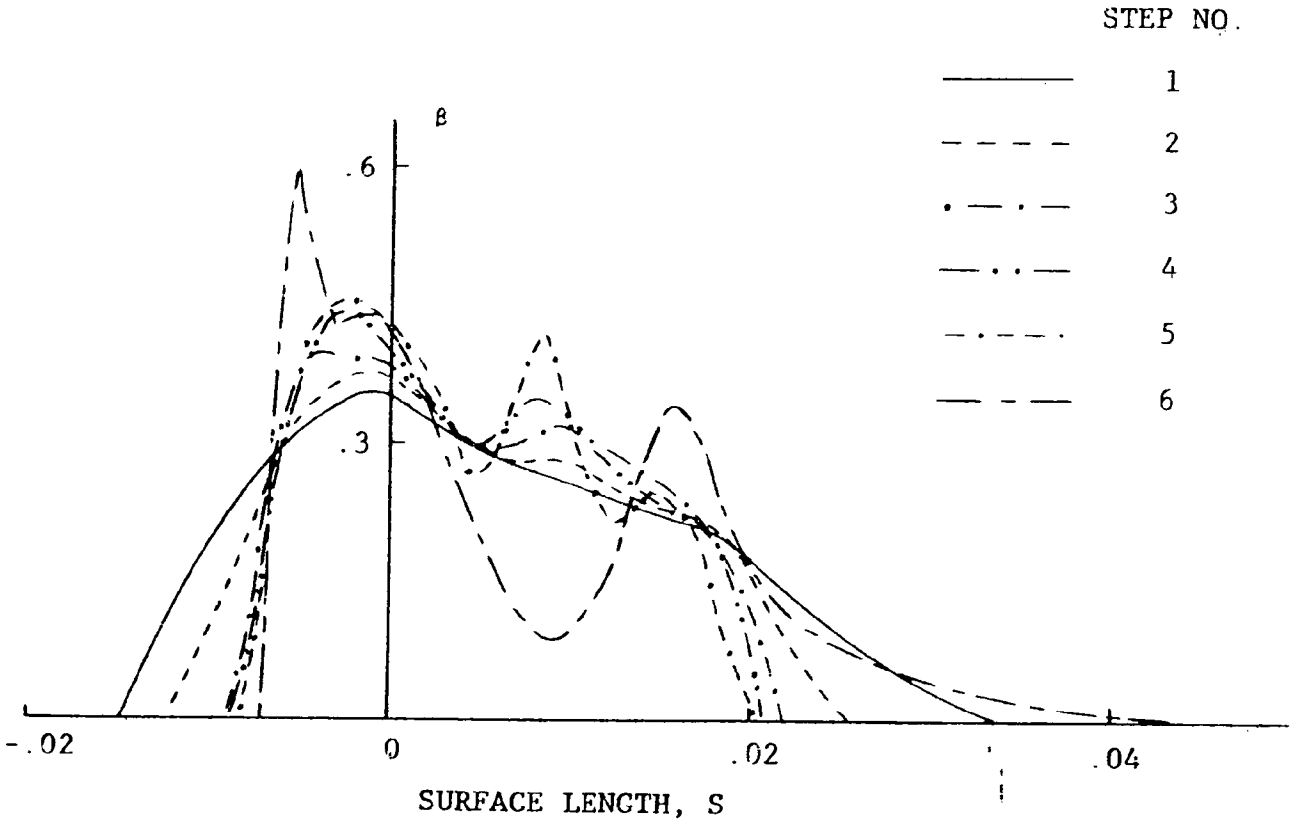

FIGURE 37. IMPINGEMENT EFFICIENCY CURVES FOR THE MODIFIED NACA 64-215 AIRFOIL ANALYZED USING SIX 2.5 MINUTE TIME STEPS

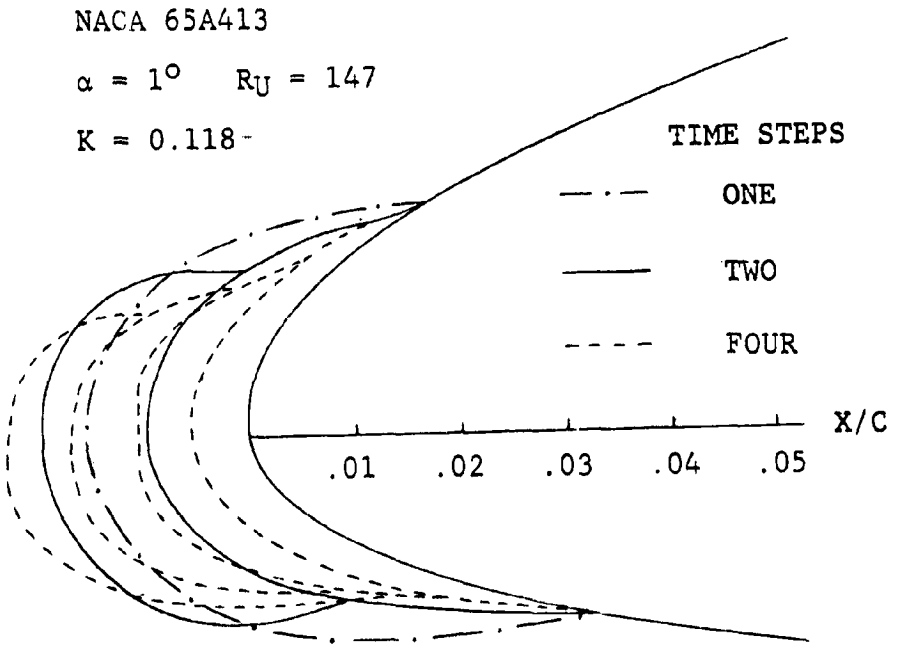

FIGURE 38. EFFECT OF THE NUMBER OF TIME STEPS ON THE PREDICTED RIME ICE SHAPE FOR A NACA 65A413 AIRFOIL

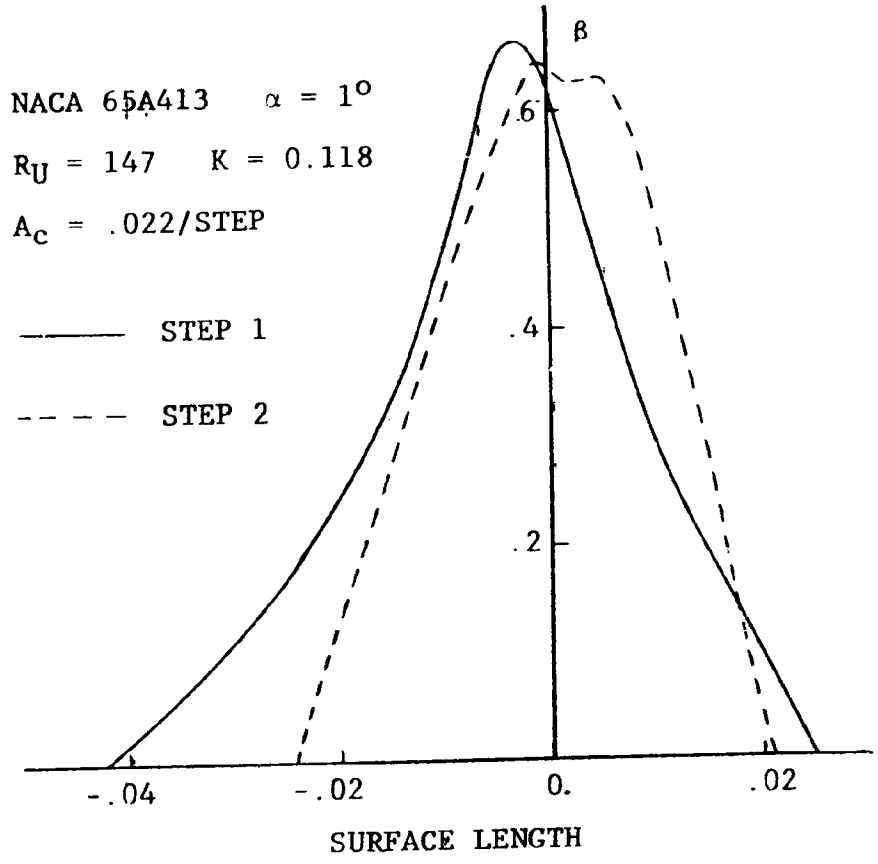

FIGURE 39. IMPINGEMENT EFFICIENCY CURVES FOR THE TWO TIME STEP ICE CALCULATION

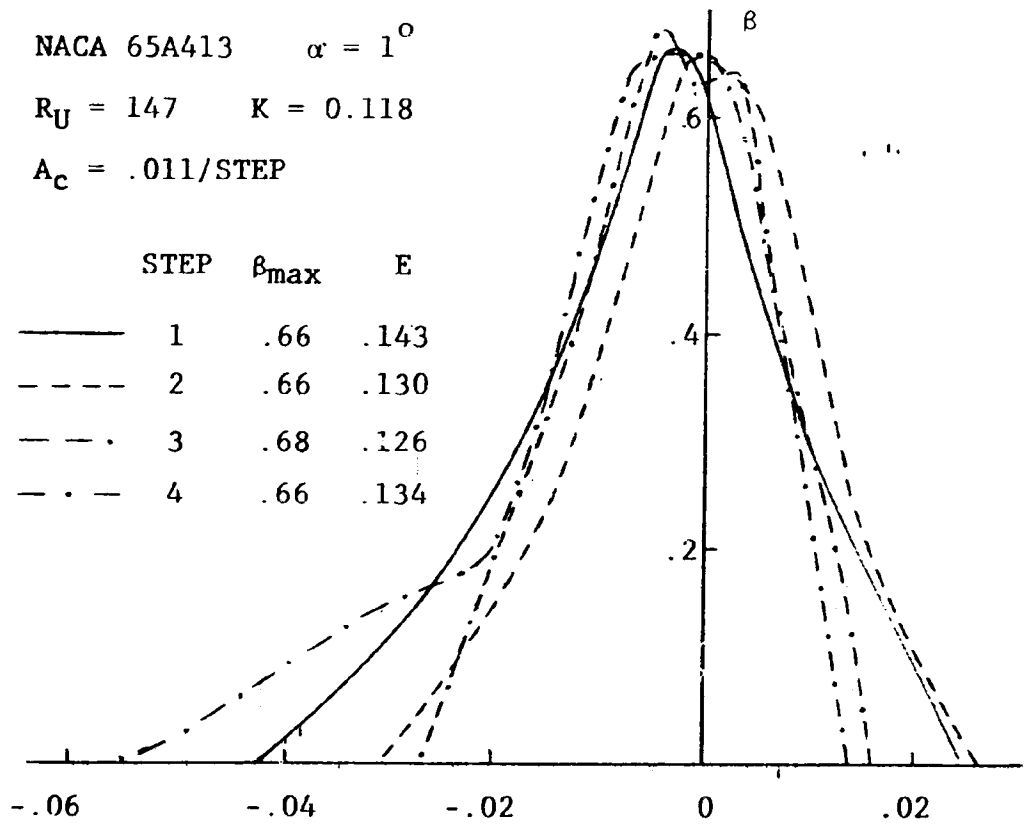

FIGURE 40. IMPINGEMENT EFFICIENCY CURVES FOR THE FOUR TIME STEP ICE SHAPE CALCULATION

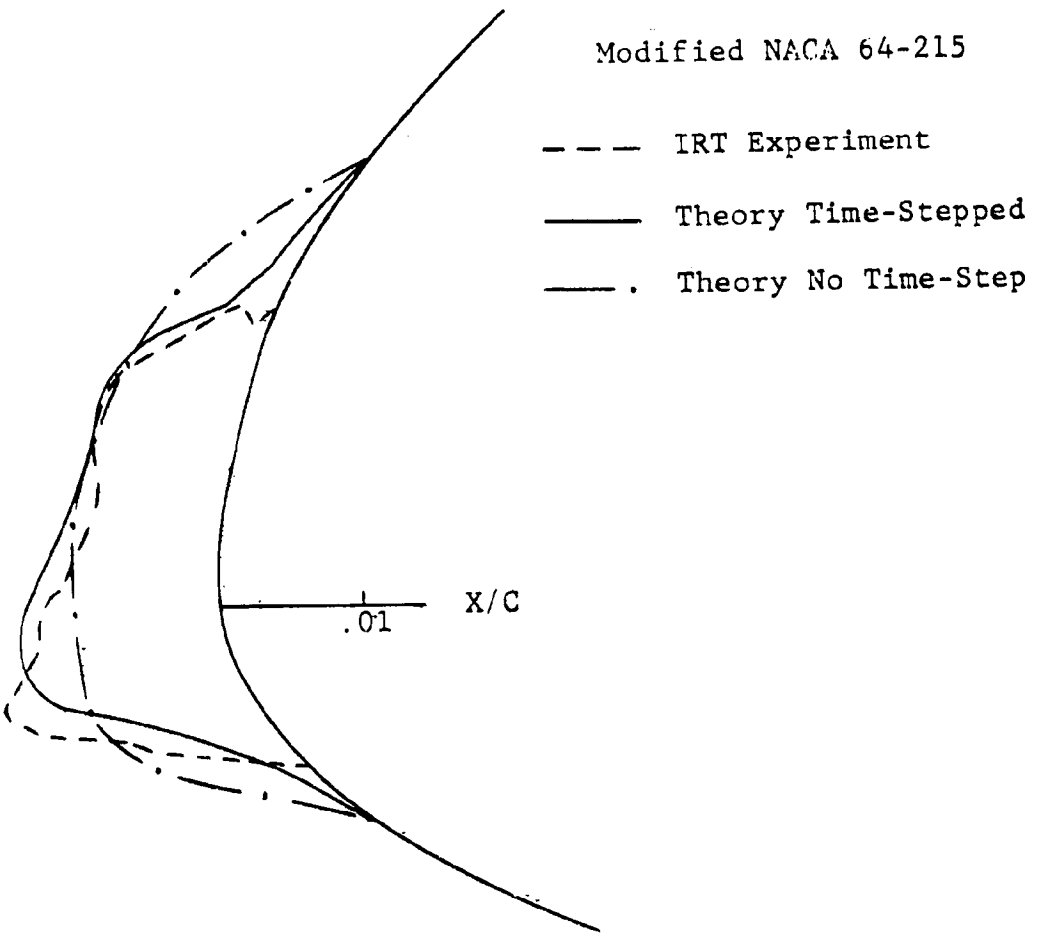

FIGURE 41. THEORETICAL RIME ICE SHAPE COMPARED TO EXPERIMENT FOR THE MODIFIED NACA 64-215 AIRFOIL

NACA 65A004

——— NACA EXPERIMENT, E = .208

– – – 5 1 MIN TIME STEPS, E = .163

— · — 1 5 MIN STEP, E = .153

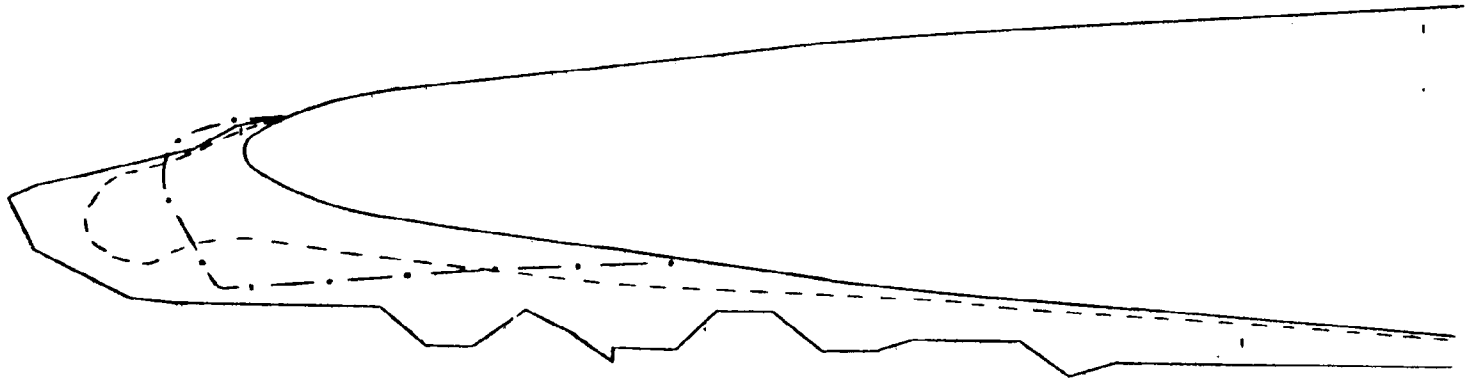

FIGURE 42. THEORETICAL RIME ICE SHAPE COMPARED TO EXPERIMENT FOR THE NACA 65A004 AIRFOIL

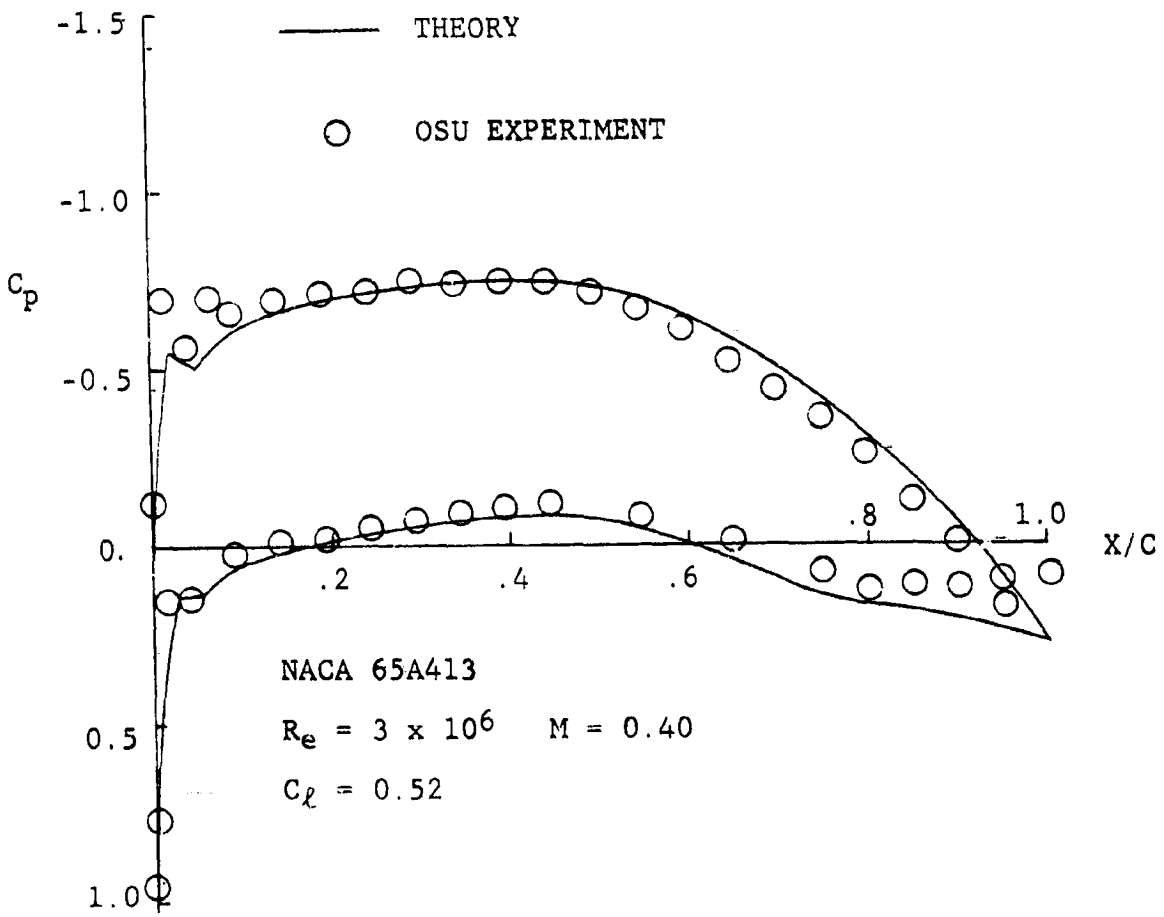

FIGURE 43. THEORETICAL AND EXPERIMENTAL PRESSURE DISTRIBUTION FOR THE CLEAN NACA 65A413 AIRFOIL

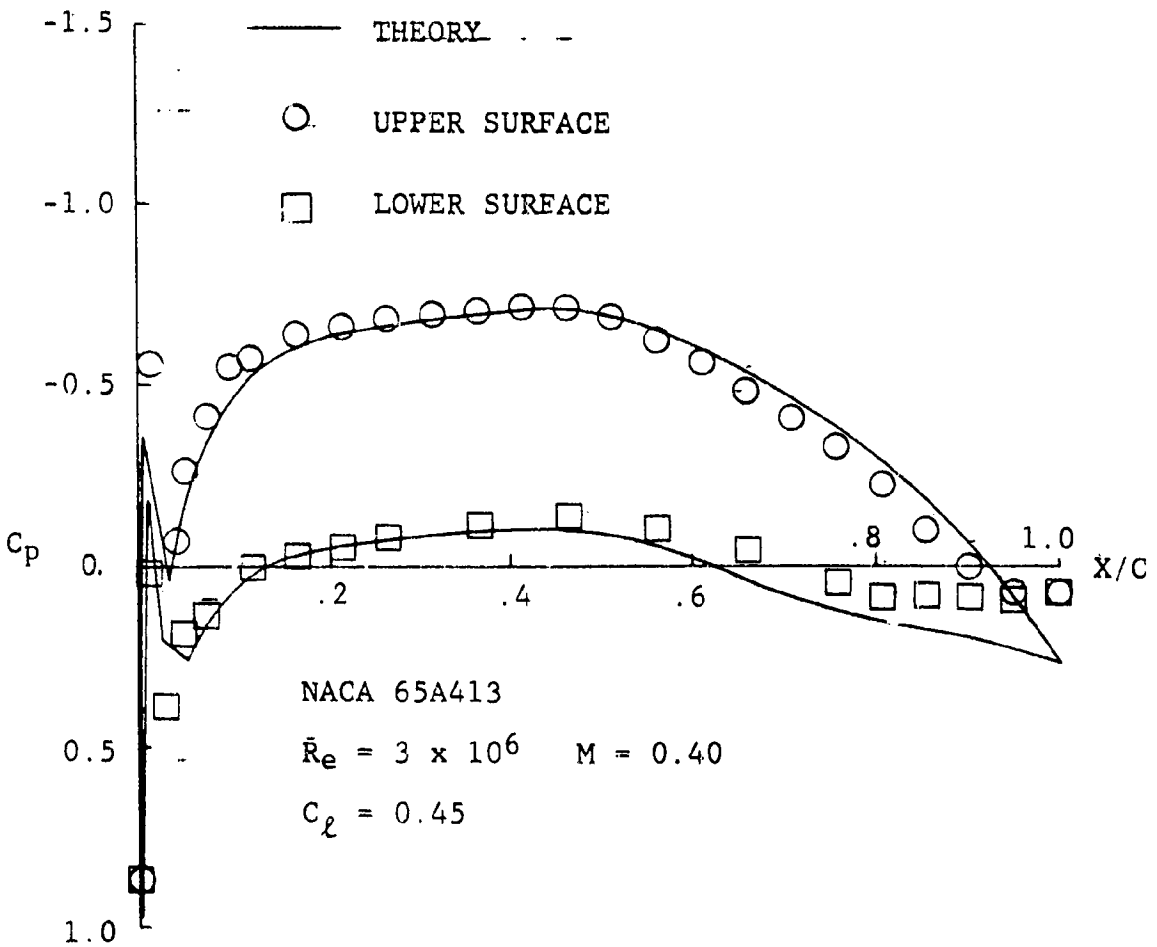

FIGURE 44. THEORETICAL AND EXPERIMENTAL PRESSURE DISTRIBUTION FOR THE NACA 65A413 AIRFOIL WITH SIMULATED RIME ICE

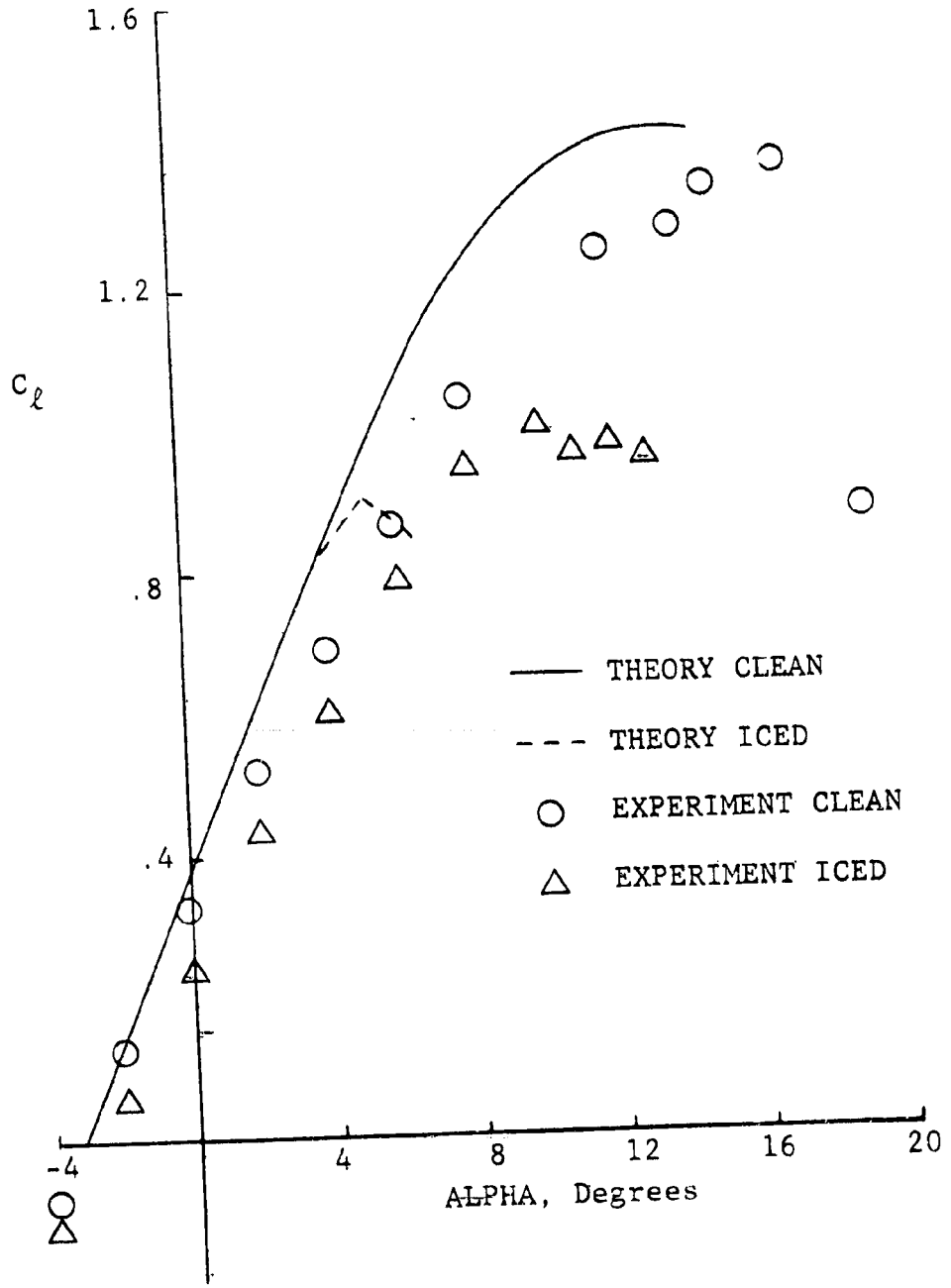

FIGURE 45. THE PREDICTED LIFT COEFFICIENT COMPARED TO EXPERIMENT FOR A NACA 65A413 AIRFOIL CLEAN AND WITH SIMULATED ICE

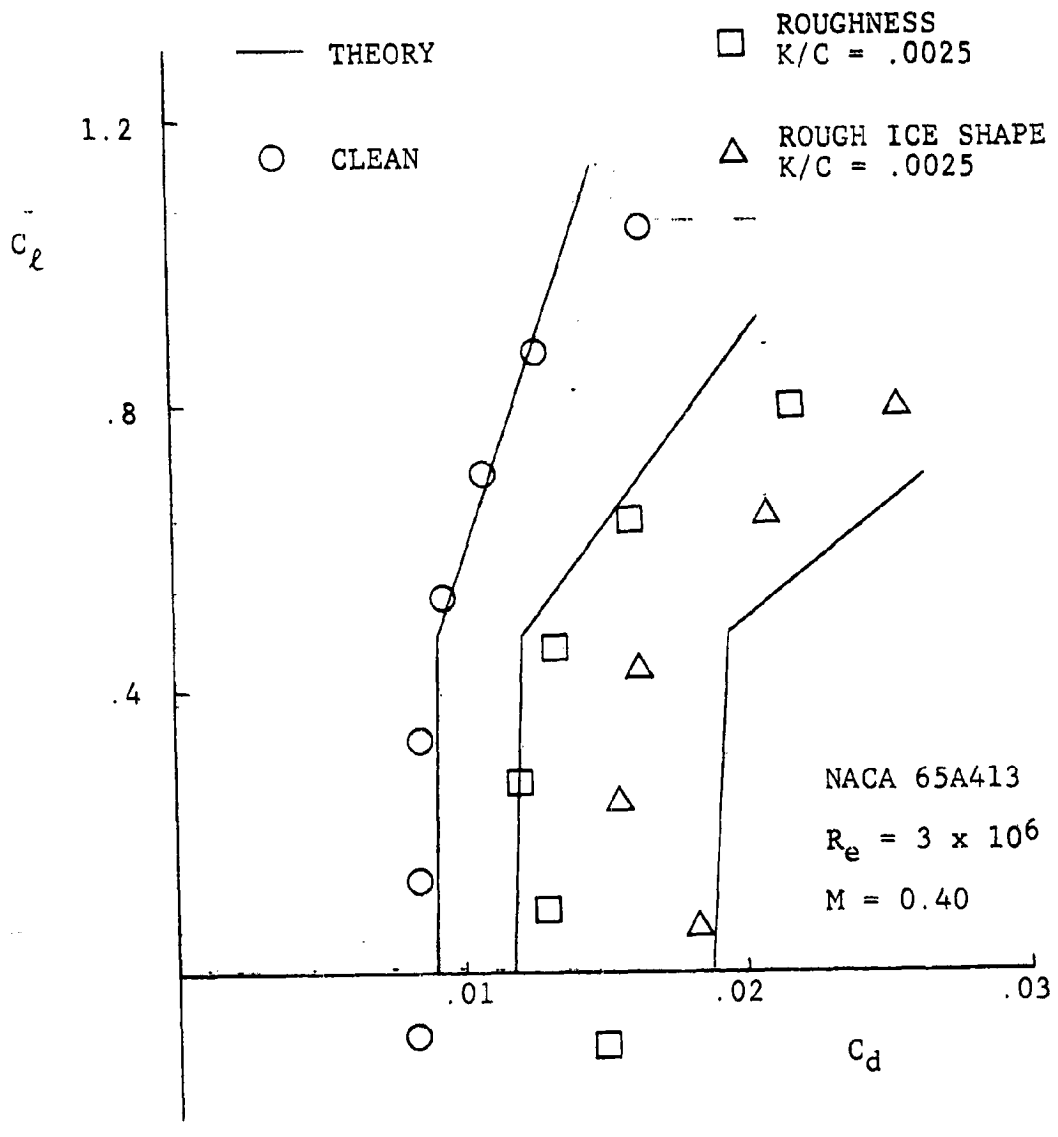

FIGURE 46. DRAG POLARS FOR THE NACA 65A413 AIRFOIL WITH LEADING EDGE MODIFICATIONS COMPARED TO THEORY

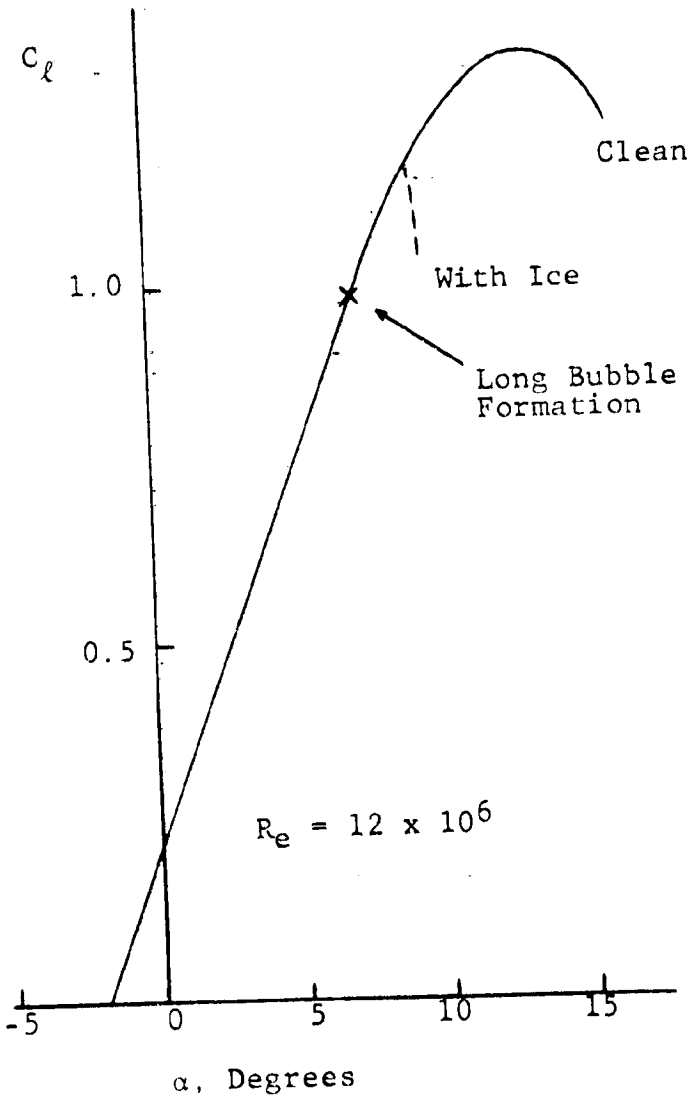

FIGURE 47. PREDICTED LIFT COEFFICIENT AS A FUNCTION OF ANGLE OF ATTACK FOR THE MODIFIED NACA 64-215 AIRFOIL

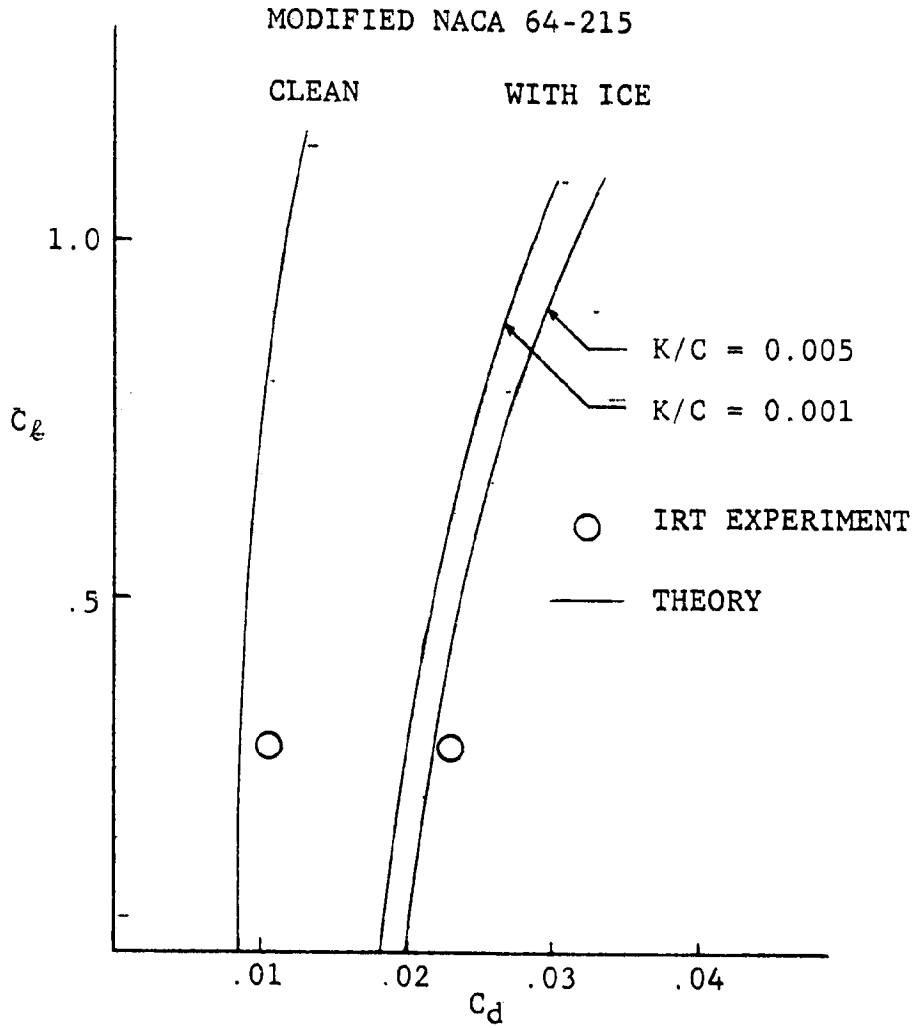

FIGURE 48. EXPERIMENTAL AND THEORETICAL DRAG POLARS FOR THE MODIFIED NACA 64-215 AIRFOIL CLEAN AND WITH ICE

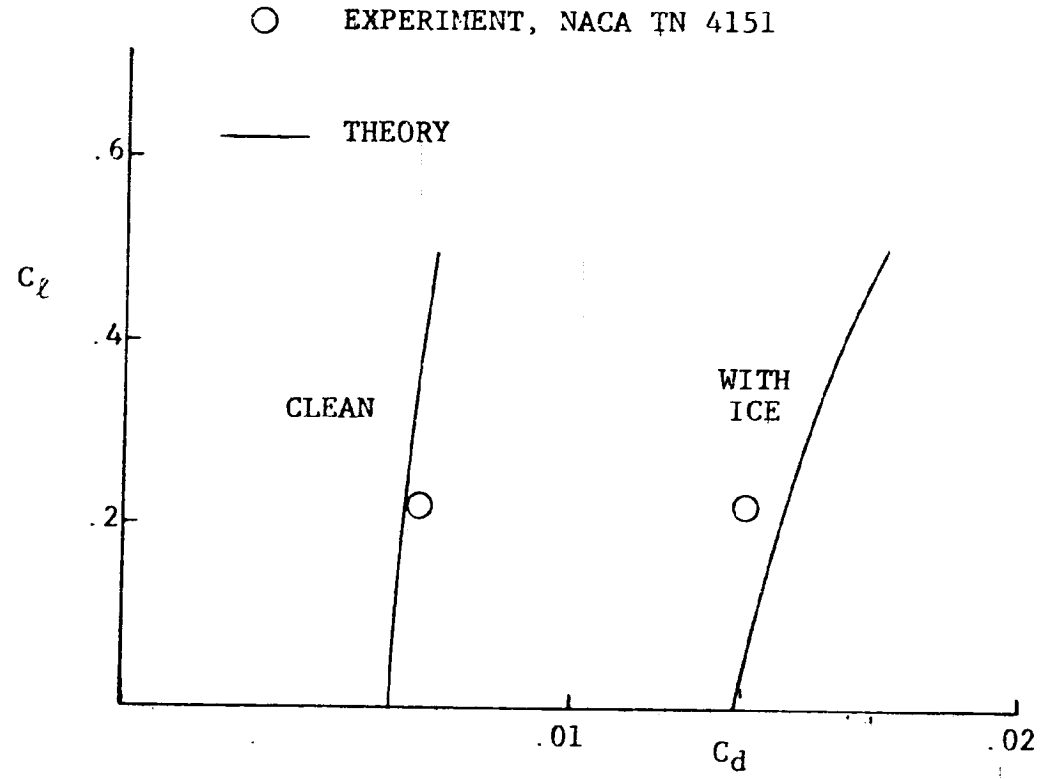

FIGURE 49. EXPERIMENTAL AND THEORETICAL DRAG POLARS FOR A NACA 65A004 AIRFOIL CLEAN AND WITH ICE

APPENDIX

An experimental program has been conducted at The Ohio State University's Aeronautical and Astronautical Research Laboratory to determine the aerodynamic characteristics of an airfoil with simulated rime ice. A wind tunnel test was performed using an existing airfoil section to gather data to be used in the validation of the iced airfoil analysis method. The experiment was performed not only to generate simulated rime ice aerodynamic data, but also to test the hypothesis used in the analytical method that the effects of ice shape and roughness can be handled separately.

The tests were conducted using four different model configurations:

1.) Clean airfoil (baseline)
2.) Airfoil with leading edge roughness
3.) Airfoil with smooth rime ice shape
4.) Airfoil with rime ice shape and leading edge roughness added (simulated rime ice)

By evaluating the aerodynamic characteristics of each configuration, the effects of surface roughness and ice shape can be determined. By comparing model two to the baseline a check on the ΔC_d prediction of figure 15 can be made as well as a check on the $\Delta C_{\ell_{max}}$ data of Brumby,

figure 13. The results of models 3 and 4 compared to the baseline will provide verification of the $C_{\ell_{max}}$ analysis. Finally the tests of model 4 will verify the entire theoretical method.

Experimental Facility

The experimental facility used in this study was the OSU 6 by 22 Transonic Airfoil Wind Tunnel [69]. The tunnel is designed for two dimensional testing with a test section six inches wide, twenty-two inches high, and forty-four inches long. The side walls are solid, while the top and bottom walls of the tunnel are perforated with a porosity of ten percent. The tunnel operates in a blowdown mode with the Mach number controlled by a choke downstream of the test section. Mach numbers from 0.2 to 1.1 are available. The total pressure in the stagnation chamber is varied to control the Reynolds number and provide a range of 1.5 to 33 million per foot.

Lift and moment coefficient data are normally taken using model static pressure taps. Pressure measurements are made with a Scanivalve, trapped volume system which is sampled with a transducer after the tunnel is shut down. Drag data are taken using a wake survey probe which traverses the wake recording the stagnation pressure deficit. The data collected is digitized and stored on magnetic tape in the Harris SLASH 6 Digital Computational

Facility [70] of the Aeronautical and Astronautical Research Laboratory. The data is then reduced to coefficient form [71] and output as quick look data on a CRT display or hard copy printed and plotted.

The interference effects in the OSU 6 by 22 Wind Tunnel have been investigated [69]. Confinement interference, spanwise interference from the side walls, and flow quality have been evaluated. The correction required for six inch chord models has been shown to be negligible. The correction to the angle of attack is on the order of 0.17 degrees per unit C_ℓ. Since this test will use a six inch chord airfoil, no corrections need be made to the data.

Airfoil Model

A NACA 65A413 airfoil section was selected for the experiment. The model used in the wind tunnel was a brass model of six inch chord and six inch span, figure A-1. The original airfoil model was instrumented with 46 static pressure taps of which 42 were used in the data reduction. The trailing edge tap is located on the sidewall due to the physical constraints.

The rime shape which was simulated was that predicted by the time-stepping analysis of figure 37. A comparison of the predicted shape and the shape used on the tunnel model is given in figure A-2. Note that since the

objective of the test was to generate baseline data to validate the analysis, the accurate reproduction of the predicted shape is not required. All that is required is that the ice shape simulated be a representative geometry and that it be adequately documented for the analytical comparison.

A schematic of the airfoil model with the simulated rime ice shape is shown in figures A-3 and A-4. The rime ice shape was simulated by adding a 0.145 inch outside diameter tube to the airfoil leading edge. The mounting blocks were drilled to allow the tube to extend out of the tunnel on both sides. The center section of the tube was replaced by a solid rod which was drilled through to pick up the existing leading edge pressure tap. The tube, now plugged in the center, was used to add an additional tap on the leading edge upper annd lower surfaces, figure A-4. The ice shape was completed by building up the area between the tube and the airfoil until the desired shape was reached. Care was taken to ensure that the affected airfoil pressure taps were extended up through this region to the new airfoil surface. A photograph of the airfoil model with the simulated rime ice shape is shown in figure A-5.

Roughness was added to the model for configurations 2 and 4. This roughness was intended to simulate the actual

roughness on a rime ice shape. Rime ice surface roughness is typically in the range of k/c = 0.001 to 0.005. Carborundum grit with an average size of 0.015 inches was used. This scales to a k/c of 0.0025 for a six inch chord model.

The grit was applied by first coating the surface with Krylon clear acrylic spray to provide the adhesive. The roughness elements were then applied to the surface and two or three coats of acrylic were applied to ensure that the particles were firmly adhered to the surface. The roughness was applied to the leading edge of the airfoil upper and lower surface back to three percent airfoil chord for both configurations 2 and 4. The roughness elements were distributed randomly at a concentration of about 250 per square inch of surface area, figure A-6.

Results and Discussion

The airfoil section selected is typical of that currently in use on general aviation and business aircraft. To simulate actual operating conditions, a Mach number of 0.40 and a Reynolds number based on chord length of 3 million were chosen for the cruise case. These conditions were used in testing the airfoil at angles of attack of eight degrees and less. To determine the maximum lift coefficient, conditions more typical of a landing approach were used. For angles of attack greater

than eight degrees a Mach number of 0.23 and Reynolds number of 2 million were used.

Pressure distributions for the clean airfoil and with surface roughness added, configurations 1 and 2, are shown in figure A-7. Here both airfoils are at two degrees angle of attack. Both curves are similar, however the areas, which give the model lift coefficient, are different. The model with roughness experiences a decrease in lift over the clean model. This is probably due to the effect of the roughness on the boundary layer. The roughness results in a thicker boundary layer at the trailing edge upper surface and therefore a larger displacement thickness. This effectively removes camber from the airfoil and decreases the lift, shifting to a more positive value.

Note also the reduced pressure recovery at the trailing edge for the rough airfoil. This suggests increased drag which can be easily seen in the wake deficit plots of figure A-8. Here the roughened airfoil has a larger velocity deficit, and therefore more drag. This result is in good agreement with earlier experimental work showing increased drag with surface roughness.

The airfoil with simulated rime ice experiences somewhat different surface pressures near the leading edge, figure A-9. Note that here the chord length is

based on the iced airfoil chord, 1.024 times the original chord. The aft portion of the Cp distribution is similar to the no ice case, however the leading edge region is altered by the ice shape. Pressure spikes, severe discontinuities in the pressure distribution, occur on the upper and lower surfaces where the ice shape joins the airfoil contour. For this ice shape this represents a discontinuity in the second derivative of the surface shape. These spikes were detected by the two additional pressure taps installed in the tube which forms the leading edge shape of the simulated ice. This demonstrates the importance of the installation of pressure taps in simulated ice shapes. The effects of the pressure spikes will be seen to be more serious at higher angles of attack.

Figure A-10 shows the lift coefficient as a function of angle of attack for all four airfoil configurations. Configurations 2 through 4 all have approximately the same effect on the lift coefficient. These changes are a shift in α_{LO} and a sizeable decrease in $C_{\ell_{max}}$. The good agreement between the $C_{\ell_{max}}$ for the smooth and rough rime ice shape suggests that the stall is caused by the shape. As seen in figure A-9, the severe pressure gradients near the leading edge probably lead to a leading edge separation bubble. This accounts for the early separation

at higher angles of attack.

The reduced $C_{\ell_{max}}$ for the airfoil with only surface roughness is due to a different mechanism. Here the roughness causes a thickening of the boundary layer and decreases pressure recovery at the trailing edge. This ultimately leads to early trailing edge separation which moves forward as α increses to cause the reduction in maximum lift coefficient. The apparent agreement in $C_{\ell_{max}}$ for configurations 2 and 4 is due to the particular k/c and rime ice shape chosen, and should not be interpreted as a general trend.

Figure A-11 shows the measured drag polars for all four configurations. The smooth airfoil is seen to have a minimum drag coeficient of about 0.086. This is well above the laminar "drag bucket" values expected for an airfoil of this type. The brass airfoil model used was slightly tarnished and therefore did not have the surface finish necessary to permit long laminar runs.

An increment in drag was seen due to the addition of surface roughness. This drag increase was certainly expected and is of a reasonable magnitude. The reason for the apparent agreement between the rough airfoil and the smooth ice shape, configurations 2 and 3, is not obvious. Most likely this is not a general result, but again merely a coincidence resulting from the roughness and the rime

ice geometry chosen.

An additional drag increment was measured when roughness elements were added to the rime ice shape, configuration 4. This is the simulated rime ice shape. This increase in drag contrasts the maximum lift coefficient case were configurations 3 and 4 behaved similarly. Therefore, while ice shape alone is sufficient to determine $C_{\ell_{max}}$, the surface roughness of the ice must be modeled to simulate accurately the total drag increase due to airfoil rime icing.

The moment coefficient about the quarter point of the original airfoil is plotted as a function of lift coefficient in figure A-12. Configurations 2 through 4 all show a reduction in the nose down pitching moment when compared to the clean model. The leading edge roughness as described before thickens the boundary layer and unloads the aft portion of the airfoil section. Therefore the nose down pitching moment is reduced. The smooth ice shape adds area in front of the nose providing more nose up moment, explaining configuration three's reduction in nose down pitching moment. The rough ice shape combines the two above effects, resulting in a slightly larger reduction in nose down pitching moment than that experienced by the shape alone.

This test not only provided data to verify the analysis, but has demonstrated the feasability of performing simulated iced airfoil tests in a small scale wind tunnel facility. The data show the expected results of decreased maximum lift coefficient and increased drag with the simulated ice shape. In addition a reduction in nose down pitching moment was measured with simulated rime ice. The pressure distributions measured for the airfoil with simulated rime ice are believed to be the first such data published. These Cp plots provide insight into the physical phenomena and detailed information to be used to evaluate and refine current analytical methods.

FIGURE A-1. CLEAN WIND TUNNEL MODEL OF AN NACA 65A413 AIRFOIL

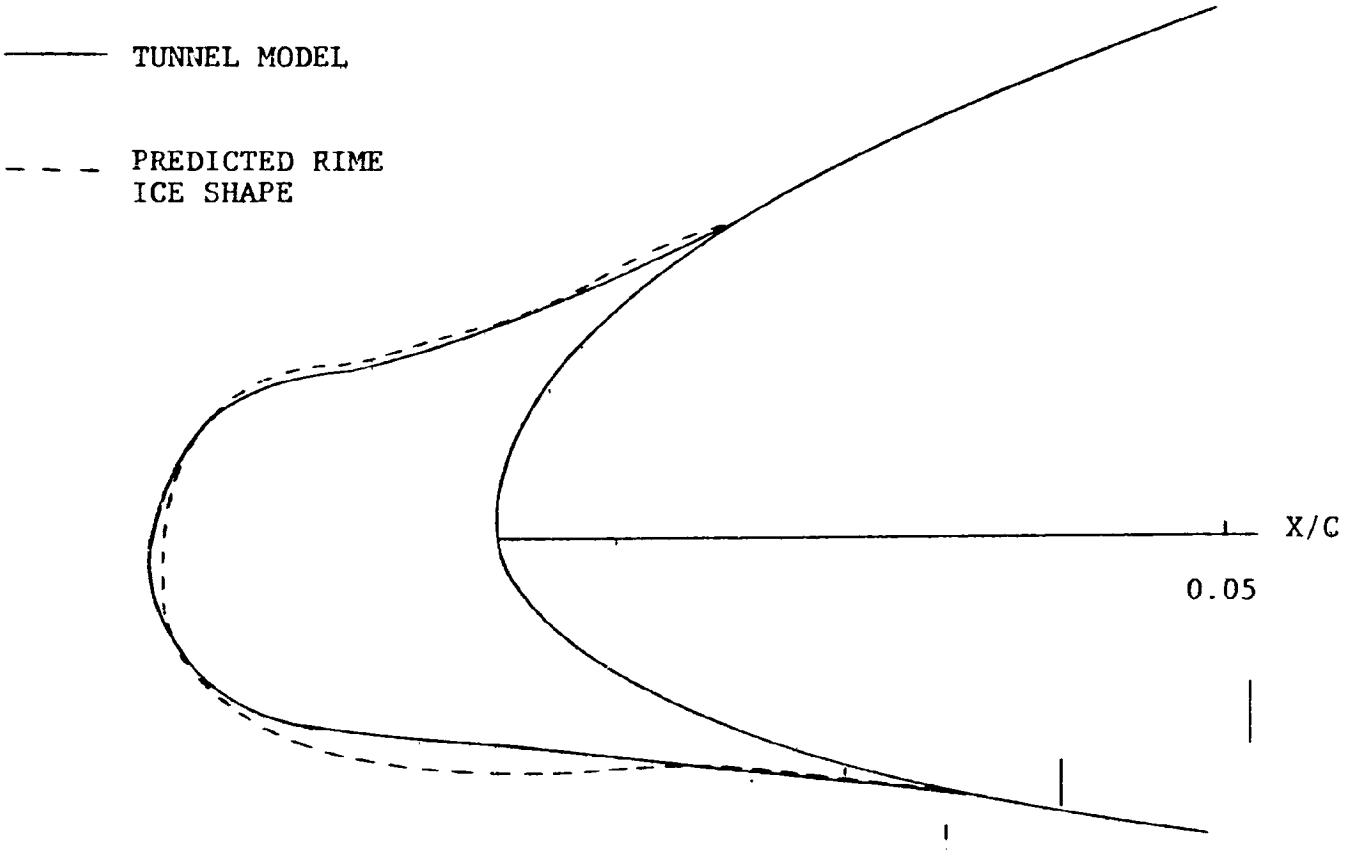

FIGURE A-2. PREDICTED RIME ICE SHAPE AND THE ACTUAL TUNNEL MODEL FOR THE NACA 65A413 TEST

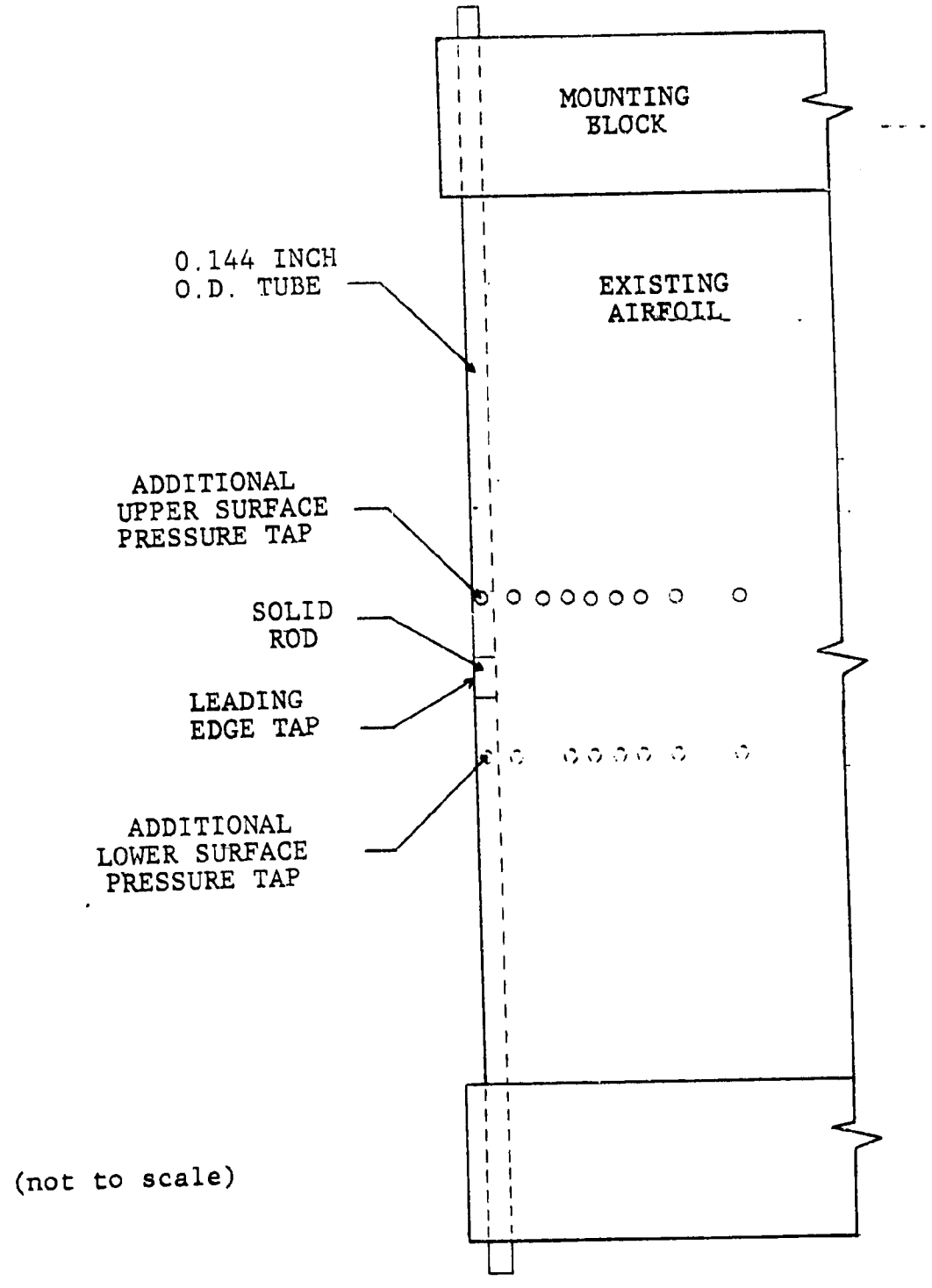

FIGURE A-3. TOP VIEW OF SIMULATED RIME ICE AIRFOIL MODEL

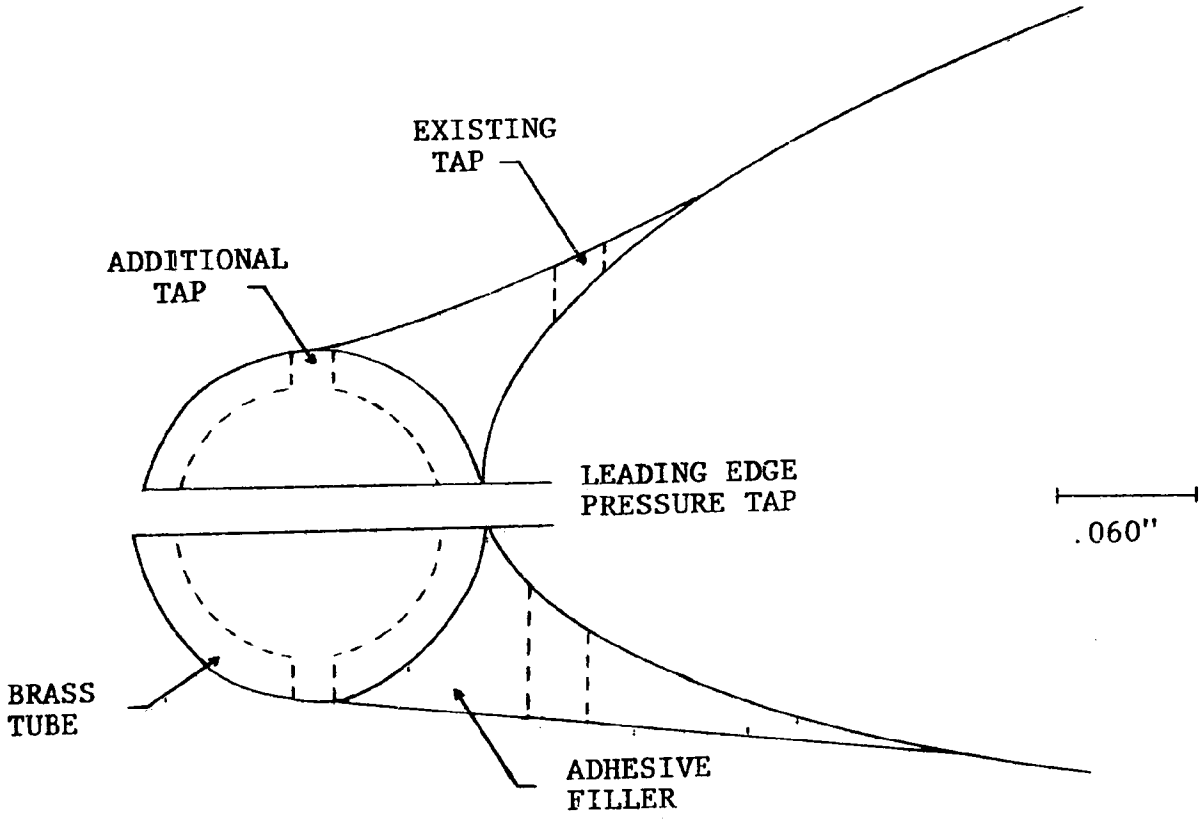

FIGURE A-4. CROSS SECTION OF SIMULATED RIME ICE AIRFOIL MODEL SHOWING PRESSURE TAP LOCATIONS

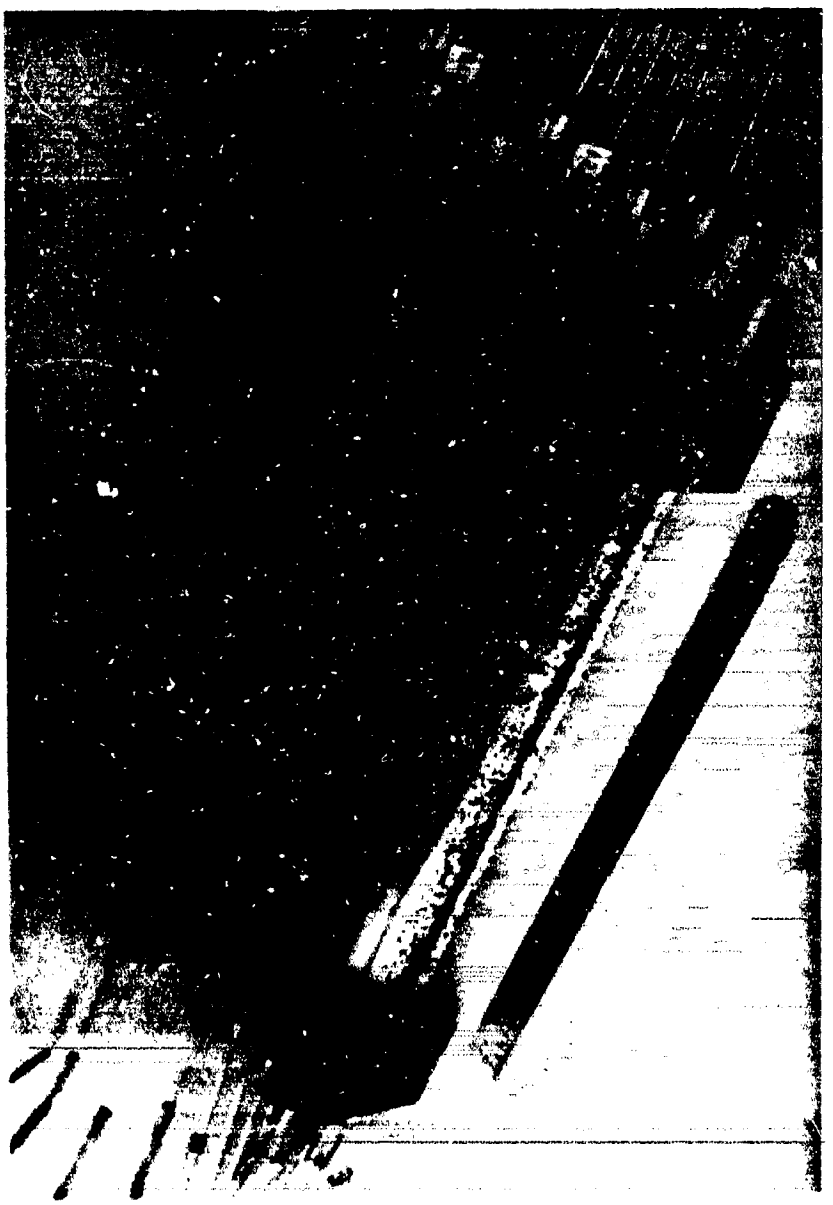

FIGURE A-5. WIND TUNNEL MODEL OF AN NACA 65A413 AIRFOIL WITH SIMULATED RIME ICE

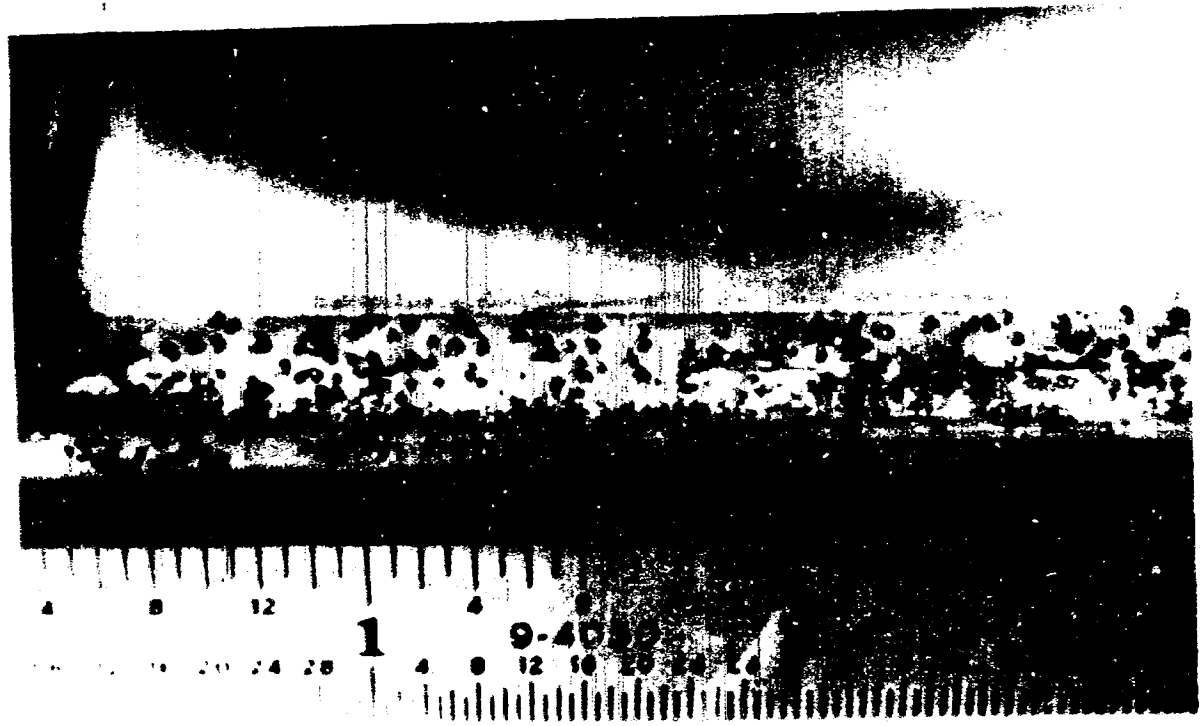

FIGURE A-6. LEADING EDGE OF SIMULATED RIME ICE MODEL SHOWING SURFACE ROUGHNESS

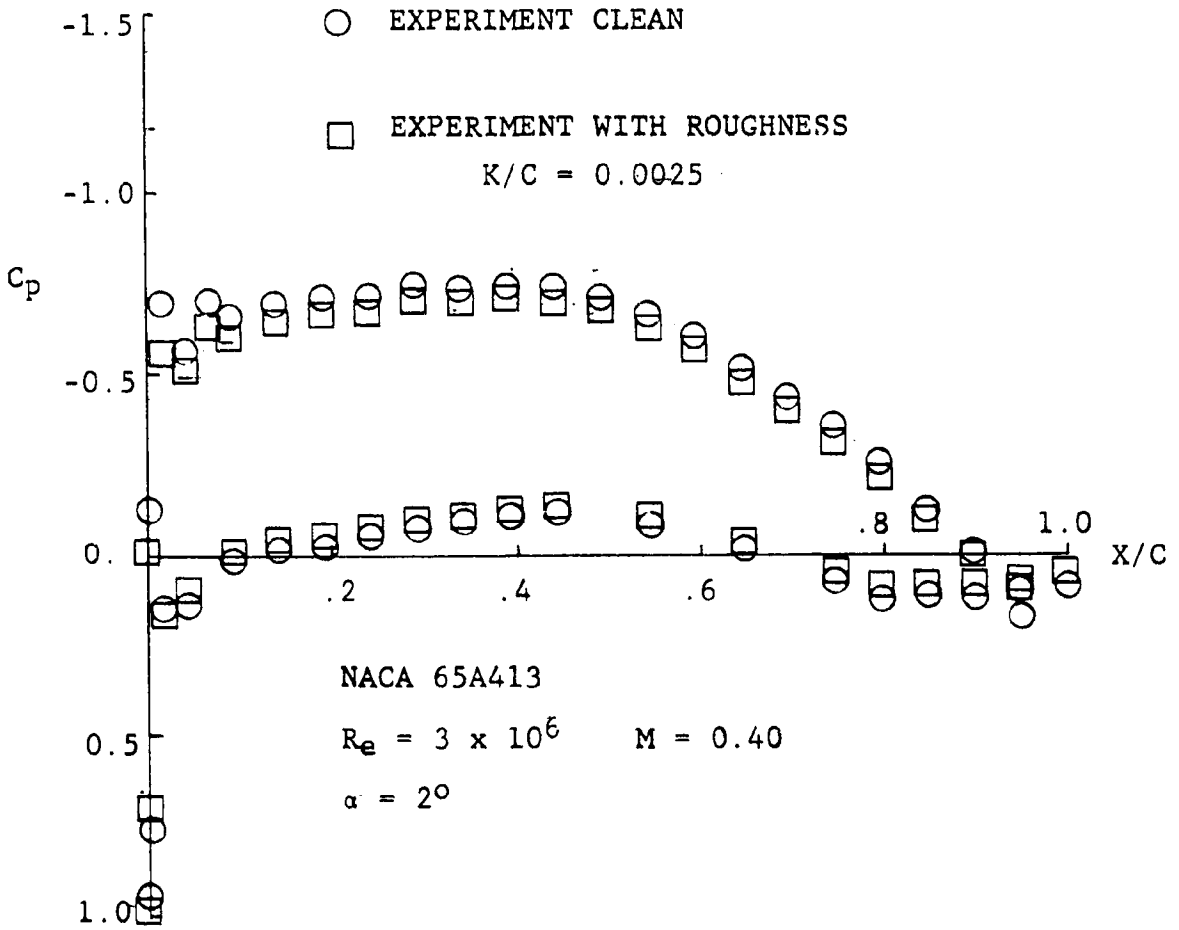

FIGURE A-7. EXPERIMENTAL PRESSURE DISTRIBUTIONS FOR A NACA 65A413 WITH A SMOOTH AND ROUGH LEADING EDGE

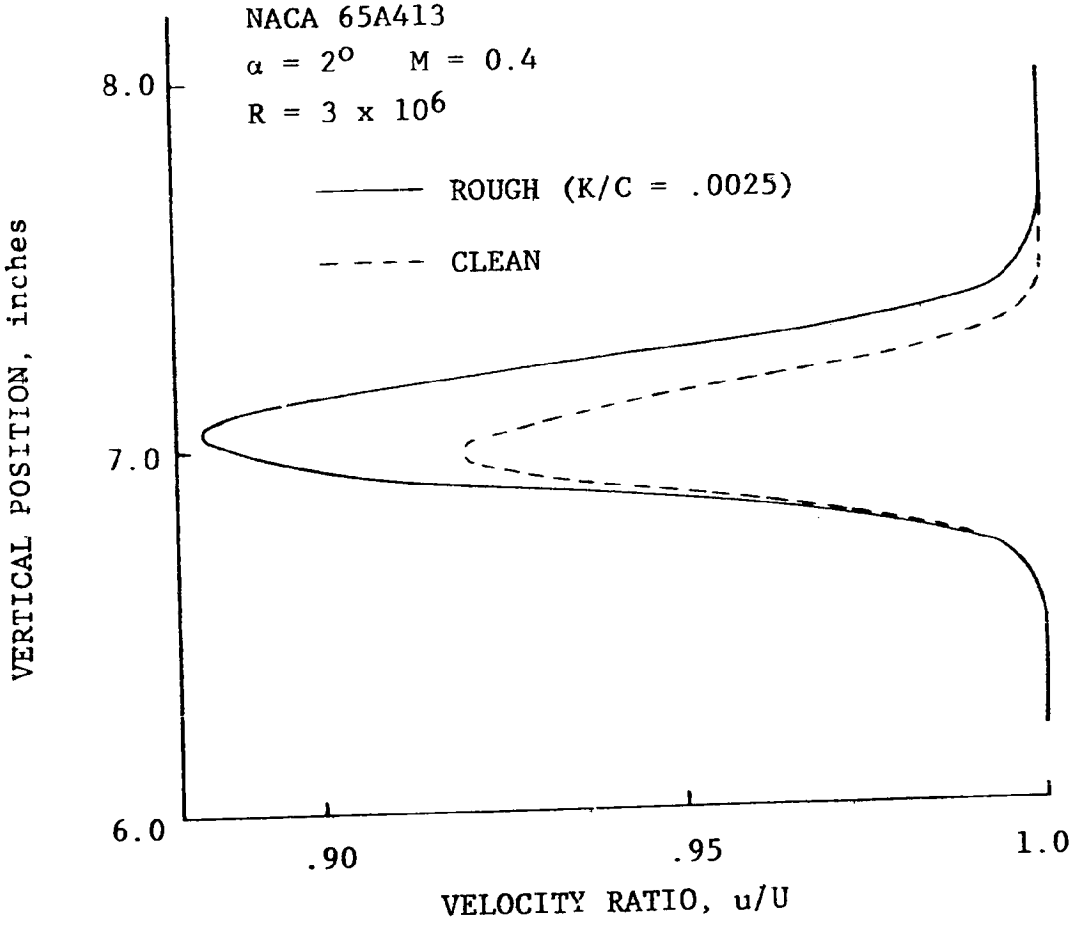

FIGURE A-8. VELOCITY RATIO IN THE WAKE OF THE NACA 65A413 AIRFOIL CLEAN AND WITH LEADING EDGE ROUGHNESS

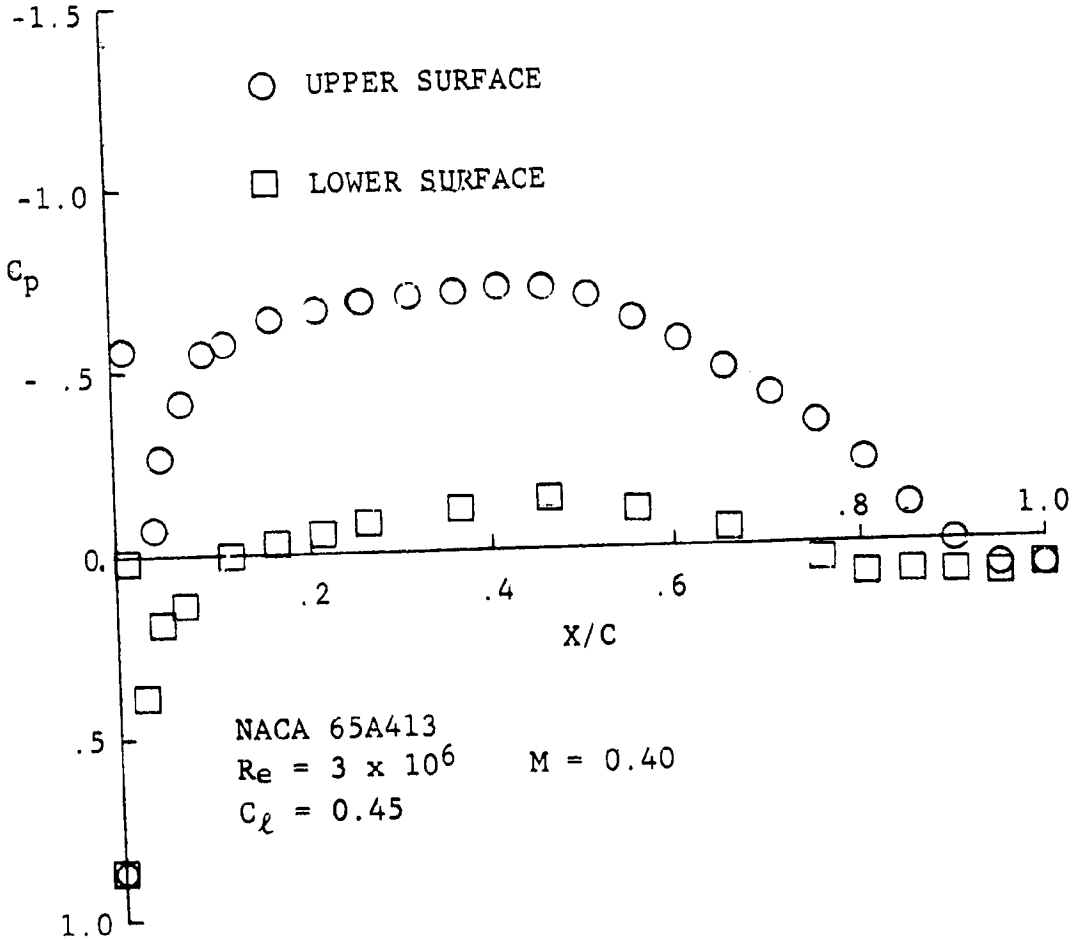

FIGURE A-9. EXPERIMENTAL PRESSURE DISTRIBUTION OF AN NACA 65A413 AIRFOIL WITH SIMULATED RIME ICE

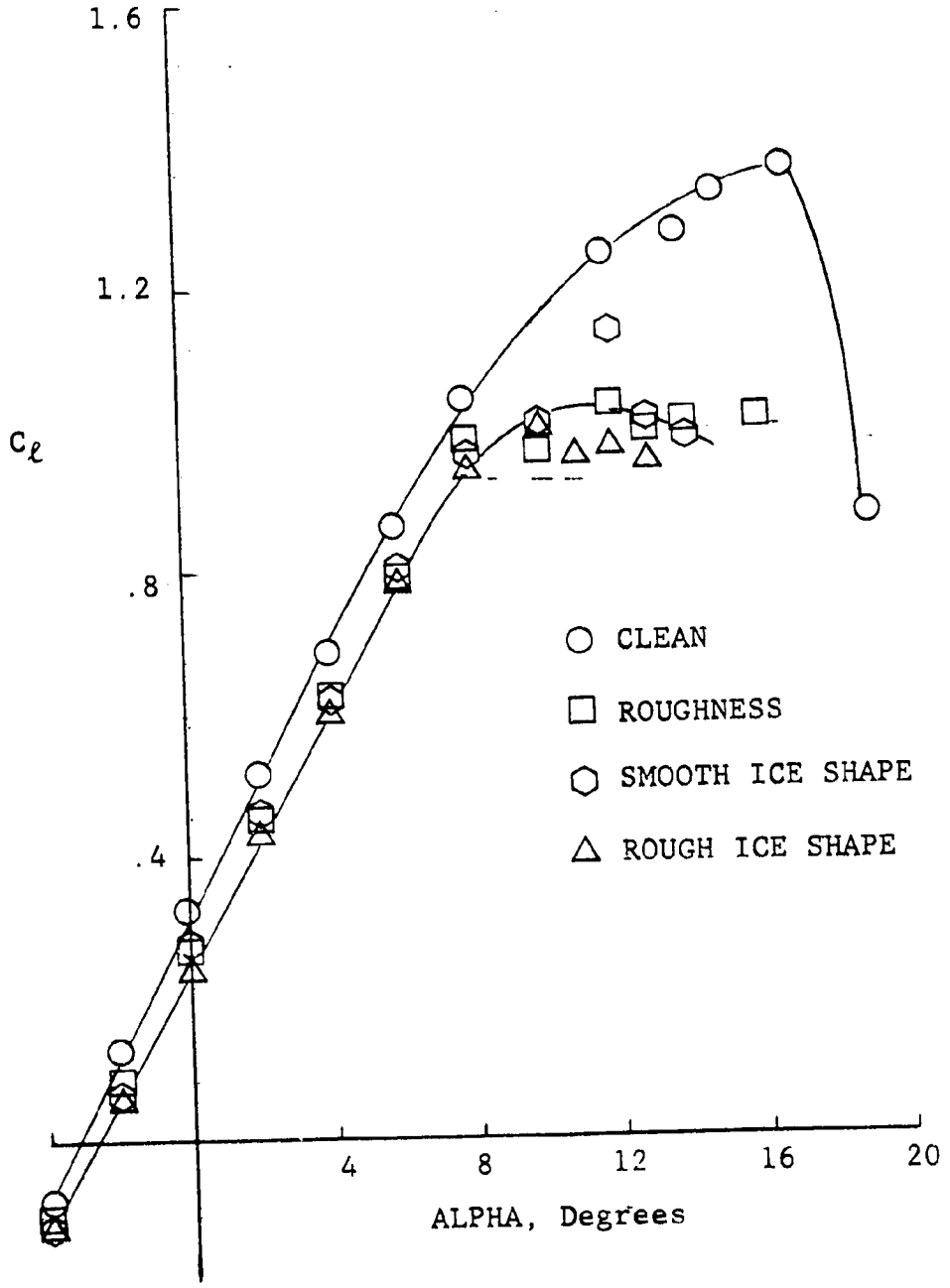

FIGURE A-10. LIFT COEFFICIENT AS A FUNCTION OF ANGLE OF ATTACK FOR THE NACA 65A413 AIRFOIL WITH LEADING EDGE MODIFICATIONS

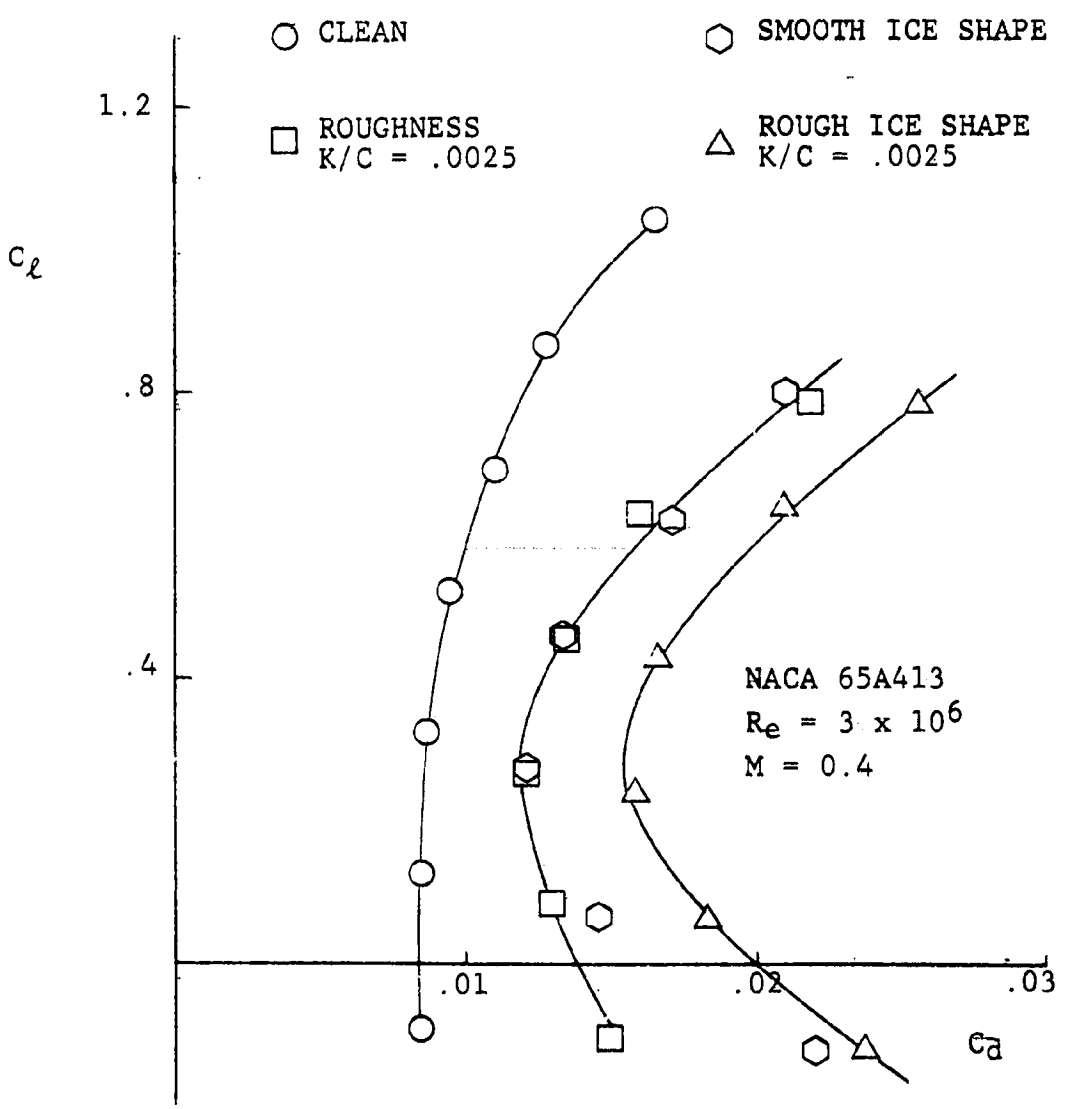

FIGURE A-11. DRAG POLARS FROM THE WIND TUNNEL TESTS OF THE NACA 65A413 AIRFOIL WITH LEADING EDGE MODIFICATIONS

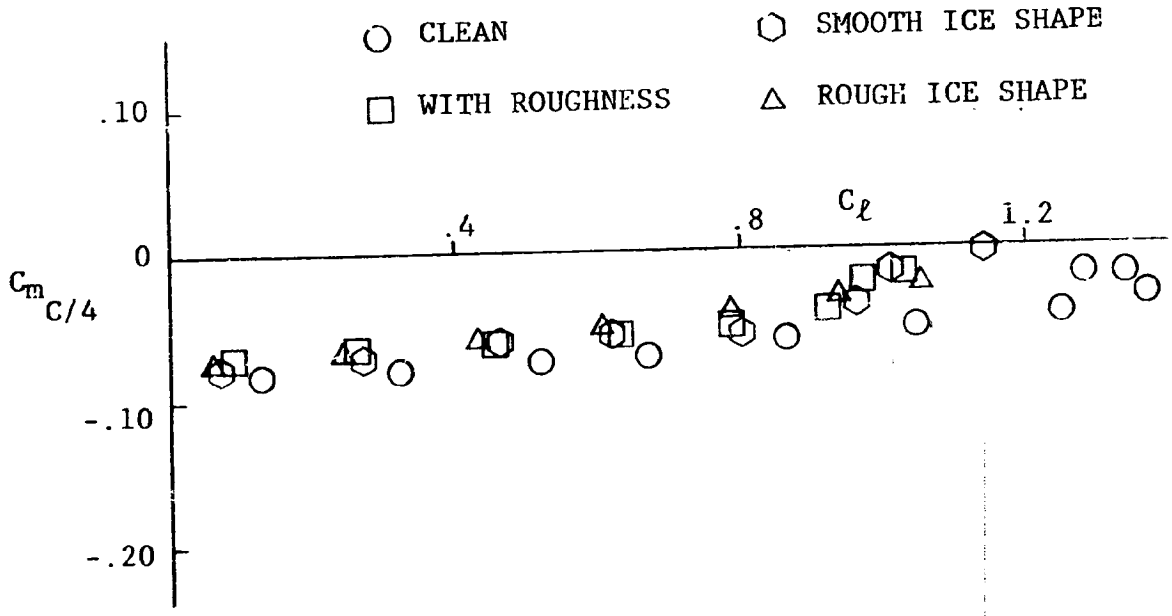

FIGURE A-12. MOMENT COEFFICIENT AS A FUNCTION OF LIFT COEFFICIENT FROM THE WIND TUNNEL TESTS OF THE NACA 65A413 AIRFOIL WITH LEADING EDGE MODIFICATIONS